



HAL
open science

Electrodes en diamant pour la fabrication de microsystèmes électrochimiques pour applications biologiques

Raphael Kiran

► **To cite this version:**

Raphael Kiran. Electrodes en diamant pour la fabrication de microsystèmes électrochimiques pour applications biologiques. Autre. Université de Grenoble, 2012. Français. NNT : 2012GRENI077 . tel-00872085

HAL Id: tel-00872085

<https://theses.hal.science/tel-00872085>

Submitted on 11 Oct 2013

HAL is a multi-disciplinary open access archive for the deposit and dissemination of scientific research documents, whether they are published or not. The documents may come from teaching and research institutions in France or abroad, or from public or private research centers.

L'archive ouverte pluridisciplinaire **HAL**, est destinée au dépôt et à la diffusion de documents scientifiques de niveau recherche, publiés ou non, émanant des établissements d'enseignement et de recherche français ou étrangers, des laboratoires publics ou privés.

THÈSE

Pour obtenir le grade de

DOCTEUR DE L'UNIVERSITÉ DE GRENOBLE

Spécialité: **Matériaux, Mécanique, Génie Civil, Electrochimie**

Arrêté ministériel: 7 août 2006

Présentée par

«Raphael / KIRAN»

Thèse dirigée par **«Pascal / Mailley»** et **«Philippe / Bergonzo»**
codirigée par **«Emmanuel / Scorsone»**

préparée au sein du **Laboratoire Capteurs Diamant au
Commissariat à l'Energie Atomique à Saclay**

Electrodes en diamant pour la fabrication de microsystemes électrochimiques pour applications biologiques

Thèse soutenue publiquement le **«21/09/2012»**,
devant le jury composé de:

Pr. John FOORD

Pr. Université d'Oxford, Royaume-Uni, Rapporteur

Pr. Eric McADAMS

Pr. Universités INSA, Lyon, France, Rapporteur

Pr. Christoph NEBEL

Head of business unit and department, micro- and nano-sensors, IAF
Fraunhofer, Freiburg, Allemagne, Membre

Pr. Etienne GHEERAERT

Pr. Université de Joseph Fourier, Grenoble, France, Président

Dr. Pascal Mailley

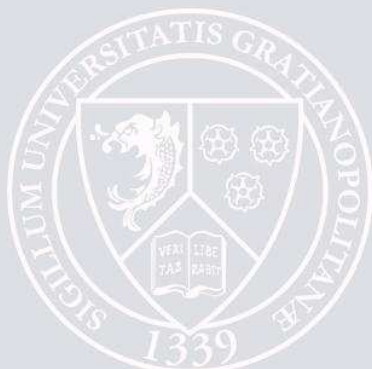
Chercheur au CEA Chambéry, France, Membre

Dr. Philippe BERGONZO

Directeur de recherches au CEA Saclay, France, Membre

Dr. Emmanuel SCORSONE

Chercheur au CEA Saclay, France, Membre



ACKNOWLEDGEMENTS

First and foremost, I would like to affirm that I am immensely indebted to my thesis co-director, **Dr Philippe Bergonzo**, director of research at CEA-Saclay, for his inspirational guidance, constant support and unceasing encouragement for the successful completion of my research work. Despite his hectic schedule, Philippe has always made himself available whenever I needed his inputs, comments, and feedback, and helped me to identify and to solve bottlenecks. I feel extremely privileged to work under him and to learn from his research expertise. It will never cease to surprise me to think of his profound confidence in my research ability and the magnitude of freedom, flexibility and opportunity he granted me during all these years of study and analysis under his guidance. I ever remain infinitely grateful to him.

I gratefully acknowledge my thesis director, **Dr Pascal Mailley**, formerly from University Joseph Fourier when my PhD started, and now research scientist at CEA-LITEN in Chambéry, for his invaluable advice and academic support. Pascal has always provided me his esteemed guidance, starting from my very first days at CEA till the end of my research work, with his profound knowledge in bio-chemistry, electrochemistry and material science. His vision, caring and commitment have generously contributed to my formation, work and success.

I have great pleasure in expressing my sincere gratitude to **Dr Emmanuel Scorsone** who was the day to day supervisor and who always provided me with the suggestions, questions, and puzzling remarks I needed to progress. He was with me through all the 3 years and I'm thankful for his wise supervision and involvement throughout the course of the research.

I am also grateful to **Dr Jacques de Sanoit**, who introduced me to the fascinating world of electrochemistry, as well as to several fascinating other worlds where electrolytes close to Chassagne-Montrachet could be involved. Without his support this work would have never taken shape. The help, suggestions and constructive criticism received from Prof **Jean-Charles Arnault** are also beyond measure and greatly appreciated.

I express sincere thanks to **Dr. Lionel Rousseau**, research scientist at ESIEE and **Prof. Blaise Yvert**, University of Bordeaux for extending their help at various phases of my research and for providing facilities to carry out part of my research activities at their institutes.

I am indebted to **Prof. Richard Jackman**, University College London and **Prof. Serge Picaud**, INSERM for their valuable suggestions and encouragements throughout my research work.

I would like to extend a very special thanks to my colleagues at CEA-Saclay, Bertrand, Celine, Christine, Hughes, Michal, Samuel, Alexandre, Amel (Inserm) and to all my friends for their timely help, co-operation and encouragement during the course of my study. I express my sincere regret in not mentioning individually many amazing persons who helped me in my pursuit, but I always nourish appreciation and gratitude for all well-wishers and benefactors.

Last but not least, I would like to extend my special appreciation to my parents for their perennial and contagious confidence in me and giving me the freedom to choose my career path. I dedicate my thesis to my beloved parents.

ABSTRACT

Boron doped diamond (BDD) electrodes are extremely promising in the field of biomedical applications as they exhibit a unique combination of properties. The thesis aims at developing new types of BDD microelectrodes and exploring their interests for electro-analytical and electrophysiological applications. Despite their superior electro-analytical properties, BDD electrodes are prone to fouling, which leads to a loss of electrode reactivity when used in biological fluids such as urine, waste waters, drinks, blood plasma, etc. A novel electrochemical treatment was developed to clean the electrode surface and to retrieve the initial reactivity, thereby enabling the use of BDD electrodes to long periods of measurements without degradation of the signal, thus significantly extending the field of monitoring and surveying applications up to domains where continuous analysis is required. The real novelty of the technique is that it does not require the use of a specific media and thus can be directly performed in the probed (bio-) fluid.

Microelectrodes in comparison with macro-electrodes offer higher sensitivity, lower background current, lower ohmic losses and higher signal-to-noise ratio. A robust, high-yield, reliable, and reproducible process for fabricating a thin-film BDD micro and ultra-microelectrode arrays (MEA) was developed using a novel lithographic technique, based on clean room processing on 4 inch substrates, thus offering considerable flexibility. For example, among other prototypes, BDD microelectrodes were developed as biosensors to quantify uric acid in human urine in quasi-real time. Although diamond film possesses good biocompatibility and excellent electrochemical properties, the low double-layer capacitance limits its application in electrophysiological applications. Increasing the charge injection limit was investigated by surface modification and nano-structuring. These include the synthesis of hybrid diamond-polypyrrole electrodes and nanograss BDD MEAs. Such high aspect ratio materials appear as excellent candidates for neurointerfacing applications such as for retinal implants.

RESUME

Le diamant dopé bore (BDD) est un matériau extrêmement prometteur pour applications biomédicales par son unique combinaison de propriétés. Cette thèse a visé le développement de nouvelles structures de micro-électrodes en BDD et l'étude de leur intérêt et leurs performances pour des applications électroanalytiques et électrophysiologiques. En dépit de leurs propriétés électroanalytiques très supérieures à d'autres matériaux d'électrodes plus conventionnels, les électrodes BDD sont sujettes au «fouling», i.e. l'apparition d'un film à la surface du diamant qui réduit la réactivité électrochimique. Ceci est très compromettant dans des milieux complexes comme l'urine, les eaux stagnantes, des boissons, le plasma sanguin etc. Ici, un nouveau traitement d'activation a été développé pour nettoyer la surface des électrodes et recouvrir leur réactivité initiale, donc il permet leur usage pour de longues périodes d'enregistrement sans dégradation du signal. Ceci permet l'usage de ce type d'électrodes, pour des domaines d'applications, pour le suivi continu d'analytes, sans entretien spécifique, en solutions complexes. La grande originalité de ces techniques d'activation est qu'elle peut être menée directement dans l'analyte lui-même.

En comparaison avec leurs équivalents en macro-électrodes, les microélectrodes permettent d'obtenir de plus grandes sensibilités, des courants résiduels moindre, des pertes ohmiques moindres, et donc des rapports signal à bruit meilleurs. Un procédé robuste et fiable a été optimisé pour la fabrication de réseaux de microélectrodes (MEA MicroElectrode Arrays) et d'ultra micro-électrodes, permettant par lithographie sur 4 pouces d'offrir une large flexibilité de fabrication. Par exemple, parmi d'autres prototypes, des microélectrodes BDD ont été utilisées pour applications de biocapteurs pour quantifier l'acide urique en temps quasi-réel. Bien que le diamant possède une très bonne biocompatibilité et des propriétés électrochimiques excellentes, la faible relative capacité de double couche limite leur application pour des applications électrophysiologiques. Des procédés de nanostructuration ont ainsi été mis au point pour accroître les limites d'injection de charge. Parmi les approches, des procédés hybrides à base de polypyrrole se sont révélés prometteurs, de même que des procédés de gravure pour former de la «nano-herbe» diamant, très intéressantes pour la fabrication de MEAs en BDD. Ces matériaux à fort rapport d'aspect apparaissent comme d'excellents candidats pour applications d'interfaces neuronales et notamment pour la fabrication d'implants rétiniens.

TABLE OF CONTENTS

Chapter	Page
I. INTRODUCTION	1
1.1 Synthesis of diamond	3
1.1.1 HPHT synthesis of diamond	3
1.1.2 CVD synthesis of diamond	4
1.2 Synthesis of doped diamond	5
1.3 MPECVD growth at the Diamond Sensors Laboratory	5
1.4 BDD film characterization	7
1.4.1 Structural and morphological characterization	7
1.4.2 Electrochemical characterization	10
1.5 BDD films for electrochemical sensors and biosensors	16
1.6 Theory of microelectrodes	18
Conclusion	21
Bibliography	22
II. Electrochemical activation of diamond electrodes	27
Introduction	29
2.1 Ageing and fouling of the electrode	29
2.1.1 Electrode ageing	29
2.1.2 Electrode fouling	32
2.2 Activation process	33
2.3 Activation in other synthetic electrolytes	36
2.4 Influence of pH, current density and number of pulses on activation	38
2.4.1 pH vs activation	39
2.4.2 Current density vs activation	40
2.4.3 Number of pulses vs activation	41
2.5 Surface analysis and activation mechanism	42
2.6 In-situ activation in biological fluids	48
Conclusion	50
Bibliography	51
III. Microelectrode: Design, fabrication and characterization	53
Introduction	55
3.1 Technological process	56
3.1.1 Design 1	56
3.1.2 Design 2	60
3.2 SEM Characterization	61
3.3 Electrochemical characterization	63

3.3.1 Background current.....	63
3.3.2 Steady state limiting current	65
3.3.3 Electrochemical impedance spectroscopy	67
3.4 All diamond microelectrode arrays	71
Conclusion.....	75
Bibliography.....	76
IV. Diamond microelectrodes: Electroanalytical application	79
Introduction	81
4.1 Electrochemical characterization of BDD microelectrode.....	82
4.2 Cyclic voltammogram of uric acid and ascorbic acid	84
4.3 Calibration curves for UA concentration	89
4.3.1 Model 1: Low ascorbic acid concentration.....	89
4.3.2 Model 2: High ascorbic acid concentration	91
4.4 Proposed model vs Spectrophotometric quantification	94
4.5 Automation of quantification procedure and in-situ cleaning.....	95
Conclusion.....	99
Bibliography.....	100
V. Diamond microelectrodes: Electrophysiological applications	103
Introduction	105
5.1 Electrophysiological characterization of MEA	106
5.1.1 Impedance measurement.....	106
5.1.2 Noise level measurement	108
5.1.3 Neural recording	108
5.2 Diamond microelectrode array as neural prosthesis: Retinal implants	110
5.2.1 Platinum microelectrode arrays	111
5.2.2 Diamond microelectrode arrays.....	114
5.3 Nanograss diamond MEA	117
5.3.1 Fabrication of nanograss MEA	117
5.3.2 SEM characterization.....	117
5.3.3 Electrochemical characterization	118
5.3.4 Electrophysiological characterization.....	121
Conclusion.....	122
Bibliography.....	124
VI. Conclusions and future perspectives.....	127
Introduction	129
5.1 Electrophysiological characterization of MEA	130
APPENDIX A	133

LIST OF TABLES

Table	Page
Table 1.1 Comparison of silicon and diamond physical characteristics	3
Table 1.2 Boron doped nanocrystalline layers synthesis conditions.....	7
Table 1.3 XPS components for ‘as grown’ BDD film	10
Table 2.1 k_0 after subsequent scan in human urine	32
Table 2.2 ΔE_p and k_0 values of ‘as grown’, aged and activated electrode	35
Table 2.3 k_0 after activation in salt solutions	37
Table 2.4 XPS components for ‘as grown’ electrode and after activation.....	42
Table 2.5 ΔE_p and k_0 of electrode with biofilm and after activation.....	46
Table 3.1 Mean value and standard deviation of i_{BG} , i_{lim} , and k_0	69
Table 3.2 Comparison of k_0 , i_{lim} , C_D and i_{BG} of 2 microelectrodes	71
Table 4.1 UA concentration: Proposed model vs Spectrophotometry	95
Table 4.2 Comparison of activated and non-activated measurements	97

LIST OF FIGURES

Figure	Page
Figure 1.1 Schematics of an MPECVD reactor	6
Figure 1.2 Raman spectra of different BDD films	8
Figure 1.3 Scanning electron microscopic image of BDD film	8
Figure 1.4 XPS Survey of BNCD thin film	9
Figure 1.5 Schematic diagram of 3 electrodes setup.....	11
Figure 1.6 Schematics of electrical double layer	11
Figure 1.7 Potential window of an ‘as grown’ electrode	12
Figure 1.8 CV of an ‘as grown’ BDD electrode in ferri/ferrocyanide	13
Figure 1.9 Randles equivalent circuit and Nyquist Plot.....	14
Figure 1.10 Nyquist plot of an ‘as grown’ BDD electrode	15
Figure 1.11 Schematics illustration of diffusion at a microelectrode	20
Figure 2.1 CV of an ‘as grown’ and aged electrode in ferri/ferrocyanide	30
Figure 2.2 Nyquist plot of an ‘as grown’ and aged electrode	31
Figure 2.3 CV in human urine.....	33
Figure 2.4 Comparison of CV in human urine and after activation.....	36
Figure 2.5 Stripping voltammogram for copper, manganese and zinc	36
Figure 2.6 pH dependence of activation process.....	39
Figure 2.7 Effect of the current density on the activation process	40
Figure 2.8 Impact of the number of pulses on the activation process	41
Figure 2.9 XPS of BDD electrode after activation.....	43
Figure 2.10 CV of BDD electrode before and after activation	44
Figure 2.11 Optical microscopic and SEM images biofilm	45
Figure 2.12 SEM images of electrode after activation.....	47
Figure 2.13 In-situ activation: k_0 after each trial.....	48
Figure 2.14 In-situ activation: J_1 after each trial	49
Figure 3.1 Diamond microelectrode fabrication process (Design 1)	57
Figure 3.2 SEM images of BDD films on titanium.....	58
Figure 3.3 Potential window and Nyquist plot of BDD films on titanium	59
Figure 3.4 Diamond microelectrode fabrication process (Design 2)	61
Figure 3.5 SEM image of an 8x8 UMEA along with the tracks	62
Figure 3.6 Potential window of BDD ultra-microelectrode.....	63
Figure 3.7 RGB model of an 8x8 electrode array: i_{BG} value.....	64
Figure 3.8 CV of BDD ultra-microelectrode in ferri/ferrocyanide	65
Figure 3.9 RGB model of an 8x8 electrode array: i_{lim} value.....	66
Figure 3.10 Nyquist plot of BDD ultra-microelectrode	67
Figure 3.11 Component of Randles’s circuit of ultra-microelectrode	68
Figure 3.12 RGB model of an 8x8 electrode array: k_0 value	69
Figure 3.13 Schematics of interconnected diamond MEA	72
Figure 3.14 SEM images of MEA and individual BDD conducting electrode.....	72
Figure 3.15 CV of boron doped diamond MEA.....	74

Figure 3.16 CV of boron doped diamond MEA in ferri/ferrocyanide	74
Figure 4.1 CV and Nyquist plot of BDD microelectrode	81
Figure 4.2 CV of uric acid and ascorbic acid in phosphate buffer solution	82
Figure 4.3 Proposed schematics for UA oxidation	83
Figure 4.4 CV of UA at various scan rate	84
Figure 4.5 CV of 1mM UA and AA (0, 250 and 500 μ M)	86
Figure 4.6 Second order curve fitting: low concentration of AA.....	87
Figure 4.7 Second order curve fitting: low concentration of AA.....	88
Figure 4.8 CV of 1.5 mM UA and AA (0, 2 and 4 mM)	89
Figure 4.9 Second order curve fitting: high concentration of AA	90
Figure 4.10 Second order curve fitting: high concentration of AA	91
Figure 4.11 CV of urine + UA added.....	93
Figure 4.12 CV of urine + UA added : with activation.....	94
Figure 4.13 Comparison of activated and non-activated measurements.....	95
Figure 5.1 8x8 BDD UMEA fixed on NanoZ device	106
Figure 5.2 Magnitude and phase of the impedance: BDD UMEA	107
Figure 5.3 Mouse embryonic hindbrain-spinal cord on UMEA	109
Figure 5.4 Recording of neural activity	109
Figure 5.5 Schematics of implantable 8 x 8 Pt microelectrode array	111
Figure 5.6 Pt soft implant (8 x 8 electrode array)	112
Figure 5.7 CV of implantable Pt microelectrode	112
Figure 5.8 Nyquist plot of implantable Pt microelectrode	113
Figure 5.9 CV of implantable Pt in ferri/ferrocyanide	113
Figure 5.10 Schematics of implantable 8 x 8 BDD microelectrode array	114
Figure 5.11 CV of implantable BDD microelectrode	115
Figure 5.12 Nyquist plot of implantable BDD microelectrode	116
Figure 5.13 CV of implantable BDD in ferri/ferrocyanide	116
Figure 5.14 SEM image of cross-section of BDD nanograss electrode.....	118
Figure 5.15 Nyquist plot of a nanograss diamond microelectrode	119
Figure 5.16 CV of nanograss diamond microelectrode.....	120
Figure 5.17 CV of nanograss diamond microelectrode in ferri/ferrocyanide	120
Figure 5.18 Electrode impedance measured for the 4 x 16 array.....	121
Figure 5.19 CV of nanograss diamond microelectrode in ferri/ferrocyanide	122

GLOSSARY

μ CD: Microcrystalline Diamond

AA: Ascorbic Acid

ARF: Acute Renal Failure

BDD: Boron Doped Diamond

BDD-PPy: Boron doped diamond – Polypyrrole

BNCD: Boron doped NCD

CE: Counter Electrode

CNT: Carbon Nanotube

CV: Cyclic Voltammetry

CVD: Chemical Vapor Deposition

DHAA: Dehydroascorbic Acid

DNP: Diamond Nanoparticles

DPV: Differential pulse Voltammetry

EC: Electrochemical

EDLC: Electric Double Layer Capacitor

EIS: Electrochemical Impedance Spectroscopy

HFCVD: Hot Filament CVD

HPHT: High-pressure/high-temperature

ICU: Intensive Care Unit

MEA: Microelectrode array

MPECVD: Microwave Plasma Enhanced CVD

NCD: Nanocrystalline Diamond

PBS: Phosphate Buffer Saline

PVA: Polyvinyl Alcohol

PVD: Physical Vapor Deposition

RE: Reference Electrode

SEM: Scanning Electron Microscopy

SIMS: Secondary Ion Mass Spectroscopy

SNR: Signal to noise ratio

TBATFB: Tetrabutylammonium tetrafluoroborate

TMB: TriMethyl Borane

UA: Uric Acid

UME: Ultra-microelectrode

UMEA: Ultra-microelectrode array

UNCD: Ultra Nanocrystalline Diamond

WE: Working Electrode

XPS: X-ray Photoelectron Spectroscopy

SYNOPSIS

Electrochemistry is the branch of science which deals with the relationship between electrical and chemical phenomena and laws of interaction between these phenomena. It is the study of reactions in which charged particles cross the interface between two phases of matter: electrode and electrolyte. One can find electrochemical reactions everywhere in nature and even within the human body. Natural processes such as photosynthesis, respiration, neural transmission are electrochemical processes. Everyday examples of electrochemistry in our daily life include batteries, hybrid automobiles, fuel cells, metal extraction, electroplating etc. Electrochemical sensors have been used extensively as chemical and biomedical sensing units. These electrochemical sensors include the most commonly used oxygen level monitors, glucose sensors etc. as well as novel DNA-based sensors. Advances in lithographic and technological processes have brought revolutionary changes in micro- and nano-structuring of electrochemical sensors. Recent inventions of novel conducting materials have also contributed towards better electro-analysis.

Doped diamond is one such material and it has become a major focus of research and development. Undoped diamond exhibits a high band gap, thus is, at room temperatures, electrically insulating. When doped with boron, this results in an electrode with remarkable electro-analytical properties which can be used to detect species in solution before oxygen and hydrogen evolution interfere with the analysis. Thus, conductive diamond electrodes take electrochemical detection into new levels and extend their usefulness to analytes which are not measurable with conventional electrode materials. There are two major approaches to fabricate doped diamond electrodes: chemical vapor deposition and high pressure high temperature methods. Finally, diamond, exhibiting specific bio-inert properties, appears as an ideal material for in-vivo sensing, implantation and other biomedical applications.

This thesis deals with the design, fabrication, characterization and application of boron-doped diamond electrodes and microelectrodes. Microwave plasma enhanced chemical vapor deposition is used to fabricate boron-doped nanocrystalline diamond.

This thesis is divided into 6 chapters:

In Chapter 1, the necessary background information and state of the art for this thesis work is introduced regarding the synthesis of diamond, importance of diamond in electrochemical sensors and biosensors. In addition, a brief introduction on the importance of micro-structuring the electrodes is given.

Electrode ageing and fouling are the two major concerns as they can lead to inaccurate readings and measurement failure. Hence electrode cleaning and activation is necessary. Chapter 2 deals with novel approaches that were developed during this work which enable the electrochemical activation of diamond electrodes. A comparison between the existing activation techniques and our novel pulsed activation technique is described in detail. We have also investigated the influence of different parameters such as the duration of the pulses, amplitude of current density, pH of the solution, etc. on electrode reactivity. As the diamond electrodes are targeted for biomedical applications, an in-situ activation technique was developed where the electrode can be cleaned within the probed fluid itself. Examples of some in-situ activation techniques in bodily fluids are also presented.

Microelectrodes possess superior properties over macroelectrodes that are highly favorable for electro-analysis such as: low ohmic drop, steady-state voltammetric behavior, reduced background current etc. Chapter 3 is dedicated to the design, fabrication and characterization of microelectrode and ultra-microelectrode arrays. The chapter describes various design approaches and the optimization of technological processes in order to produce the microelectrode arrays with the best performances. The microelectrodes were characterized using scanning electron microscopy and electrochemical tools including cyclic voltammetry and electrochemical impedance spectroscopy. Electro-analytical and electrophysiological applications of the fabricated microelectrodes are described in chapters 4 and 5 respectively.

Chapter 4 is centered on a classical electro-analytical application based on diamond microelectrode where the uric acid concentration in human urine is selectively determined in the presence of ascorbic acid. This innovative electrochemical technique is based on fast cyclic voltammetry and the quantification technique is explained in detail. Chapter 4 also describes the

application of the in-situ activation technique explained in chapter 2, where the electrodes were reactivated within human urine, thereby opening the way towards automatic quantification of uric acid quantification with in-situ cleaning.

Chapter 5 focuses on electrophysiological applications of diamond microelectrodes where they are used to electrically stimulate neurons and to record the neural activity. Although the low double layer capacitance of a diamond electrode is an advantage in electrochemical recording, the electrode should possess a large storage capacitance for electrical stimulation. Also for neural recording, the impedance of the electrode has to be low in order to have higher signal to noise ratio. The charge injection limit and signal-to-noise ratio were increased by techniques such as surface modification (boron doped diamond – polypyrrole composite) and nano-structuring (nanograss). This chapter also describes the fabrication and characterization of flexible diamond electrodes for eye implants.

The work is summarized in Chapter 6 along with a review of the scope of future studies.

SYNOPSIS EN FRANCAIS

Introduction

Le diamant est un matériau précieux, objet de toutes les convoitises. Sa valeur est conditionnée par sa rareté, sa transparence ainsi que son éclat...Sa présence symbolise bien souvent un amour éternel.

Mise à part son utilisation la plus connue, à savoir la joaillerie, le diamant se trouve également au cœur de l'innovation scientifique. Constitué exclusivement d'un arrangement particulier de carbone, ce matériau est un élément quasiment inaltérable et ses propriétés semi-conductrices en font un matériau recherché en électronique. Il fait également preuve d'une grande résistance à la température et aux rayonnements ionisants. Beaucoup plus isolant que le verre, il acquiert des propriétés conductrices après dopage au bore (dopage de type p) ainsi il en viendra à posséder une forte réactivité électrochimique avec une large fenêtre de potentiel, pouvant atteindre plus de trois volts en solution aqueuse. Grâce à ce fabuleux Curriculum Vitae, le diamant se trouve positionné au carrefour de multiples technologies innovantes. Le laboratoire LCD du CEA LIST, spécialisé dans la synthèse de ce matériau le décline au sein de plusieurs disciplines comme la dosimétrie médicale, la détection de rayonnements ionisants, la dissipation thermique, les nanoparticules, les transducteurs, les matériaux pour bio interfaces et enfin l'électrochimie analytique.

Dans le cadre de mes études doctorales, j'ai eu l'opportunité d'effectuer mes travaux de recherches au sein du Laboratoire Capteurs Diamant du CEA LIST. L'intérêt particulier que je porte au domaine de la Recherche m'a permis d'appréhender le sujet proposé avec beaucoup de motivation.

Mes travaux sont présentés dans cette thèse, qui est articulée de la manière suivante, après une brève présentation du laboratoire LCD et une introduction au matériau diamant, le chapitre 1 aura d'une part pour but d'éclairer le lecteur sur les méthodes de synthèse du diamant et sur l'importance de ce matériau dans des applications telles que les capteurs électrochimiques et les biocapteurs. D'autre part ce chapitre apportera une brève introduction sur la micro-structuration des électrodes en diamant dopé au bore. Aussi l'un des objectifs de cette thèse a été de développer une méthode de traitement EC (électrochimique) simple et rapide qui peut être utilisée pour récupérer la réactivité perdue des électrode BDD (Diamant dopé au bore), améliorant ainsi leur réutilisation, sans dégradation du signal, même après une longue période de mesures. Le chapitre 2 décrit un nouveau processus d'activation EC, en régime impulsionnel Redox réalisé par une série d'impulsions alternativement cathodiques et anodiques, appliqué sur des électrodes BDD. Ce traitement apportera un changement de la surface de l'électrode, cela peut être mis en évidence par XPS et par caractérisation électrochimique. L'influence de la densité de courant, du pH, et du nombre d'impulsions sur l'activation EC sera développée. Quelques exemples d'activation dans les fluides biologiques et synthétiques seront également inclus dans

ce chapitre. Ensuite le chapitre 3 sera consacré à l'explication des différents processus de fabrication des microélectrodes et des MEA. Ces électrodes ont été caractérisées par MEB et par des méthodes électrochimiques (Voltamétrie cyclique CV et spectroscopie impédance électrochimique EIS). Cela a permis d'apprécier les performances des électrodes à savoir les courants limites (i_{lim}), les constantes de transfert de charge (k_0), les fenêtres électrochimiques et les courants de fond (i_{BG}). Ces deux méthodes d'analyses électrochimiques sont les techniques les plus efficaces pour détecter d'éventuelles fissures ou discontinuités dans la couche isolante de l'électrode BDD UME, ainsi que pour l'analyse de ses propriétés électrochimiques. En ce qui concerne le chapitre 4, il traitera les études effectuées sur la microélectrode BDD. La microélectrode BDD d'un diamètre de 40 μm et en forme de bande, fabriquée selon notre technologie (voir chapitre 4), a été utilisée pour la détection sélective et sensible de l'acide urique (UA) en présence de quantités faibles ou élevées d'acide ascorbique (AA). La capacité de la double couche de diamant, réduit le courant de fond et augmente le signal vers le ratio initial. Ces microélectrodes indiquent une diminution de la chute ohmique, une couche de diffusion hémisphérique et permettent la mise en place rapide d'un signal statique en comparaison avec les macro-électrodes. Ce chapitre traite de la caractérisation électrochimique de ces microélectrodes, de la quantification de l'acide urique en présence d'une grande ou faible concentration d'acide ascorbique et de différentes techniques de nettoyage in-situ. Enfin l'électrophysiologie est l'étude des propriétés électriques de cellules et de tissus biologiques, elle implique la mesure de la variation de tension d'une entité biologique. Il s'agit d'une approche puissante qui permet d'une part l'étude de l'activité électrique des cellules animales, pour comprendre le fonctionnement du système nerveux, du cerveau ou de l'hypothalamus, et d'autre part le diagnostic et le traitement des troubles du système nerveux. Des réseaux de microélectrodes extracellulaires permettent de mesurer directement l'activité électrique des neurones. Les MEA fabriquées en utilisant la technique décrite dans le chapitre 3, ont été utilisées pour des mesures électro-physiologiques in-vitro. Le chapitre 5 décrit le processus de fabrication et la méthode de caractérisation d'une prothèse neurale: implants rétiniens constitués de MEA BDD. Les études sur l'amélioration de la limite d'injection de charges sont aussi incluses dans ce chapitre, elles se font par modification de surface et nano-structuration de l'électrode.

Le Laboratoire Capteurs Diamant du CEA

Le CEA :

Le CEA est un organisme public de recherche créé en 1945 par une ordonnance du général de Gaulle. Cette institution est actuellement un acteur majeur dans la recherche française et européenne et pionnier en matière d'innovations technologiques. Elle emploie actuellement plus de 15 000 salariés sur ses centres répartis dans toute la France.

Son domaine d'activité se situe dans cinq grands domaines qui sont :

- le nucléaire civil (développement des technologies de réacteurs, retraitement des combustibles nucléaires usés et traitement des déchets nucléaires)

- la recherche technologique (développement des technologies du futur en partenariat avec des groupes industriels : cela concerne le développement de nouveaux matériaux, les technologies pour l'information, la communication, la santé...)

- la défense nationale (armes atomiques, systèmes de propulsion des navires et sous-marins à propulsion nucléaire)

- sciences de la matière et de l'univers (recherches fondamentales sur la structure de l'univers, les nanosciences, l'énergie de fusion, l'astrophysique...)

- sciences du vivant (amélioration de l'imagerie médicale, biologie moléculaire...)

Le laboratoire Capteur Diamant (LCD) :

Le laboratoire LCD est axé sur la recherche technologique pour les applications industrielles et biomédicales. Il est rattaché à un département nommé DCSI (Département Capteurs, Signal et Information) lui-même étant un élément du LIST (laboratoire intégration des systèmes et des technologies). La particularité du LCD concerne l'étude du diamant de synthèse pour le développement de capteurs innovants (chimique, rayonnement, biologique, radioactivité...). Actuellement, vingt-sept personnes travaillent au LCD ; quatorze permanents, le reste de l'équipe est constitué de post doc, thésards, ingénieurs en alternance et stagiaires.

Le matériau diamant

Structure du diamant

Le diamant est l'une des trois formes allotropiques du carbone avec le graphite et le fullerène. Alors que le graphite se trouve sous forme de feuillets hexagonaux et le fullerène sous la forme de sphères, d'un ellipsoïde ou d'un tube composé de feuillets, le diamant se présente sous la structure cristalline cubique faces centrées (CFC). La structure diamant comporte huit atomes de carbone par maille élémentaire.

Chaque atome de carbone est lié de façon covalente aux quatre autres: ils sont dits hybridés sp^3 . La forme sp^3 est une forme métastable du carbone; la forme stable du carbone étant le graphite où le carbone trivalent a une hybridation sp^2 .

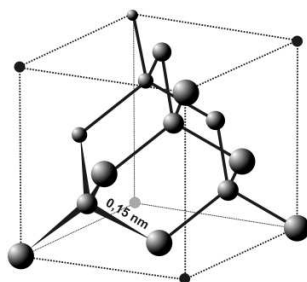


Figure 1 : Maille élémentaire du diamant

A l'état naturel, le diamant se forme sous la croûte terrestre à des profondeurs telles que les températures et pressions atteignent respectivement 1100 à 1400°C sous 4 à 6 GPa, conditions nécessaires à la cristallisation en une structure dérivée du CFC du carbone qui le compose.

Propriétés du diamant

Le réseau cristallin du diamant est très dense (1,54 Å entre chaque atome voisin). Ce matériau possède un fort nombre d'atomes par unité de volume ($1,76 \cdot 10^{23}$ atomes. cm^{-3}). Les fortes énergies de cohésion atomiques (7,3 eV/atome) et sa très faible distance interatomique font du diamant un matériau très résistant, électriquement isolant et très bon conducteur thermique ($20 W.cm^{-1}.K^{-1}$, 5 fois plus élevée que celle du cuivre). Il est inerte vis-à-vis d'agents agressifs aussi divers que sont les acides, les bases, les oxydants et réducteurs. Le diamant est également très résistant aux rayonnements ionisants (dose intégrée maximale de 2,5 MGy pour le rayonnement gamma de 1 MeV). De plus, son utilisation dans le domaine de la dosimétrie médicale est envisageable car son numéro atomique ($Z = 6$) est très proche de celui du tissu humain ($Z = 7,1$) [Tromson, 2000]

Le tableau ci-dessous récapitule les principales caractéristiques physiques du diamant et les compare avec celles du silicium [Jany, 1998].

Caractéristiques	Diamant	Silicium
Durée de vie des porteurs de charges	100 ps à 10 ns pour le diamant polycristallin et 30 ns pour le diamant monocristallin	0,10 μ s
Densité atomique	$1,76 \cdot 10^{23}$ atomes.cm ⁻³	$4,96 \cdot 10^{22}$ atomes.cm ⁻³
Densité	3,51	2,33
Largeur de bande interdite	5,5 eV	1,1 eV
Résistivité	de 10^{12} Ω .cm à 10^{15} Ω .cm	$5 \cdot 10^5$ Ω .cm
Mobilité des électrons à 300 K	$2000 \text{ cm}^2 \cdot \text{V}^{-1} \cdot \text{s}^{-1}$	$1350 \text{ cm}^2 \cdot \text{V}^{-1} \cdot \text{s}^{-1}$
Énergie de cohésion	7,37 eV par atome	4,63 eV par atome
Énergie de création paire électron/trou	13 eV	3,6 eV
Température maximale d'utilisation	> 500 °C	50 °C

Tableau 1

Caractéristiques physiques du diamant comparées à celles du silicium

Le diamant naturel est classifié en fonction de sa teneur en impuretés:

Type Ia : 0,1 % d'azote sous forme d'agrégats. La majeure partie (98 %) des diamants extraits des mines sont de ce type.

Type Ib : azote en position substitutionnelle, couleur jaune.

Type IIa : très faible quantité d'azote. Il représente moins de 1 % de la production mondiale.

Type IIb : diamant semi-conducteur. La conduction est due à la présence de bore, qui donne une couleur bleutée au diamant. Il est extrêmement rare dans la nature (< 0,1 %).

La fabrication de capteurs à partir de diamants naturels est limitée par différents facteurs dont l'impossibilité de trouver deux diamants naturels de caractéristiques physiques identiques (répartition et concentration différentes en impuretés et défauts).

Afin de contrôler les impuretés et la taille du diamant, différentes techniques de synthèses ont pu être développées. Au laboratoire LCD, la technique MPCVD (Dépôt chimique en phase vapeur assistée par plasma micro-onde) est utilisée pour la synthèse du diamant dopé au bore (Dopage type p).

Le diamant poly-cristallin est synthétisé sur un substrat en silicium, ce qui permet de réaliser des films de grande surface à moindre coût (jusqu'à 10 cm de diamètre). La structure microscopique du diamant poly-cristallin est composée de grains.

Contexte de l'étude

Le diamant de synthèse est très prisé dans le monde de la recherche. Des techniques de synthèse ont été perfectionnées lors de ces quarante dernières années. Ces avancées scientifiques ont rendu ce matériau disponible [Bundy, 1955].

Dans le cadre de cette étude, nous nous intéressons au diamant de synthèse (procédé CVD assisté par micro-ondes) et plus précisément celui dopé au bore électrochimiquement actif. En effet, le diamant intrinsèque est un matériau semi-conducteur avec un grand gap (5.5 V) et pour qu'il puisse être utilisé en électrochimie, un dopage est nécessaire afin de le rendre conducteur électrique. Grâce à ce dopage (dopage au bore de type p), ce matériau devient électro-actif, une nouvelle propriété qui figure dans une longue liste d'autres caractéristiques à la fois exceptionnelles et originales, notamment une large fenêtre de potentiel (plus de 3 V en milieu aqueux), de bas courants résiduels (quelques μA), une surtension importante à la réduction de l'oxygène dissout ainsi qu'une impressionnante stabilité chimique [Fujishima, 2005, Kraft, 2007, Pleskov, 2006]. Plus récemment c'est pour sa bio-inertie que le diamant se voit propulsé dans la sphère de la communauté scientifique. Cette propriété élargit encore le vaste champ des applications du diamant qui s'étend de la détection de substances explosives et polluantes à l'état de traces [de Sanoit, 2009] à la réalisation de prothèses neuronales [Artificial Rectina, 2001, DREAMS, 2006, MEDINAS, 2008]. Cependant, pour pouvoir réaliser toutes ces applications, l'expérimentateur doit posséder une bonne connaissance et une maîtrise parfaite de la synthèse du diamant et de son dopage. C'est dans ce cadre qu'il est proposé d'étudier les propriétés du diamant avec différents taux de dopage au bore et de les caractériser par les méthodes citées plus bas.

Synthèse du diamant

Au vu des propriétés intéressantes du diamant pour la recherche et l'industrie, les chercheurs se sont naturellement intéressés à sa synthèse. Le premier diamant artificiel provient de Stockholm et date de 1953 [E. Vanhove, 2010].

Dans le cadre de cette étude la synthèse du diamant se fera par dépôt en phase vapeur assisté par plasma micro-onde (MPCVD) dans une enceinte métallique sous vide qui constitue le réacteur. Le réacteur est identifié au laboratoire sous le nom de BAOBAB.

La méthode MPCVD nécessite au moins deux gaz, le premier apporte les atomes de carbone, le second les atomes d'hydrogène. Usuellement pour l'apport de carbone, le méthane (CH_4) est utilisé, quant à l'hydrogène (H_2) il sera fourni par le

second gaz (dihydrogène H_2). La pression de l'enceinte est comprise entre 30 et 100 mbar.

Ces deux gaz forment un mélange gazeux qui sera ionisé grâce à un champ électrique intense. Ce champ électrique est produit par l'énergie micro-onde. Le mélange gazeux se transforme alors en plasma. Plusieurs facteurs influencent la qualité du matériau produit : la pression dans l'enceinte, la température du substrat ($900\text{ }^\circ\text{C}$), la puissance micro-onde (quelque kW) et la composition du mélange gazeux. (Cf figure 2)

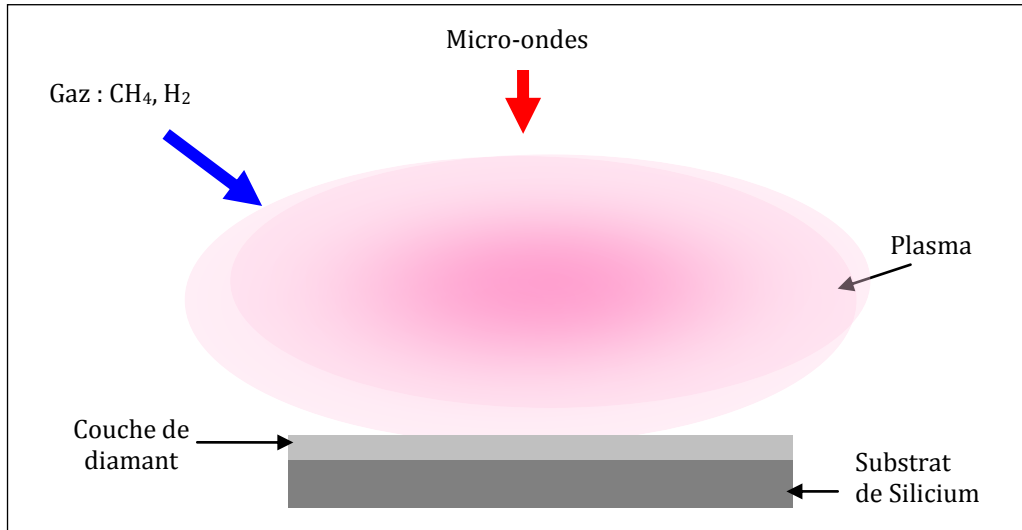


Figure.2 : Schéma de principe de la méthode MPCVD

La première étape de synthèse est la nucléation. Elle consiste à créer des germes de diamant sur un substrat de silicium. Ce dernier est utilisé sous la forme de disques de 5 cm de diamètre recouvert de nanoparticules de diamant par spin coating afin d'initier la nucléation.

A partir des sites de nucléation, les germes de diamant croissent pour finalement se rejoindre (coalescence) et ainsi former un dépôt poly-cristallin (Cf. figure 3).

Une nouvelle phase débute alors, elle est nommée phase de croissance du film. Les atomes de carbone vont venir se lier à la surface des cristaux afin de les faire grandir.

Le film possède une structure colonnaire (Cf. figure 3).

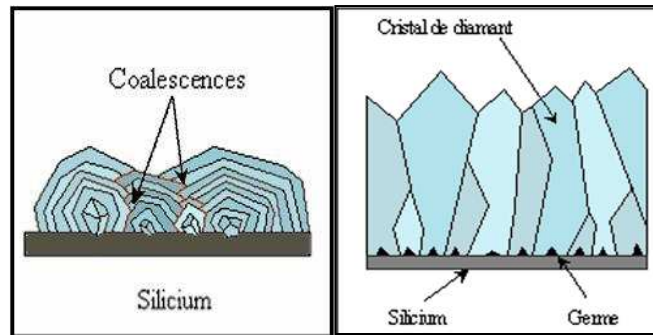


Figure. 3: Coalescence des cristaux de diamant et structure colonnaire obtenue après croissance du film

Le but de cette étude étant l'utilisation du diamant de synthèse pour des applications de type capteurs électrochimiques, il est nécessaire de le doper au bore afin qu'il acquière les propriétés de conduction électrique et de réactivité électrochimique. Pour se faire, il sera dopé au bore (dopage de type p) via l'injection du gaz TMB (triméthylbore) lors de la croissance. La concentration en bore qui sera inclus dans le matériau sera contrôlée par l'addition d'oxygène sous forme gazeuse (avec un gradient d' O_2/H_2 de 0 à 0.5 %) à débit de TMB constant. (Cf. le tableau 2, pages 10)

Caractérisation du matériau diamant dopé au bore

Nous avons choisi deux méthodes pour caractériser la morphologie du diamant dopé au bore. La première est la microscopie électronique à balayage (MEB) qui permet l'observation de l'évolution de la structure poly-cristalline pour différentes conditions de croissance. La deuxième méthode choisie est la spectrométrie de masse d'ions secondaires (SIMS) qui a pour but de mesurer le taux de dopage en bore dans l'épaisseur du matériau. (cf. annexe 4°).

Caractérisation électrochimique

La caractérisation électrochimique a pour but de tester la réactivité de surface du diamant de synthèse dopé au bore afin d'en déterminer la propriété fondamentale (vitesse de transfert de charge k_0 mesurée avec un couple redox rapide). Deux méthodes ont été choisies; une méthode dite « à balayage » nommée **voltamétrie cyclique** et une méthode dite « à modulation » nommée **spectroscopie d'impédance électrochimique**.

Conditions de croissance du diamant dans le réacteur Baobab type MPCVD

Dans le tableau ci-dessous, sont regroupés, les conditions de croissance des échantillons de diamant de synthèse sur substrats de 5 cm de diamètre, l'épaisseur de la couche diamant obtenue, ainsi que, la valeur du taux dopage en bore mesuré par SIMS. Le but recherché est de vérifier qu'il est possible de contrôler le taux de dopage en bore du diamant en faisant varier la concentration en oxygène dans le réacteur à concentration de TMB constante.

Dépôts	H ₂ /C H ₄ (sccm)	TM B (sccm)	O ₂ (sccm)	Puissance/Pression	Température (°C)	Épaisseur (nm) pesée	Dopage estimé / SIMS
B1203 12	100 / 1	12	0	30 mbar 1.5 kw	800	280	2.10 ²⁰
B1503 12-a	100 / 1	12	0.15	33 mbar 1.5 kwatts	820	320	4.10 ¹⁹
B1303 12-a	100 / 1	12	0.25	30 mbar 1.5 kw	800	290	2.10 ¹⁹
B1503 12-b	100 / 1	12	0.35	33 mbar 1.5 kw	790	370	8.10 ¹⁸
B1303 12-b	100 / 1	12	0.5	35 mbars 1.65 kw	810	330	5.10 ¹⁸
B2402 12	100 / 1	12	1	35 mbar 1.65 kwatts	750	350	2.10 ¹⁷

Tableau 2

Conditions de croissance des échantillons de diamant utilisés lors des expériences.

Mise en œuvre d'une électrode de diamant

Les films de diamant sortis du réacteur Baobab après caractérisation par SIMS et MEB sont montés sous la forme d'électrodes afin de pouvoir être caractérisés par les méthodes électrochimiques CV et EIS. Le montage des électrodes requiert un certain nombre d'éléments (Cf. Figure 4). Les différentes étapes du montage des électrodes sont décrites dans le mode opératoire suivant :

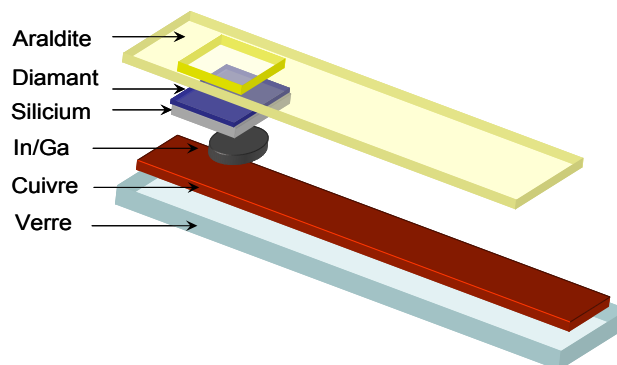


Figure 4 : Schéma éclaté de l'électrode de diamant de synthèse dopé au bore montée

Étape 1 : Prendre une lame de microscope en verre et la couper en deux parties dans le sens longitudinal. Nettoyer un des morceaux à l'éthanol absolu (95 %) afin d'enlever toutes traces de graisse. Coller une bande de cuivre adhésive sur une des faces afin de former un contact électrique. Eliminer le surplus de bande cuivre afin d'obtenir un assemblage de même type que celui montré ci-dessus. Effectuer un dernier nettoyage à l'éthanol.

Étape 2 : Prendre à la manière d'une plume d'écriture un peu de mélange eutectique indium/gallium à l'aide d'un trombone déplié. Gratter vigoureusement la surface du cuivre sur environ 1 cm^2 afin de former un alliage avec ce dernier. Pratiquer de la même façon sur la surface arrière (opposée à celle du diamant) du substrat de silicium afin d'éliminer la couche superficielle de SiO_2 qui sera alors remplacée par un fin dépôt d'alliage eutectique. Cette technique particulière permet d'assurer un contact de type ohmique dans l'électrode.

Étape 3 : A l'aide d'une pince brucelles, poser délicatement le substrat (coté silice et eutectique) sur le cuivre recouvert d'eutectique indium/gallium. A l'aide d'un coton tige, on appuiera délicatement sur la surface de diamant afin de solidariser l'ensemble du montage.

Étape 4 : Enrober le montage à l'aide d'une résine époxy (Araldite rapide bi-composants) tout en ménageant une fenêtre de diamant et en laissant à nu le haut du contact électrique en cuivre. Laisser polymériser 24 heures à température ambiante et à l'abri de la poussière

Mesure de la surface de l'électrode

La surface des électrodes a été déterminée par une photographie des électrodes posées sur une mire en papier quadrillé. Après découpage des images obtenues et d'une surface de référence, nous avons pesé les différents échantillons de papier sur une balance de précision. La mesure de masse des photographies des électrodes et des échantillons de référence de surface connue a permis de déterminer l'aire des électrodes de diamant. Nous avons admis que le grammage du papier était constant

Caractérisations électrochimiques

Les caractérisations électrochimiques ont été réalisées d'une part par spectroscopie d'impédance électrochimique (EIS) au potentiel de repos et d'autre part par voltamétrie cyclique. L'électrolyte utilisé est composé dans tous les cas par une solution équimolaire de ferro-ferricyanure de potassium ($K_3Fe(CN)_6$ et $K_4Fe(CN)_6$) à la concentration de 10^{-3} M. Le sel de fond employé est le chlorure de potassium (KCl) à la concentration de 0.5 M.

L'activation électrochimique des électrodes de diamant dopées au bore a été effectuée en régime impulsionnel (± 5 mA, 0.1 s, 30 cycles) dans un électrolyte composé de Coca Cola Light Décaféiné.

Protocole opératoire

Le protocole opératoire employé pour l'étude des différents échantillons de diamant dopé au bore a été le suivant :

- 1) Mesure EIS du matériau « as grown » afin de mesurer la réactivité initiale du matériau. Trois mesures successives sont effectuées afin d'évaluer la reproductibilité ou de mettre en évidence une évolution de la réactivité de l'électrode en cours de mesure.
- 2) Mesure par voltamétrie cyclique entre - 0.3 et + 0.3 V/ECS dans une gamme de vitesses de balayage s'étendant de 25 à 150 mV/s. Pour une vitesse de balayage donnée, quatre cycles de mesure sont effectués. Seul le dernier cycle sera systématiquement enregistré.
- 3) Mesure EIS « Après CV » afin de comparer la réponse de l'électrode avant et après la mesure de voltamétrie cyclique. Trois mesures successives sont effectuées afin d'évaluer la reproductibilité de la réponse de l'électrode.
- 4) Activation électrochimique du matériau en régime impulsionnel Redox par une série d'impulsions alternativement cathodiques et anodiques (± 5 mA, 0.1 s, 30 cycles) dans un électrolyte composé de Coca Cola Light Décaféiné.

- 5) Mesure EIS « Après activation électrochimique » afin de comparer la réponse de l'électrode avant et après l'activation électrochimique. Trois mesures successives sont effectuées afin d'évaluer la reproductibilité de la réponse de l'électrode.
- 6) Mesure de voltamétrie cyclique entre - 0.3 et + 0.3 V/ECS dans une gamme de vitesses de balayage s'étendant de 25 à 150 mV/s. Ceci permettra de comparer la réponse de l'électrode en voltamétrie cyclique « avant » et « après activation électrochimique ». Pour une vitesse de balayage donnée, quatre cycles de mesure sont effectués. Seul le dernier cycle sera systématiquement enregistré.
- 7) Mesure EIS « Après activation électrochimique et CV » afin de comparer la réponse de l'électrode « *après l'activation électrochimique* » et « après activation + CV ». Trois mesures successives sont effectuées afin d'évaluer la reproductibilité de la réponse de l'électrode.

L'activation électrochimique

L'activation électrochimique ne semble pas efficace pour des teneurs en bore dans le matériau minimal. En effet, en dessous d'un taux de dopage de 10^{20} B/cm³ la méthode devient inefficace voir nuisible pour l'intégrité des propriétés électrochimiques des électrodes.

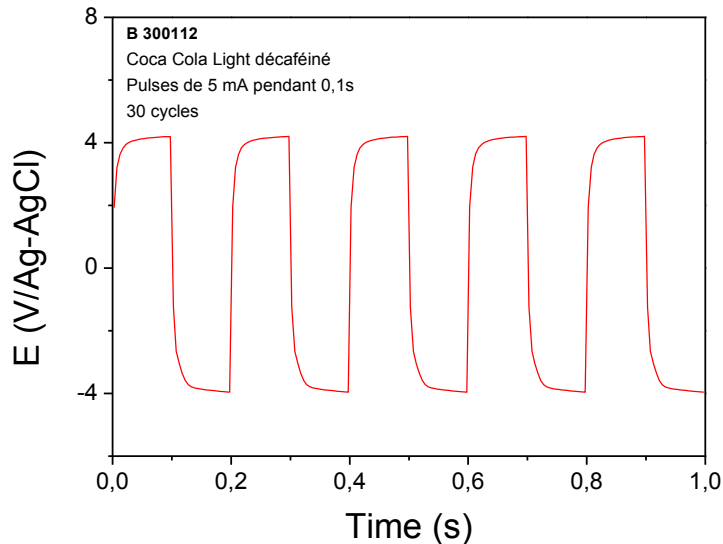


Figure 5

Un exemple d'activation électrochimique impulsionnelle d'une électrode de diamant dopée au bore :

La constante de vitesse de transfert de charges k_0

La réactivité électrochimique d'un matériau électro-actif est estimée grâce à l'indicateur constante de vitesse de transfert de charges, noté k_0 et de dimension cm⁻¹. Cet indicateur, intégrant dans son calcul à la fois la résistance de transfert de charges et la surface active des électrodes, il sera aisé de comparer les propriétés électrochimiques d'électrodes de surfaces différentes. On estime que la réactivité d'une électrode mesurée à l'aide d'un couple électrochimique rapide (i.e Fe(CN)₆^{3-/4-}) est satisfaisante si la valeur de k_0 se trouve être supérieure à 10⁻³ cm/s.

Conclusion

Dans le premier chapitre, les différentes techniques de croissance du diamant dopé au bore et les méthodes de caractérisation de ce matériau ont été décrites. Les électrodes de diamant dopé au bore ont été synthétisées à partir d'un mélange gazeux comprenant du méthane, de l'hydrogène et du TMB (tri-méthyl borane) par méthode MPCVD (dépôt en phase vapeur assisté par plasma micro-onde). Les propriétés physiques et chimiques de la couche mince du diamant synthétisé, ont été évaluées en utilisant la spectroscopie Raman, XPS, MEB, CV et EIS. Les électrodes de diamant fortement dopé au bore présentent une excellente réactivité, ce qui en fait des candidats idéaux pour des applications électro-analytiques et des applications en tant que biocapteurs.

Il a été démontré, que la méthode d'activation développer pendant mes recherches, permet de récupérer la réactivité de l'électrode BDD perdue au court du temps. Cette perte de réactivité est due au contact de l'électrode avec l'air ou encore à un encrassement de cette dernière par une solution. En ce qui concerne cette méthode d'activation impulsionnelle, plus la densité de courant sera élevée et plus le temps d'activation sera court, meilleur sera le résultat. En ajustant les paramètres mentionnés ci-dessus (densité de courant, durée d'impulsion, nombre d'impulsions et type d'électrolyte), on peut augmenter la constance de transfert de charge k_0 , pour atteindre des valeurs supérieures à $0,01 \text{ cm.s}^{-1}$. L'autre avantage de cette technique est qu'on peut réutiliser l'électrode BDD sans craindre de perdre ses caractéristiques. Contrairement à d'autres prétraitements plus classiques rapportés dans la littérature, tels que les traitements anodiques, cathodiques ou thermiques, ce nouveau prétraitement électrochimique est relativement simple, rapide et nécessite un minimum d'énergie.

Un nouveau procédé lithographique, reproductible et avec un rendement élevé, a été utilisé pour fabriquer les UMEA. Des BDD UMEA, appropriées pour une utilisation dans des capteurs électrochimiques, ont été préparées par une technique de micro-fabrication compatible avec la technologie standard de salle blanche. La caractérisation topographique détaillée et l'étude électrochimique des UME individuelles n'ont révélé que quelques électrodes défectueuses, dans une plateforme contenant plusieurs microélectrodes. Pendant les tests électrochimiques, les UME ont été exposées à un faible courant de base, presque théorique, à un état d'équilibre limitant et à un taux de transfert d'électrons rapide (aux alentours de $0,01 \text{ cm s}^{-1}$). L'amélioration de ces deux valeurs physiques a été réalisée grâce à l'activation électrochimique. L'objectif de ce travail, a été de développer des plateformes de bio-détection pour le suivi d'activités neuronales en l'électrophysiologie. Les applications électro-analytiques et électro-physiologiques de ces microélectrodes et de ces plateformes AME seront plus détaillées dans les chapitres 4 et 5.

La détermination sélective de l'acide urique en présence d'acide ascorbique a été réalisée en utilisant la microélectrode BDD sans y apporter des modifications. La comparaison de la technique de quantification électrochimique EC et de la technique

spectrophotométrique, montre qu'une mesure précise peut être faite en utilisant les deux modèles proposés. Cette technique met en évidence que le potentiel, des microélectrodes BDD considérée comme un capteur électro-analytique, est du à la faible capacité de la double couche de l'électrode qui résiste à une haute densité de courant et qui possède une résistance à la corrosion. Le traitement électrochimique récupère la réactivité perdue d'une électrode qui a été soit séchée à l'air, soit encrassée par un milieu avec lequel elle aurait été mise en contact. Pour ce traitement, il n'est pas utile d'utiliser un réactif ou une solution spécifique. Cette technique permet la réutilisation de la microélectrode BDD et même son activation dans l'urine même. Cela démontre la possibilité d'automatisation de la quantification de l'acide urique car l'électrode peut être activée directement dans l'urine, donc elle peut être utilisée pour une surveillance continue et pendant une longue période d'analyse. Le temps nécessaire pour l'activation est de 300 ms et le temps nécessaire pour la voltamétrie cyclique CV (20 Vs^{-1}) est inférieur à 200 ms.

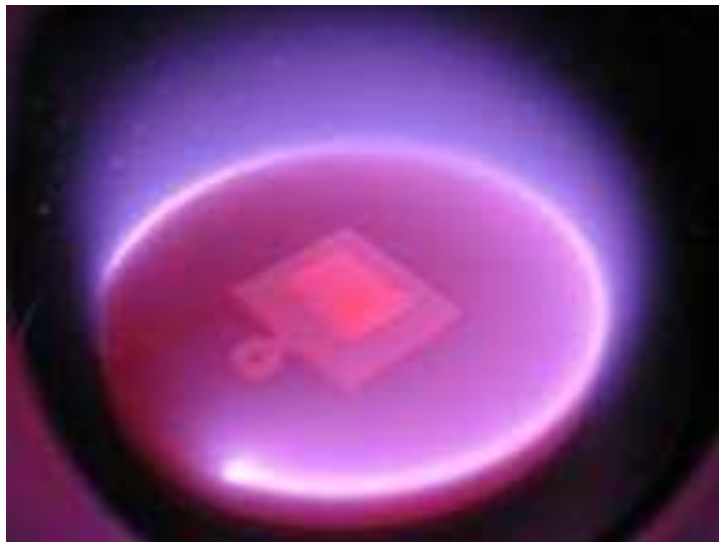
Le diamant peut être une prothèse neurale avec d'excellentes propriétés physiques et chimiques et possède aussi une bonne biocompatibilité. Dans ce chapitre, plusieurs approches ont été proposées pour améliorer les propriétés électriques du diamant afin d'en faire une électrode idéale pour des applications électrophysiologiques. Bien que les microélectrodes BDD-ppy électrodes ne peuvent pas être utilisés en tant que prothèse neurale, cette étude a permis l'utilisation de ce matériau dans d'autres domaines de recherche tels que le stockage d'énergie et de transmission. Les microélectrodes BDD nanograss, présentent de très larges limites d'injection de charge et par rapport au nitrure de titane et l'oxyde d'iridium, le diamant possède une meilleure biocompatibilité et stabilité microstructurale. L'augmentation du nombre d'électrodes, la conception des formes d'électrodes plus appropriées (jusqu'à présent, les formes étaient toutes planaires) et une modification surface de l'électrode peuvent faire des microélectrodes BDD nanograss un bien meilleur dispositif avec des propriétés supérieures à d'autres techniques usuellement utilisées pour la fabrication de prothèses neuronales.

Les résultats des études présentées dans cette thèse suggèrent des intérêts au cœur de l'innovation scientifique et technologique. En ce qui concerne le processus d'activation in situ décrit dans cette thèse, il peut trouver des applications dans de nombreux processus d'analyses on peut citer; la détection de neurotransmetteurs comme la dopamine ou encore la catécholamine, quant aux analyses in-vitro, plusieurs applications sont possibles car les microélectrodes BDD sont connues pour leur bio-inertie. D'autres applications incluent l'activation in situ, cette méthode permet de quantifier la teneur totale en polyphénols au cours de la fermentation du vin ou encore le traitement des eaux usées. Les microélectrodes BDD en bande et ceux en réseau MEA peuvent être utilisés pour d'innombrables applications biomédicales telles que la détection de métaux lourds, de maladies neurochimiques ou encore pour des enregistrement électriques qui trouvent leur utilité dans l'étude de l'activité neuronale, aussi ces microélectrodes peuvent servir à l'administration de médicaments, à la fabrication de prothèses pour des implants rétiniens et cochléaires.

Enfin la fonctionnalisation de ces microélectrodes par des enzymes pourra permettre d'étendre le rayon de ces applications en tant que capteur de glucose, d'alcool ou d'ADN.

CHAPTER I

Introduction



Introduction

Diamond is an allotrope of carbon where the carbon atoms are arranged in a strong tetrahedral structure. The three dimensional assembly of different sp^3 hybridized carbon atoms, where the bonds are along the four directions connecting the center of a regular tetrahedron to its four corners, makes diamond the hardest natural material known. Naturally occurring diamond possesses excellent properties such as high thermal conductivity, optical transparency, electrical insulation, chemical corrosiveness, and biocompatibility.¹ Intrinsic diamond is a wide band gap material with $E_g = 5.45$ eV.² Table 1.1 compares the physical properties of silicon, a classical semiconductor, with those of diamond, a wide band gap semiconductor. Diamond's excellent properties make it an ideal candidate for electronic devices.

Table 1.1 Comparison of silicon and diamond physical characteristics²

Property	Si	Diamond
Band gap (eV)	1.12	5.45
Dielectric constant	11.9	5.5
Electric breakdown field (kV.cm ⁻¹)	300	10000
Electron mobility (cm ² .V ⁻¹ .s ⁻¹)	1500	2200
Hole mobility (cm ² .V ⁻¹ .s ⁻¹)	600	850
Thermal conductivity (W.cm ⁻¹ .K ⁻¹)	1.5	22

1.1 Synthesis of diamond

Diamond can be synthesized using two techniques: High-pressure/high-temperature (HPHT) and chemical vapor deposition (CVD). Large single crystal diamonds can be grown by HPHT techniques whereas CVD techniques produce mainly polycrystalline diamond.³ The description of these two growth techniques are described in sections 1.1.1 and 1.1.2.

1.1.1 HPHT synthesis of diamond

In nature, diamonds are formed at high temperature and high pressure deep in the Earth mantle. The high-pressure high-temperature (HPHT) process essentially simulates nature's process for synthesizing diamonds. The HPHT method uses a molten metal catalyst (usually nickel, cobalt or iron) to facilitate the change from graphite to diamond. A reproducible diamond synthesis technique was first demonstrated in 1955 at the General Electric Company.⁴ In their process, diamond was synthesized using a high pressure of 75000 atm, operating temperatures from 1200 to 2000 °C and heating pulses, generated by discharging a

Introduction

large electrolytic capacitor through the graphite sample (in order to avoid the melting or chemical reaction of the surrounding wall material). Although non-metallic catalysts like oxides, hydroxides and halides can also be used to synthesize diamond, however, such process requires higher pressure-temperature budgets, thus longer reaction times are required. The HPHT method is currently the most commonly used technique to fabricate industrial diamond (polishing, cutting tools, etc.). They are also used to change or enhance the colors of some rare natural diamonds by this technique, thus making them more valuable in the market.

1.1.2 CVD synthesis of diamond

The logic behind CVD processes lies in the thermal decomposition of carbon containing gases on natural diamond crystals heated between 600 and 1600 °C.⁴ At higher temperature excessive black carbon is deposited and at lower temperature insufficient growth takes place and hence the temperature range should be 900 – 1100 °C. Essentially, the gas phase species are energetically activated by either hot filament (HFCVD) or microwave plasma (MPECVD).⁵ Eversole was the first to demonstrate CVD diamond growth at low pressure.⁶ Matsumoto et al. made a significant breakthrough by demonstrating that atomic hydrogen etches sp^2 graphitic phases.⁷ In addition to the aforementioned activation techniques, DC-plasma, RF-plasma, electron cyclotron resonance-microwave plasma CVD (ECR-MPCVD), and their modifications were developed.^{6,8}

The critical step in CVD diamond growth is the nucleation phase. Diamond single crystals were used as the substrate to grow diamond during the early development of CVD diamond deposition. Later diamond deposition based on diamond seeds and hetero-substrates were developed. Mitsuda et al. found that scratching of the substrate surface with diamond powder could greatly enhance the nucleation density.⁹ Yugo et al. reported on generation of the diamond nuclei from ion bombardment in an electric field in plasma chemical vapor deposition.¹⁰ Methane (CH_4) is the commonly used precursor which is blended with a large quantity of hydrogen (H_2). Many active species (CH_4^+ , CH_3^+ , CH_2^+ , CH^+ , C^+ , H^+ , H_2^+ , CH_5^+ and H_3^+) are produced and they react with the surface of the diamond crystals.¹¹ Both amorphous and diamond allotropic forms of carbon are grown together during deposition. The monoatomic hydrogen species play an important role in etching the amorphous phase. Based on the grain size, the polycrystalline diamond films can be classified as microcrystalline (μCD - $> 1 \mu m$), nanocrystalline (NCD – few 100 nm) and ultra-nanocrystalline (UNCD - < 100 nm) diamond.^{6,12,13}

1.2 Synthesis of doped diamond

Although diamond is one of the best natural insulators, when doped, the material possess metallic behavior, thereby making it an excellent material for electrochemical, electronic and optoelectronic devices. Doping of diamond is achieved by introducing dopant atoms into the plasma during growth. The growth of boron doped diamond (BDD) films by CVD techniques has been achieved using a boron source added to the gaseous mixture resulting in p-type diamond films.¹⁴ N-type doping of diamond has been achieved by several techniques (nitrogen atom incorporation,¹² diphosphorous pentoside¹⁵ lithium ion implantation,¹⁶ etc.) which are more complicated as opposed to p-type doping. Koizumi et al. has reported on n-type semiconducting monocrystalline diamond using phosphine as the dopant source.¹⁶

1.3 MPECVD growth at the Diamond Sensors Laboratory

The Diamond sensors Laboratory (LCD) of CEA-LIST houses several dedicated MPECVD reactors enabling the growth of intrinsic and doped diamond layers (on substrates up to 4” in diameter) as well as heteroepitaxial growth. Two reactors were particularly used to grow the BDD films used during this PhD thesis:

- 1) Baobab: A home-made, cylindrical-shaped metal reactor exhibiting a plasma configuration close to that of the ASTeX PDS type reactors.
- 2) Seki: ASTeX AX6500 series reactor

Although several substrates such as quartz and highly resistive silicon wafers were used to grow BDD films, p-type silicon wafers (Siltronix) were employed for most of our experiments. They are monocrystalline, polished, ‘100’ oriented and heavily boron-doped (resistivity below 0.05 ohm.cm) silicon wafers with a thickness of 500 microns. The silicon substrates were sonicated in isopropanol and were then rinsed thoroughly with ultra-pure deionized water (18 Mohm) and dried under an argon stream. Diamond nucleation was initiated by diamond particles deposited on the surface of the substrate using nano-seeding. Aqueous, colloid-containing, diamond nanoparticles (DNP) purchased from Van Moppes were spread by spin coating to achieve a high density nanodiamond seeding using a method developed previously in the lab (refer to chapter 3 section 3.1.1).¹⁷

Figure 1.1 shows the schematics of the MPECVD reactor. It comprises four main elements: the microwave generator, the system for regulating the pressure, the gas supply system, and

Introduction

the vacuum chamber. A high frequency electromagnetic field pattern is created by the microwaves and the reactant gases (CH_4 , H_2 and trimethyl borane - TMB) are heated and excited to form a plasma ball. The substrate sits just below the visible edge of the plasma ball, on top of a molybdenum substrate holder. The reactors were also equipped with pyrometers to monitor the temperature during growth.

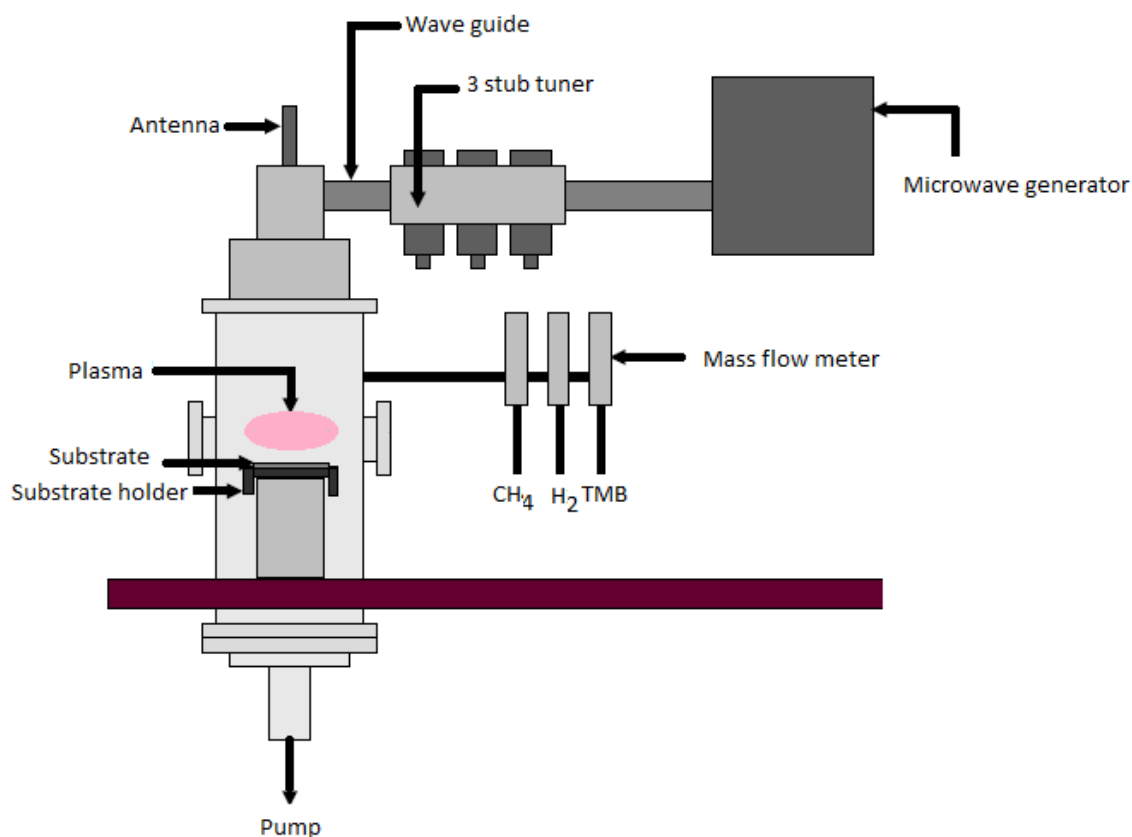


Figure 1.1 Schematics of an MPECVD reactor

During growth, the boron atoms substitute the carbon atoms when the concentration is low, and at higher concentration they occupy neutrally interstitial positions. In low doping cases, the substituted boron atoms are bonded to neighboring carbon atoms in the sp^3 configuration and in the ground state the holes provided by boron atoms are bound to one of the three-fold degenerate impurity states with a binding energy of 0.38 eV.¹⁸ At higher boron concentrations, as the average distance between boron atoms is close to the acceptor Bohr radius, metallic conduction appears at room temperature with conductivities of a few $100 \text{ ohm}^{-1} \cdot \text{cm}^{-1}$. The growth conditions are summarized in table 1.2. All growths were performed

Introduction

using a low methane to hydrogen ratio ($[\text{CH}_4]/[\text{H}_2] = 0.22\%$). TMB mixed with hydrogen at 2000 ppm is used as the boron gas source. These parameters were chosen based on the previous studies conducted in the group.¹⁹ A recent study was conducted to clarify whether diborane or TMB would be more appropriate for diamond growth. It appears that even in single crystal diamond, TMB appears as efficient as diborane for boron doping.²⁰

Table 1.2 Boron doped nanocrystalline layers synthesis conditions

Power	1.5 kW
Pressure	40 mbars
H ₂	88 sccm
CH ₄	0.22 sccm
TMB	12 (2000 ppm) sccm
Duration	10 - 15 hours
Temperature	750 °C

1.4 BDD film characterization

The synthesized BDD films were characterized using ellipsometry, Raman spectroscopy, X-ray photoelectron spectroscopy (XPS), scanning electron microscopy (SEM), secondary ion mass spectroscopy (SIMS) cyclic voltammetry (CV) and electrochemical impedance spectroscopy (EIS). These characterization techniques helped us to evaluate the continuity of the film and the boron incorporation.¹⁹ Studies on synthesis of highly doped diamond electrodes were already conducted in our lab based on different boron concentration. Subsection 1.4.1 and 1.4.2 recalls the structural, morphological and electrochemical characterization of the synthesized electrodes.^{19,21}

1.4.1 Structural and morphological characterization

The thickness was characterized using a UV–Vis Spectroscopic Ellipsometer (Horiba Jobin-Yvon, UVISSEL) and the films were almost uniformly thick throughout the wafer and were around 500 nm thick for a growth time of 15 hours. Secondary ion mass spectrometry (SIMS) depth profiling was performed at CNRS GEMaC (Meudon) using a Cameca IMS 4f ion microprobe. The measured boron concentration was approximately ($2 \times 10^{21} \text{ at.cm}^{-3}$). The Raman spectra were obtained using a Horiba Jobin–Yvon® SAS confocal Raman HR800.

Introduction

They were recorded on a cooled CCD detector after excitation of the films with the 325 nm line of a He–Cd laser (spot size $< 1 \mu\text{m}^2$).

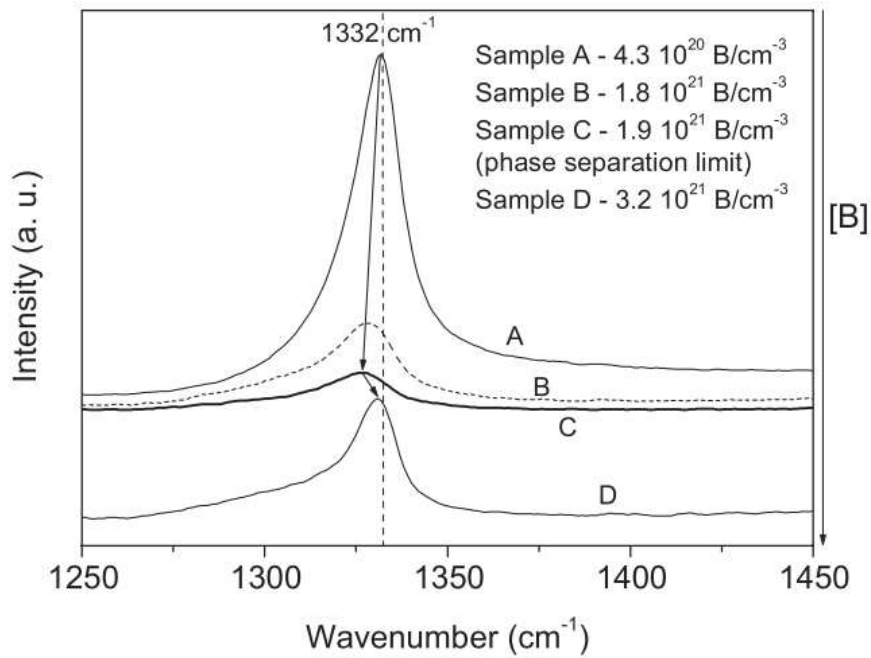


Figure 1.2 Raman spectra of different BDD films at different boron concentrations.¹⁹

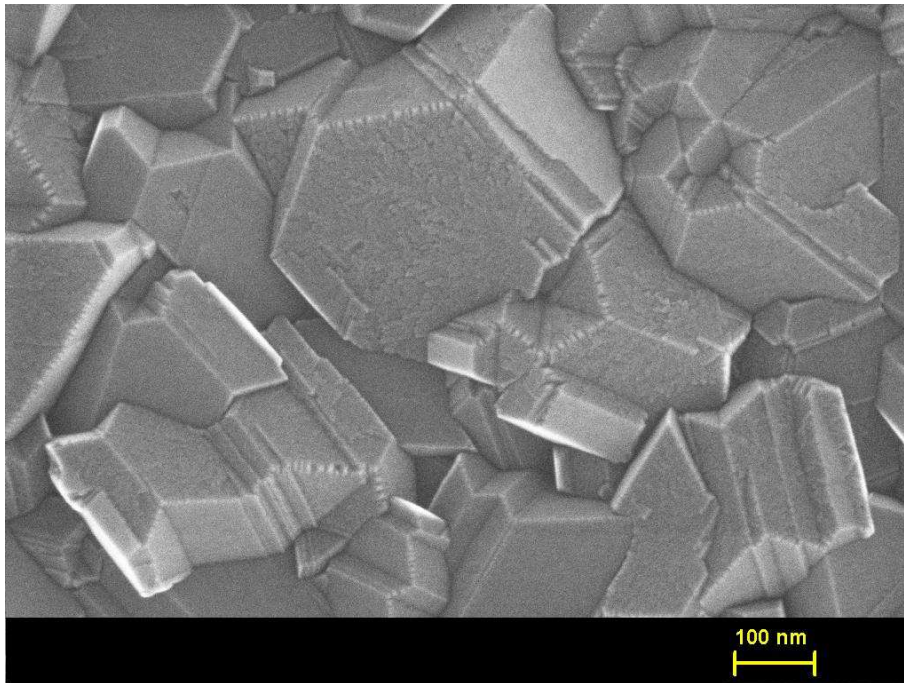


Figure 1.3 Scanning electron microscopic image of BDD film.

The UV excitation was chosen because the Raman shift of the diamond 1332 cm^{-1} signal appears more clearly with this excitation due to a lower Fano deformation. Figure 1.2 shows a

Introduction

diamond peak position slightly below, but very close to 1332 cm^{-1} , typical of boron concentrations up to the metallic limit ($3 \times 10^{20}\text{ at.cm}^{-3}$). The morphology and grain size were assessed using SEM. The typical morphology of a boron-doped nanocrystalline layer (BNCD) is shown in figure 1.3. The diamond crystals are highly faceted, with an average grain size of 100 nm and the obtained diamond films are uniform and continuous.

The surface analysis was performed using X-ray photoelectron spectroscopy. XPS analysis was carried out on samples directly after the growth. The spectrometer consists of a hemispherical analyzer and an Al $K\alpha$ anode supplied with a monochromator. Binding energies were referenced to the Au $4f_{7/2}$ peak located at 84 eV.²² According to the experimental geometry, the probed depth was estimated to be 1 nm. A curve-fitting procedure was carried out to extract the components in the C1s spectra using Voigt functions with a Lorentzian half-width of 0.2 eV. The Gaussian width was considered as an adjustable parameter. Then the area of each peak was calculated and the ratio of this area was recorded with respect to the total area.

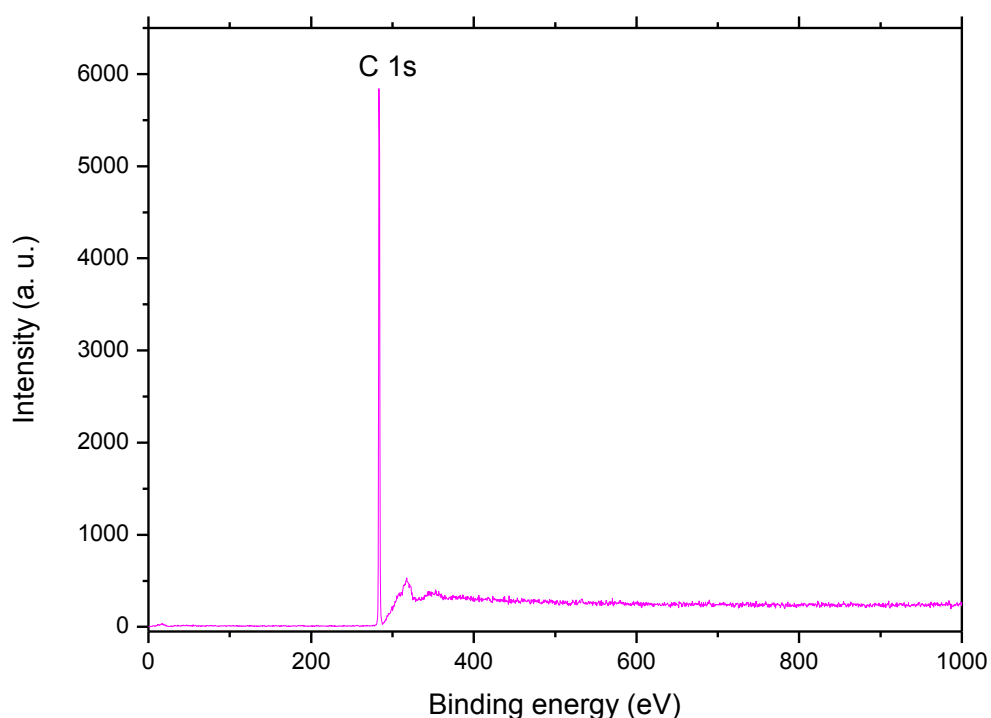


Figure 1.4 XPS Survey of BNCD thin film.

Introduction

Figure 1.4 shows the XPS wide spectra of an ‘as grown’ sample. No oxygen was detected using XPS corresponding to values below the detection threshold of 0.5 at %. In addition to the C-C sp³ / C-H major peak located at 283.9 eV, the C1s signal exhibits a shoulder at + 0.6 eV corresponding to CH_x (x>1) bonds which represents 19% of the C1s total area (Table 1.3).

Table 1.3 Percentages of total C1s area of the XPS components for ‘as grown’ BDD film

	C-C sp ²	C-C sp ³ / C-H	CH _x	C-OH	C-O-C
‘As grown’ BDD	< 0.5 %	81 %	19 %	-	-

1.4.2 Electrochemical characterization

An ideal electrode for bio-analysis need to possess wide working potential window to detect species over a wide potential range, high signal-to-background ratio (low background current) to have enhanced signal and sensitivity, low adsorption properties to reduce electrode fouling, high electrochemical reactivity and high microstructural and morphological stability to guaranty corrosion resistance. On the other hand, for neural recording and prosthesis high impedance, low noise and corrosion resistive electrode is desirable. Refer to section 1.5 for more details.

Two techniques: CV and EIS, were used to characterize the electrochemical (EC) properties of the electrode. The BDD electrode was fixed on a non-reactive one-compartment cell with a working surface area of typically 0.33 cm² and gallium-indium eutectic alloy was used between the silicon substrate and the copper plate for the electrical contact as shown in figure 1.5.

When an electrode is in contact with an electrolyte, a double layer is formed at the electrode/electrolyte interface as electric charges are accumulated on the electrode surfaces and ions of opposite charge are arranged in the electrolyte side (figure 1.6). The electric double layers formed at the electrode/electrolyte interfaces are accessible to ions present in the electrolyte.^{23,24} The interactions between the ions in solution and the electrode surface are assumed to be electrostatic in nature and result from the fact that the electrode holds a charge density which arises from either an excess or deficiency of electrons at the electrode surface. In order for the interface to remain neutral the charge held on the electrode is balanced by the redistribution of ions close to the electrode surface. The Stern layer is defined as the compact

Introduction

layer of immobile ions strongly adsorbed to the electrode surface.²⁵ Beyond the Stern layer is the so-called diffuse layer where ions are mobile under the coupled influence of electrostatic forces and diffusion. The result is analogous to an electrical capacitor which has two plates of charge separated by some distance.²⁶

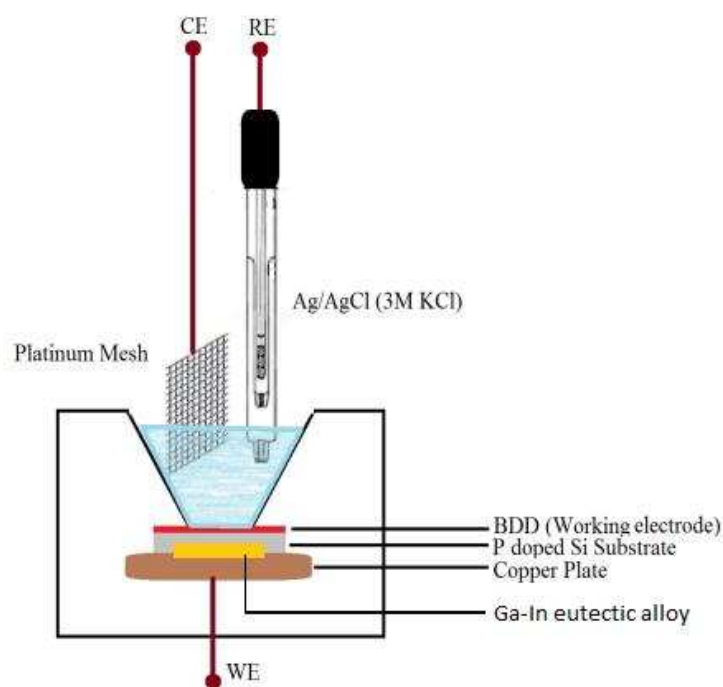


Figure 1.5 Schematic diagram of 3 electrodes setup: WE (Working Electrode), RE (Reference Electrode) and CE (Counter Electrode).

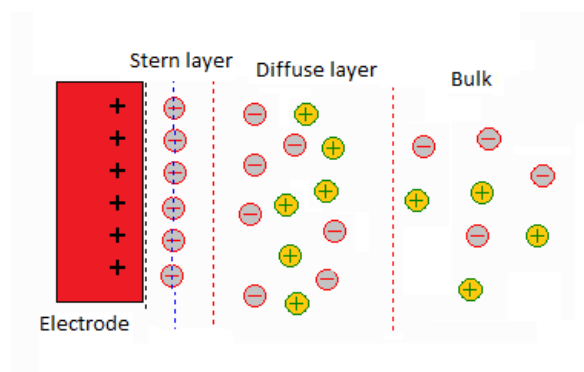


Figure 1.6 Schematics of electrical double layer at electrode/electrolyte interface.

The electrochemical window (potential range over which the electrolyte is not reduced or oxidized at an electrode) in which electrode charging is capacitive is the double layer region

Introduction

and is determined by cyclic voltammetry.²⁷ CV measurements consist of imposing an electric potential at the electrodes which varies periodically and linearly with time. The resulting electric current is recorded. The total charge accumulated at the electrode surface can be found by integrating the electric current with respect to time.²⁸

The EC characterizations were carried out using a 3 electrode setup. Ultrapure deionised (DI) water (Millipore Direct Q3) was used to prepare all the solutions. During cyclic voltammetry an Ag/AgCl/3M KCl reference electrode and a platinum mesh counter electrode were used while BDD was the working electrode. Figure 1.7 shows a typical voltammogram of the BDD electrode with a potential window greater than 3 V (in accordance with the literature values²⁹) in 0.5 M LiClO₄ aqueous solution. As the potential window corresponds to the potential range between which water gets electrolyzed, many electro-active species with high oxido-reduction potential can be detected. The double layer capacitance (C_D) probed for this electrode is 6.25 $\mu\text{F}\cdot\text{cm}^{-2}$. Lower the value, lower the signal-to-background ratio. The double layer capacitance is up to one order of magnitude lower than that of glassy carbon electrode.²⁹

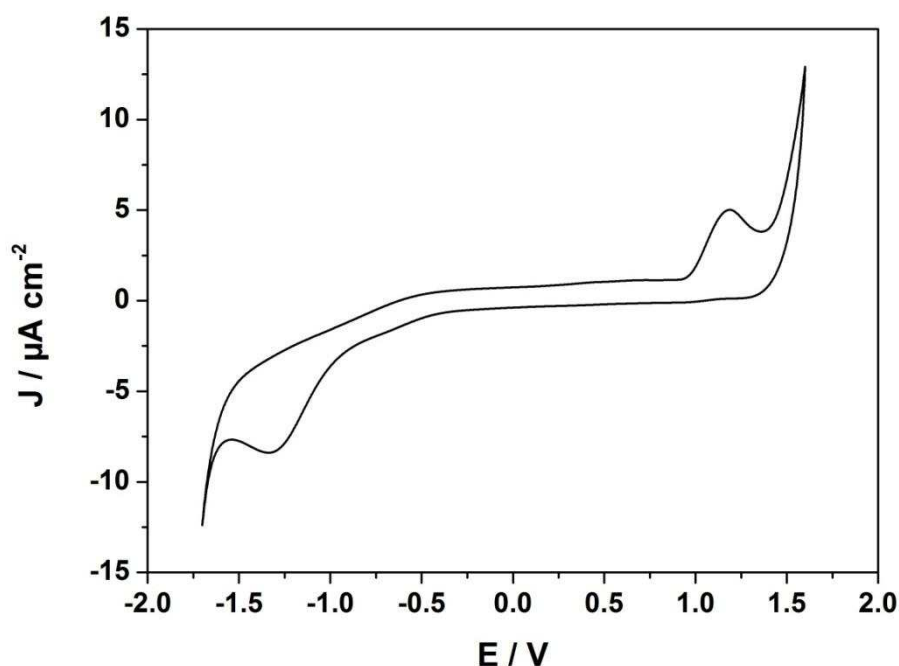


Figure 1.7 Cyclic voltammogram of ‘as grown’ electrode in 0.5 M aqueous LiClO₄ solution scanned at 0.1 V s⁻¹.

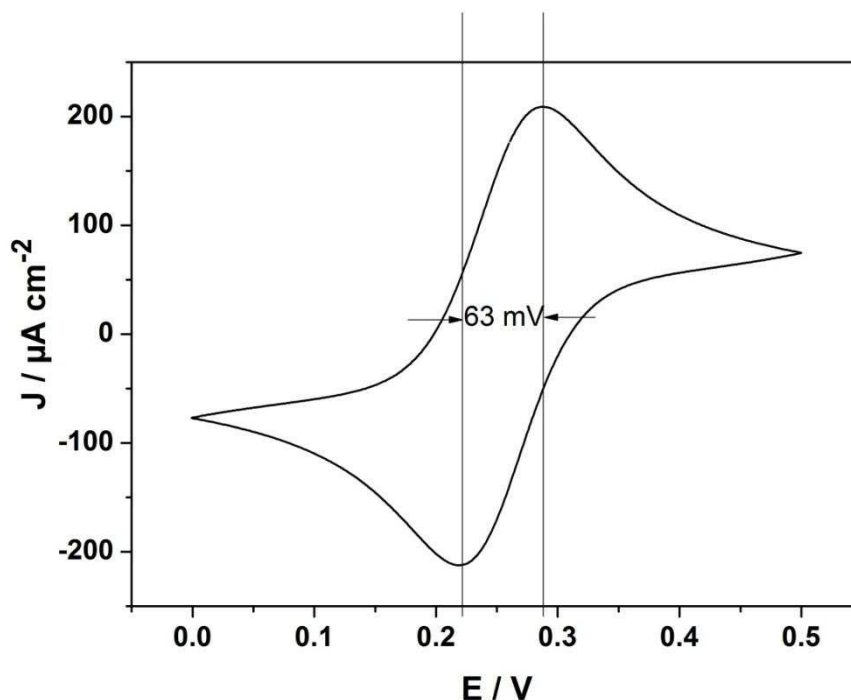


Figure 1.8 Cyclic voltammogram of an ‘as grown’ BDD electrode in ferri/ferrocyanide scanned at 0.1 V s^{-1} .

Equimolar (1 mM) solutions of potassium ferricyanide(III)/ potassium hexacyanoferrate(II).trihydrate (Acros Organics) were prepared in 0.5 M potassium chloride (Acros Organics) solution. The CV of BDD in ferri/ferrocyanide redox couple yields faradaic peaks and the peak separation $\Delta E_p (= E_{pc} - E_{pa})$ should be $58/n \text{ mV}$ at all scan rates at 25°C . Figure 1.8 shows one such CV and the calculate ΔE_p is 63 mV. Well defined peaks and peak separation close to theoretical value indicate higher electrochemical reactivity.³⁰ A high ΔE_p shows higher charge transfer resistance (resistance to the charge transferring chemical reaction at the electrode-electrolyte interface).³¹ High electrode reactivity is essential for electro-analytical application as it increases the sensitivity, signal-to-background ratio and reproducibility of the measurement.

Impedance spectroscopy is a powerful tool to analyze the impedance response of an electrochemical system and is sensitive to surface phenomena.³² An electrochemical system can be represented by an equivalent circuit of lumped resistors and capacitors. A frequently used circuit, called the Randles circuit, is shown in figure 1.9 a, is used to analyze the impedance spectra, where R_s is the solution resistance, R_T the charge transfer resistance, C_D the double layer capacitance and W the Warburg diffusion impedance.

Introduction

During an impedance measurement, a frequency response analyzer (FRA) is used to impose an AC signal of low amplitude on top of a DC potential. The frequency is varied from as high as 10^5 Hz to as low as about 10^{-3} Hz in a set number of steps per decade of frequency. Dividing the input voltage by the output current furnishes the impedance. The variation in impedance (magnitude and phase angle) is used for the interpretation. The AC voltage and current response of the cell is analyzed by the FRA to determine the resistive, capacitive and inductive behavior of the cell at different frequencies.

In the equivalent circuit, the faradaic component arises from the electron transfer via an EC reaction across the interface by overcoming an appropriate activation barrier (R_T) along with resistance represented by conductive pathways for ion (R_S). The nonfaradaic current results from charging the double-layer capacitor associated with space-charge polarization regions (C_D). The mass transport of the reactants and the products provides another class of impedance: Warburg component (W).

EIS data for electrochemical cells such as fuel cells are most often represented by Nyquist plot (figure 1.9 b). A complex plane or Nyquist plot depicts the imaginary impedance, which is indicative of the capacitive character of the cell, versus the real impedance of the cell. The semicircle relates to charge-transfer controlled process and its intercept with the X axis gives R_S and R_T values (as seen in figure 1.9 b).

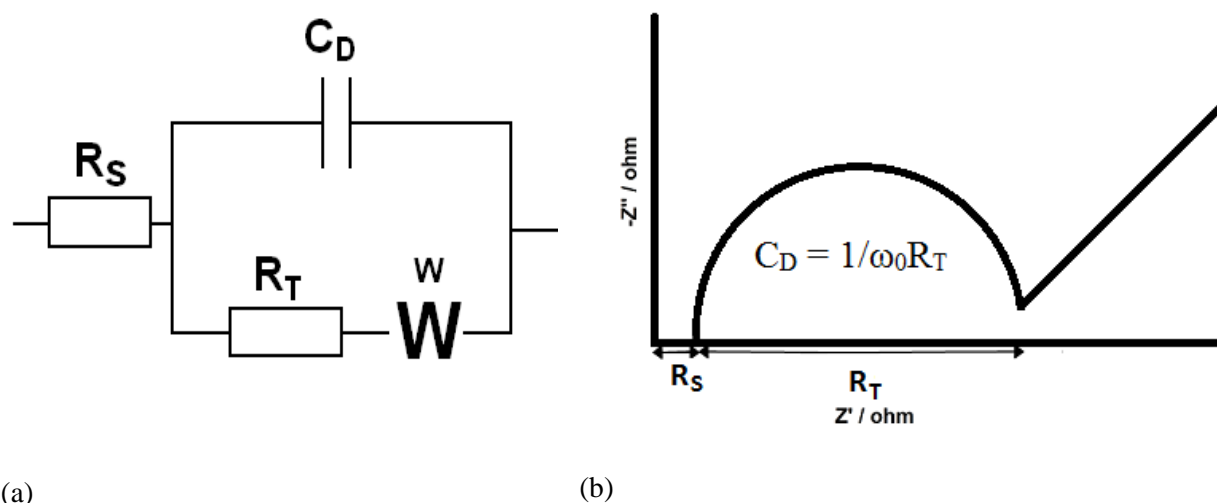


Figure 1.9 (a) Randles equivalent circuit and (b) Nyquist Plot which describes impedance behavior of a simple electrochemical cell

The electron transfer rate constant k_0 (k_0 is measured in 1mM ferro/ferricyanide in 0.5 M KCl, throughout the report, unless stated) was experimentally determined by EIS over a frequency

Introduction

range of 50 kHz–1Hz with logarithmic point spacing and potential amplitude of 0.01 V rms while the BDD was maintained at open circuit potential. The EIS was done in a three electrode setup where BDD electrode is the working electrode, platinum wire the pseudo-reference electrode and platinum mesh the counter electrode. The electrodes were rinsed in DI water and dried under flow of argon gas prior to each experiment. The k_0 value was determined from the Nyquist plot fitted using ZSimWin 3.21 software. Unless stated otherwise the potential is always given versus an Ag/AgCl reference electrode.

The quality of an electrode can be related to its electron transfer rate k_0 which is defined by equation (1.1) and used to characterize our electrodes in the rest of the document:

$$k_0 = \left(\frac{RT}{nF} \right) \frac{1}{nSFR_T C_0} \quad (1.1)$$

Where R = Universal gas constant, T = Absolute temperature (K), S = Surface area of the electrode (cm^2), F = Faraday's constant (96500 C.mol^{-1}), R_T = Electron transfer resistance of electrode (ohm), C_0 = Concentration of redox couple (mol.cm^{-3}), n = number of electrons transferred. The higher the value of k_0 , the better the reactivity of the electrode. The experimental and fitted Nyquist plot of the electrode is depicted in figure 1.1 and k_0 calculated for this electrode was 0.5 cm.s^{-1} .

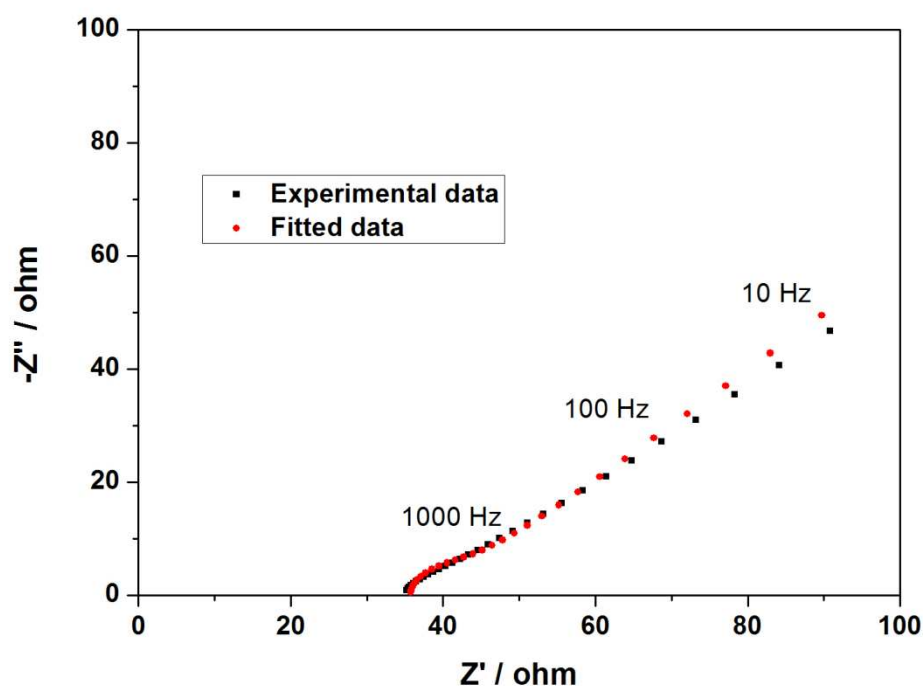


Figure 1.10 Experimental and fitted Nyquist plot of an 'as grown' BDD electrode.

1.5 BDD films for electrochemical sensors and biosensors

The synthesized BDD films exhibit excellent electrochemical characteristics. The objective of the thesis is to realize electrochemical sensors for biomedical applications. In biomedical and environmental applications, electrochemical sensors are generally well adapted due to their good sensitivity, fast measuring time, portability, low power consumption and cost effectiveness. BDD electrodes have been a major focus of research and development in electrochemical and biomedical sensors due to their electro-analytically advantageous features,^{5,29,33,34} namely: wide potential window in aqueous electrolytes (> 3 V), corrosion stability in aggressive media, morphological and structural stability at very high current, low background current and bio-inertness.

Owing to diamond's stability and high activity to oxidize organic compounds, electrochemical treatment of waste water provides an attractive alternative to traditional methods. Compared to other electrode materials such as glassy carbon, metal oxide electrodes, diamond has proven to be an excellent candidate because of its high anodic stability and wide electrochemical window.³⁵ Unlike conventional electrodes, diamond is less susceptible to fouling and does not release toxic ions. The organic compounds are oxidized to CO_2 by electrogenerated hydroxyl radical (OH^*). Organic pollutants oxidized on diamond electrodes include, carboxylic acids, nitrophenols, phenols, chlorophenols, cyanides, etc.²⁹

BDD electrodes are suitable mercury-free electrochemical sensors to detect trace metals such as lead using anodic stripping voltammetry.³⁶ Several techniques of anodic stripping voltammetry have been successfully employed for lead detection which involves toxic mercury film or mercury drop electrodes. BDD electrodes are ideal due to their enlarged potential window, low background current and long term stability. Simultaneous quantification of other heavy metals such as zinc, cadmium and copper is also possible using BDD electrodes.³⁷

Amperometric biosensors based on BDD electrodes have also attracted the interest of many researchers as they combine the merits of biosensors such as specificity, sensitivity, and fast response with the superior properties of BDD electrodes. Carbon-based materials such as glassy carbon, porous carbon, carbon nanotubes and carbon nanofibers, etc. possess advantages such as simple preparation technique, large potential ranges and ease of surface modification. However, fouling of the electrode has to be dealt with and this leads to frequent polishing or disposal of electrodes after limited usage. BDD electrodes are less subjected to

Introduction

fouling than other carbon-based electrodes.³⁸ Other advantages include the low background current increases the sensitivity when compared to the other electrodes.³⁹ Development of new chemical approaches to attach biomolecules covalently to diamond surfaces has led to an entirely new class of electrochemical biosensors. The control of surface termination is crucial for the detection of charged biomolecules. H-terminated BDD electrodes were used to detect biomolecules such as glucose, DNA, NADH, etc.^{38,40,41} O-terminated BDD electrodes were employed for detection of dopamine,⁴² tyrosinase modified boron doped diamond electrode to detect Cresol,⁴³ etc. A detailed example of biosensor developed using BDD electrodes to detect uric acid in urine is explained in chapter 4.

Another interesting feature worth noting is the biocompatibility of diamond films. Biocompatibility, by definition, is the quality of not producing toxic or injurious effects on biological systems. Factors such as the chemical composition, roughness, surface energy, topography and hydrophobicity of a material determine the interaction of cells and biomolecules with the electrode.⁴⁴ Specht et al. has demonstrated the biocompatibility of diamond surfaces by selective attachment of mammalian neurons and ordered outgrowth of neurites on its surfaces.⁴⁵ As diamond is extremely inert, unlike metal implants, it does not lead to cytotoxicity, allergy or malign effects caused by its degradation. Evaluation of osteoblast and endothelial cell adhesion on diamond surfaces highlights not only the mechanical and physical properties but also its attraction to cell colonization.⁴⁶ Grausova et al. has evaluated this possibility and recommends nanocrystalline diamond (NCD) as an excellent candidate for in-vivo experiments and tissue engineering.⁴⁶ Surface roughness of biomaterials plays an important role in biocompatibility, especially on the adhesion of endothelial cells. On the other hand, osteoblast cells are sensitive to the chemical composition of the surface. Mitura et al. investigated on the impact of the contact of the NCD coating with blood.⁴⁷ NCD coating does not change in any significant way the activation of the elements of coagulation of blood.

Biocompatibility, chemical stability, biostability and excellent mechanical characterization indicate diamond's potential for in-vivo and in-vitro biosensing applications. Some examples of electrophysiological applications of diamond such as in-vitro neural recording and retinal implants are described in detail in chapter 5.

Despite these promising properties when compared to classical electrodes, diamond electrodes are also susceptible to fouling when used in organic or biological fluids.^{35,48,49} An in-situ

regeneration approach was developed as part of this thesis in order to solve the problems associated with fouling and is described in detail in Chapter 2.

Chapter 3 deals with the fabrication processes for microelectrodes, these being better suited for biomedical applications when compared to macroelectrodes. Microelectrodes exhibit significant advantages over macro-electrode systems, such as a decreased ohmic drop, a hemispherical diffusion layer, which extends into the solution, rapid establishment of a steady-state signal, and higher S/N ratio. Moreover, they require very small sample volumes

Several multi-electrode arrays systems have been reported elsewhere, where all microelectrodes are connected together to form one single probe^{51,52}. Those electrodes, when designed appropriately, still behave as individual microelectrodes at suitable scan rates, but since they are all interconnected they offer the additional advantages of an enhanced electrical signal when compared to single electrodes. Boron doped diamond (BDD) materials exhibit superior electrochemical properties over other conventional electrode materials including low capacitive background currents, wide potential window in aqueous media and corrosion resistance in harsh environments^{29,33,53}. Thus the advantage of using microelectrodes over macro-electrodes has been further improved by combining their unique properties resulting from geometrical characteristics with the excellent electrochemical properties of BDD materials⁵⁴⁻⁵⁷.

1.6 Theory of microelectrodes

Ultramicroelectrodes (UMEs) are electrodes with a critical size dimension below 25 μm . UMEs exhibit different behavior from those of macroelectrodes when the critical diameter is equal to or less than the diffusion layer.⁵⁴ The diffusion of electro-active species occurs in two dimensions: radially with respect to the axis of symmetry and normal to the plane of the electrode. The current density is not uniform across the face of the disk, but is greater at the edge, which offers the nearest point of arrival to electro-reactant drawn from a large surrounding volume.

The faradaic current that flows at any time is a direct measure of the rate of the electrochemical reaction taking place at the electrode³². This current depends upon two phenomena:

Introduction

- 1) Charge transfer kinetics
- 2) Mass transport rate

Charge transfer kinetics is defined as the rate at which electrons are transferred across the interface and the rate at which species move from the bulk of the solution to the electrode is known as mass transport rate. There are three modes of mass transfer:

- a. Diffusion: defined as the movement of any species under the influence of chemical potential or a concentration gradient.
- b. Migration: the movement of charged particles in an electric field.
- c. Convection: movement of material contained within a volume element of stirred (hydrodynamic) solution. It can be both natural and forced convection.

The experiments were designed such that the mass transport rate is only limited to the contribution from diffusion. Fick's first law quantifies the movement of a species (under diffusion control) with respect to the distance x from an electrode with the flux J_0 . The relation is given by:

$$J_0 = D_0 \left(\frac{\partial C_0}{\partial x} \right) \quad (1.2)$$

Where D_0 is the diffusion coefficient, C_0 the concentration, and x the distance. In the above equation (equation 1.2), the units of flux J_0 are in $\text{moles.cm}^{-2}.\text{s}^{-1}$. The faradaic current can be obtained by simplifying the above equation and is given as:

$$i = nFAD_0 \left(\frac{\partial C_0}{\partial x} \right) |_{x=0} \quad (1.3)$$

where n is the number of electrons transferred per molecule of reactant, F is Faraday's constant, and A is the surface area of the electrode. Fick's second law describes the time-dependent changes in the concentration of the substance amount caused by the flux.

$$\frac{\partial C_0}{\partial t} = D_0 \left(\frac{\partial^2 C_0}{\partial x^2} \right) \quad (1.4)$$

where 't' is duration of experiment.

The diffusion layer is the region in the vicinity of an electrode where the concentrations are different from their value in the bulk solution. The flux of the substance toward the electrode is then described by the product of the diffusion coefficient of the substance, D_0 , and its bulk concentration divided by the diffusion layer thickness, d . This quantity is defined by the relationship:

Introduction

$$d = (2D_0t)^{0.5} \quad (1.5)$$

When $d \ll r$ (radius r of the electrode), the perturbation of the linear diffusion flux caused by the hemispherical diffusion at the electrode edges extends to a short distance of several d from the edge. The behavior of the electrode can be approximated by the infinite electrode model as only a small part of the electrode surface is affected. When $d \gg r$, the edge effect plays an important role as the diffusional flux towards the electrode is constant with time but inhomogeneous over the electrode surface. The diffusion layer is hemispherical in shape and extends out into the solution. Figure 1.11 demonstrates the planar and radial diffusion profile at a macro and micro electrode respectively. Under such conditions, the concentration of the electro-active substance attains the limiting value described by the equation for steady-state transport, which corresponds to the time derivative being zero in Fick's second law and the current goes to a steady state value.

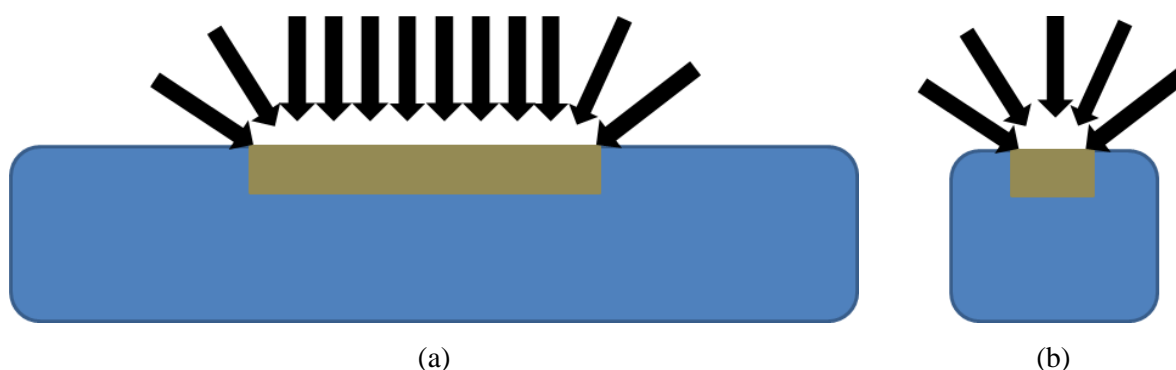


Figure 1.11 Schematics illustration of (a) linear diffusion at a planar electrode and (b) radial diffusion at a microelectrode.

The steady state limiting current is different for different types of ultramicroelectrodes based on their geometry:³²

(a) Spherical or hemispherical UME:

$$i_{lim} = 4\pi nrFD_0C_0 \quad (1.6)$$

(b) Cylindrical UME:

$$i_{lim} = 2nFAD_0C_0/r\ln\tau \quad (1.7)$$

$$\text{where } \tau = 4D_0t/r^2$$

(c) Band UME:

$$i_{lim} = 2\pi nFAD_0C_0/w\ln(64D_0t/w^2) \quad (1.8)$$

where w = width of the band

(d) Disk UME:

$$i_{lim} = 4nrFD_0C_0 \quad (1.9)$$

Conclusion

In the first chapter, different diamond growth techniques and characterization methods are described. The diamond electrodes were synthesized using MPECVD technique from a mixture of methane, hydrogen and TMB. The physical and chemical properties of the thin film were assessed using Raman spectroscopy, XPS, SEM, CV and EIS. Highly doped diamond electrodes give rise to extreme reactivity and they are ideal candidates for electro-analytical and biosensing applications. Chapter 2 addresses the problem associated with loss of reactivity especially when the electrode is used in a biological medium. A novel activation process is described in detail where diamond electrodes can be reactivated within the biological fluid.

Bibliography

- (1) Jee, A.; Lee, M. *Current Applied Physics* **2009**, 9, e144–e147.
- (2) Tolbert, L. M.; Ozpineci, B.; Islam, S. K.; Chinthavali, M. S. *From Proceeding (379) Power and Energy Systems* **2003**, 1–5.
- (3) Neves, A. J.; Nazaré, M. H. *Properties, Growth and Applications of Diamond*; IET, 2001; p. 427.
- (4) Ferro, S. *Journal of Materials Chemistry* **2002**, 12, 2843–2855.
- (5) Xu, J.; Granger, M. C.; Chen, Q.; Strojek, J. W.; Lister, T. E.; Swain, G. M. *Analytical Chemistry News & Features* **1997**, 591 A – 597 A.
- (6) Lee, S.; Lin, Z.; Jiang, X. *Material Science and Engineering* **1999**, 25, 123–154.
- (7) Matsumoto, S.; Sato, Y.; Tsutsumi, M.; Setaka, N. *Journal of Materials Science* **1982**, 17, 3106–3112.
- (8) Tang, Y.; Aslam, D. M. *Journal of Vacuum Science & Technology B: Microelectronics and Nanometer Structures* **2005**, 23, 1088.
- (9) Mitsuda, Y.; Kojima, Y.; Yoshida, T.; Akashi, K. *Journal of Materials Science* **1987**, 22, 1557–1562.
- (10) Yugo, S.; Kanai, T.; Kimura, T.; Muto, T. *Applied Physics Letters* **1991**, 58, 1036.
- (11) Tsuda, M.; Nakajima, M.; Oikawa, S. *Journal of American Chemical Society* **1986**, 108, 5780–5783.
- (12) May, P. W.; Smith, J. a.; Mankelevich, Y. a. *Diamond and Related Materials* **2006**, 15, 345–352.
- (13) Butler, J. E.; Sumant, A. V. *Chemical Vapor Deposition* **2008**, 14, 145–160.
- (14) Fujimori, N.; Imai, T.; Doi, A. *Vacuum* **1986**, 36, 99–102.
- (15) Okano, K.; Kiyota, H.; Iwasaki, T.; Nakamura, Y.; Akiba, Y.; Kurosu, T.; Iida, M.; Nakamura, T. *Applied Physics A Solids and Surfaces* **1990**, 51, 344–346.
- (16) Koizumi, S.; Kamo, M.; Sato, Y.; Mita, S.; Sawabe, A.; Reznik, A.; Uzan-Saguy, C.; Kalish, R. *Diamond and Related Materials* **1998**, 7, 540–544.
- (17) Scorsone, E.; Saada, S.; Arnault, J. C.; Bergonzo, P. *Journal of Applied Physics* **2009**, 106, 014908.

Introduction

- (18) Wu, D.; Wang, Z. L.; Luo, Q.; Gu, C. Z.; Wang, N. L.; Li, C. Y.; Lu, X. Y.; Jin, Z. S. *Physical Review B* **2006**, 73, 1–5.
- (19) Vanhove, E.; de Sanoit, J.; Mailley, P.; Pinault, M. -a.; Jomard, F.; Bergonzo, P. *Physica Status Solidi (a)* **2009**, 206, 2063–2069.
- (20) Volpe, P.-N.; Arnault, J.-C.; Tranchant, N.; Chicot, G.; Pernot, J.; Jomard, F.; Bergonzo, P. *Diamond and Related Materials* **2012**, 22, 136–141.
- (21) Vanhove, E.; de Sanoit, J.; Arnault, J. C.; Saada, S.; Mer, C.; Mailley, P.; Bergonzo, P.; Nesladek, M. *Physica Status Solidi (a)* **2007**, 204, 2931–2939.
- (22) Seah, M. P. *Surface and Interface Analysis* **1993**, 20, 243–266.
- (23) Yoon, S.; Lee, J.; Hyeon, T.; Oh, S. M. *Journal of The* **2000**, 147, 2507.
- (24) Wang, H.; Pilon, L. *Electrochimica Acta* **2012**, 64, 130–139.
- (25) Birdi, K. S. *Introduction to Electrical Interfacial Phenomena*; Taylor & Francis, 2009; p. 167.
- (26) Lvovich, V. F. *Impedance Spectroscopy: Applications to Electrochemical and Dielectric Phenomena* (Google eBook); John Wiley & Sons, 2012; p. 368.
- (27) *Green Industrial Applications of Ionic Liquids* (Google eBook); Springer, 2003; Vol. 0, p. 584.
- (28) Compton, R. G.; Banks, C. E. *Understanding Voltammetry*; World Scientific, 2011; p. 429.
- (29) Panizza, M.; Cerisola, G. *Electrochimica Acta* **2005**, 51, 191–199.
- (30) Wang, W. L.; Jin, E. M.; Gu, H.-B. *Transactions on Electrical and Electronic Materials* **2012**, 13, 121–124.
- (31) Nicholson, R. S. *Analytical chemistry* **1965**, 37, 1351–1355.
- (32) Bard, A. J.; Faulkner, L. R. *Electrochemical Methods: Fundamentals and Applications*; Wiley, 2001; Vol. 6.
- (33) Swain, G. M. *Analytical chemistry* **1993**, 65, 345–351.
- (34) Granger, M. C.; Witek, M.; Xu, J.; Wang, J.; Hupert, M.; Hanks, A.; Koppang, M. D.; Butler, J. E.; Lucazeau, G.; Mermoux, M.; Strojek, J. W.; Swain, G. M. *Anal. Chem.* **2000**, 72, 3793–3804.
- (35) Iniesta, J.; Michaud, P. A.; Panizza, M.; Cerisola, G.; Aldaz, A.; Comminellis, C. *Electrochimica Acta* **2001**, 46, 3573–3578.

Introduction

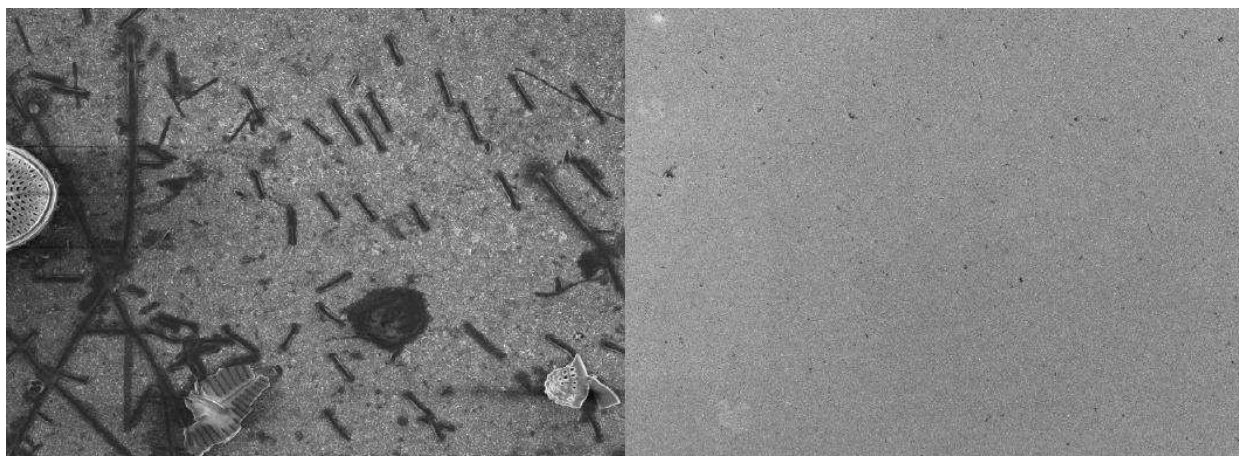
- (36) Dragoe, D.; Spătaru, N.; Kawasaki, R.; Manivannan, A.; Spătaru, T.; Tryk, D. a.; Fujishima, A. *Electrochimica Acta* **2006**, 51, 2437–2441.
- (37) El Tall, O.; Jaffrezic-Renault, N.; Sigaud, M.; Vittori, O. *Electroanalysis* **2007**, 19, 1152–1159.
- (38) Rao, T. N.; Yagi, I.; Miwa, T.; Tryk, D. a; Fujishima, a *Analytical chemistry* **1999**, 71, 2506–11.
- (39) Zhou, Y.; Zhi, J. *Talanta* **2009**, 79, 1189–96.
- (40) Lee, J.; Park, S.-M. *Analytica Chimica Acta* **2005**, 545, 27–32.
- (41) Weng, J.; Zhang, J.; Li, H.; Sun, L.; Lin, C.; Zhang, Q. *Analytical chemistry* **2008**, 80, 7075–83.
- (42) Tryk, D. A.; Tachibana, H.; Inoue, H.; Fujishima, A. *Diamond and Related Materials* **2007**, 16, 881–887.
- (43) Zhou, Y.; Zhi, J. *Electrochemistry Communications* **2006**, 8, 1811–1816.
- (44) Ponsonnet, L.; Reybier, K.; Jaffrezic, N.; Comte, V.; Lagneau, C.; Lissac, M.; Martelet, C. *Materials Science and Engineering: C* **2003**, 23, 551–560.
- (45) Specht, C. G.; Williams, O. a; Jackman, R. B.; Schoepfer, R. *Biomaterials* **2004**, 25, 4073–8.
- (46) Grausova, L.; Kromka, a.; Bacakova, L.; Potocky, S.; Vanecek, M.; Lisa, V. *Diamond and Related Materials* **2008**, 17, 1405–1409.
- (47) Mitura, S.; Mitura, A.; Niedzielski, P.; Couvrat, P. *Chaos, Solitons & Fractals* **1999**, 10, 2165–2176.
- (48) Montilla, F.; Michaud, P. A.; Morallon, E.; Vazquez, J. L.; Comninellis, C. *Electrochimica Acta* **2002**, 47, 3509–3513.
- (49) Panizza, M.; Michaud, P. a.; Cerisola, G.; Comninellis, C. *Journal of Electroanalytical Chemistry* **2001**, 507, 206–214.
- (50) Stulik, K.; Amatore, C.; Holub, K.; Marecek, V.; Kutner, W. *Pure and Applied Chemistry* **2000**, 72, 1483–1492.
- (51) Niwa, O.; Xu, Y.; Halsall, H. B.; Heineman, W. R. *Analytical chemistry* **1993**, 65, 1559–63.
- (52) Kounaves, S. P.; Deng, W.; Hallock, P. R. *October* **1994**, 66, 418–423.
- (53) Yano, T.; Tryk, D. A.; Hashimoto, K.; Fujishima, A. *Journal of The Electrochemical Society* **1998**, 145, 1870–1876.

Introduction

- (54) Soh, K. L.; Kang, W. P.; Davidson, J. L.; Basu, S.; Wong, Y. M.; Cliffel, D. E.; Bonds, A. B.; Swain, G. M. *Diamond and Related Materials* **2004**, 13, 2009–2015.
- (55) Lawrence, N. S.; Pagels, M.; Meredith, A.; Jones, T. G. J.; Hall, C. E.; Pickles, C. S. J.; Godfried, H. P.; Banks, C. E.; Compton, R. G.; Jiang, L. *Talanta* **2006**, 69, 829–834.
- (56) Tian, R.; Zhi, J. *Electrochemistry Communications* **2007**, 9, 1120–1126.
- (57) Pagels, M.; Hall, C. E.; Lawrence, N. S.; Meredith, A.; Jones, T. G. J.; Godfried, H. P.; Pickles, C. S. J.; Wilman, J.; Banks, C. E.; Compton, R. G.; Jiang, L. *Analytical chemistry* **2005**, 77, 3705–8.

CHAPTER II

Electrochemical activation of diamond electrodes



Introduction

Boron-doped diamond electrodes are extremely promising for a range of biomedical applications as they exhibit a unique combination of favorable properties. Despite these promising properties when compared to classical electrodes, unfortunately they too are susceptible to fouling when used in organic or biological fluids.¹⁻³ Electrode fouling can be due to adsorption or adhesion of biomolecules such as proteins, enzymes, cells, intermediate products of oxidation of organic compounds, etc.⁴⁻⁷ ‘As grown’ BDD electrodes are hydrogen-terminated and they exhibit very good electrochemical reactivity characterized by their high electron transfer rate k_0 . But ageing in air or in aqueous solution reduces the k_0 value to considerably,^{8,9} possibly due to surface modification. The H-terminated, ‘as grown’ BDD electrode is gradually modified to O-terminated on exposure to air. Both fouling and ageing affects the accuracy, sensitivity and reproducibility of the measurement and lifetime of the electrode.

One of the thesis’ objectives was to develop a simple and fast electrochemical (EC) treatment that can be used to retrieve the lost reactivity, thereby enhancing electrodes’ reusability over long periods of measurement without degradation of the signal. This chapter describes a novel EC activation process where a train of short current pulses is applied to the BDD electrodes. The surface modification of EC-activated electrodes is investigated using X-ray Photoelectron Spectroscopy and electrochemical characterization. Influence of current density, pH, and number of pulses on EC-activation is discussed. Some examples of activation within biological and synthetic fluids are also presented.

2.1 Ageing and fouling of the electrode

Two phenomena: electrode ageing and fouling, that affect the electrode reactivity and thereby affect the accuracy of measurement are explained in detail with the help of cyclic voltammetry (CV) and electrochemical impedance spectroscopy (EIS). The details of electrochemical characterization were explained in chapter 1 (section 1.4.2).

2.1.1 Electrode ageing

BDD Electrodes, when fabricated from recently grown material, exhibit very high reactivity with k_0 values above 0.01 cm.s^{-1} . The peak to peak separation of the oxidation and reduction potential (ΔE_p in $[\text{Fe}(\text{CN})_6]^{3-/4-}$ solution) of such an electrode was probed at 60 mV at a 100

$\text{mV}\cdot\text{s}^{-1}$ scan rate (as shown in figure 2.1), a value close to the theoretical value for this couple, thus demonstrating the extreme reactivity of the diamond surface. The k_0 value for this electrode was estimated to be $5.9 \times 10^{-2} \text{ cm}\cdot\text{s}^{-1}$. However, when exposed to air for 30 days (under laboratory conditions), the same electrode evidenced a decrease in the k_0 value of 1100 % and ΔE_p decreased by 42% due to this ageing. Figure 2.2 shows a comparison between the Nyquist plots of ‘as grown’ BDD electrode and the same electrode after ageing where the transfer resistance R_T (related to the diameter of the high frequency arc) increased from 10 ohm to 105 ohm.

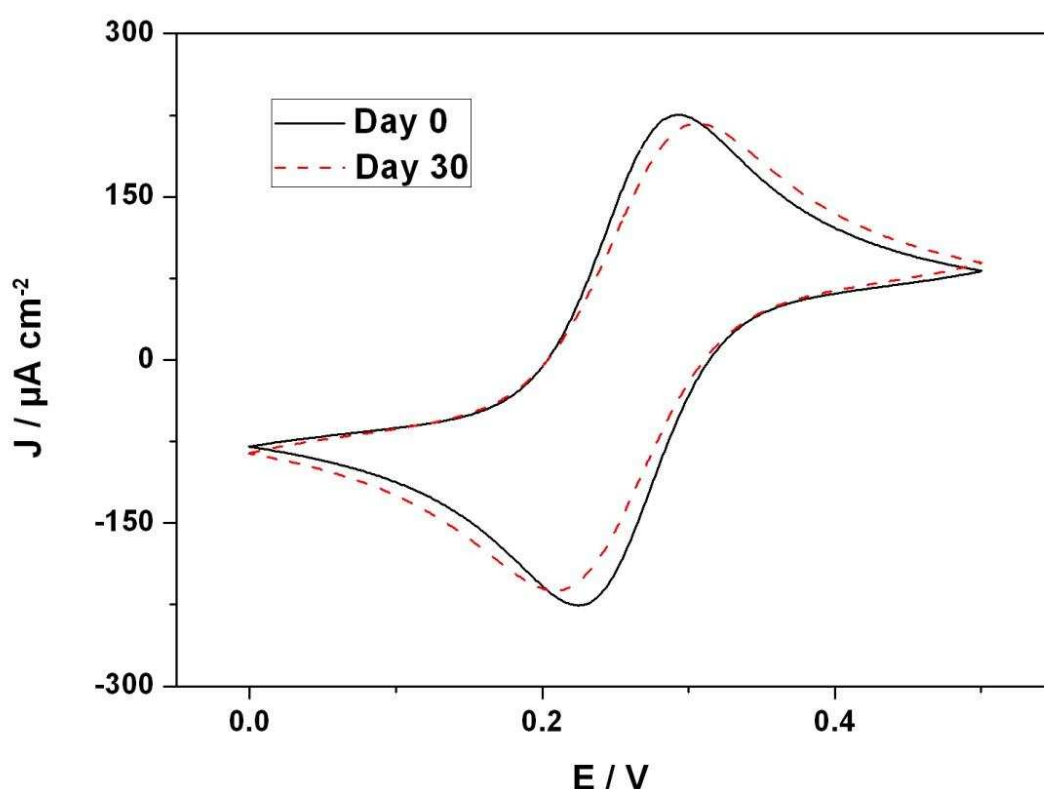


Figure 2.1 Cyclic voltammogram of ‘as grown’ electrode (solid line) and the same electrode after 30 days exposure to air (dashed line) scanned at 100 mV s^{-1} in 0.5 M KCl solution containing $1 \text{ mM } [\text{Fe}(\text{CN})_6]^{3-/4-}$.

There have been several proposals suggested by various groups in order to establish a relationship between the ageing and the electrochemical properties of BDD electrodes. Duo et al. proposed that a non-negligible amount of sp^2 species might be present in the grain boundary which could be the reason for the high reactivity of ‘as grown’ electrode.¹⁰ A relatively mild anodic polarization process was sufficient to transform the surface from

hydrophobic to hydrophilic without changes in the crystal shape and size. The variation of BDD electrode surface is related to the oxidation of the sp^2 states present on the surface leading to a “non-active” polycrystalline diamond surface. Another study of this matter indicated that the changes in the BDD electrodes during the anodic process are related to the variation in the concentration of H at the surface.¹⁰ An Oxygen-terminated surface may be the cause of the observed high surface electrical resistance, indicating the attainment of positive electron affinity.¹¹

A study has been conducted in our laboratory to address the evolution of H-terminated BDD electrochemical properties with time.⁸ It was observed that these electrochemical evolutions were due to modification of surface termination and partial inactivation. According to this study, the XPS analysis of ‘as grown’ BDD electrode shows C-C sp^3 and C-H (74% of total area) and C-H_x (26%) peaks. After exposure to air, an increase in CH_x bonds and a weak contribution of C-OH bond was observed. Hence the electrochemical evolution of ‘as grown’ BDD electrode might be due to an increase in polyhydride carbon species and surface oxygenation.

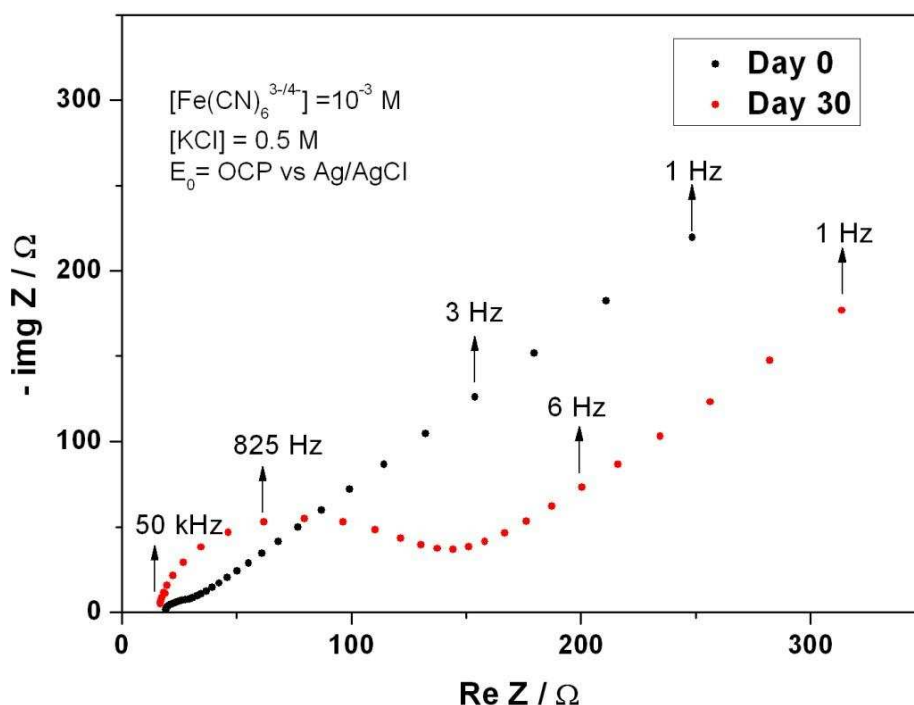


Figure 2.2 Comparison between the Nyquist plot of ‘as grown’ BDD electrode and that of the same electrode which has been exposed to air for 30 days.

2.1.2 Electrode fouling

The effects of fouling are much more severe than those associated with electrode ageing as k_0 in the former case is found to decrease by several tens of times after using the electrode in a biological medium. In order to demonstrate the effect of fouling, a set of 5 CV cycles from -0.4 V to 1.1 V vs Ag/AgCl at 100 mV s^{-1} was performed in human urine using a freshly prepared BDD electrode. After each trial EIS was carried out to assess the k_0 value. An oxidation peak (P1) was observed on the CV at approximately 0.5 V vs Ag/AgCl (figure 2.3). The peak P1 corresponds to the oxidation potential of uric acid and ascorbic acid in urine.¹² Chapter 4 is dedicated to the quantification process of uric acid in presence of ascorbic acid in human urine.

The amplitude of P1 is observed to significantly decrease after each trial. The attenuation of current is not because of diffusion-limited phenomena as the electrode was washed thoroughly in DI water and dried before each CV. Also the oxidation potential of this peak has shifted towards more positive potentials and the k_0 value decreases after each trial (figure 2.3 and table 2.1). Before the measurement, a k_0 value of 0.27 cm.s^{-1} was measured, whereas after five trials it decreased to less than $10^{-3} \text{ cm.s}^{-1}$. This clearly illustrates the effect of the fouling of the electrode.¹³ Human urine contains many proteins such as macroglobulin, fibrinogen, antigens of epithelial cells, etc.¹⁴ in addition to carbohydrates, hormones, fatty acids and other organic and inorganic compounds. When human urine is not diluted and used as the analyte these complex molecules get adsorbed on the electrodes surface thereby blocking the electron transport and reducing the electron transfer rate to considerable extend.

Table 2.1 Electron transfer rate (k_0) of ‘as grown’ electrode and values after subsequent scan in human urine.

	$k_0 \text{ (cm.s}^{-1}\text{)}$
As grown	0.27
After scan 1	0.011
After scan 2	0.005
After scan 3	0.003
After scan 4	0.002
After scan 5	0.001

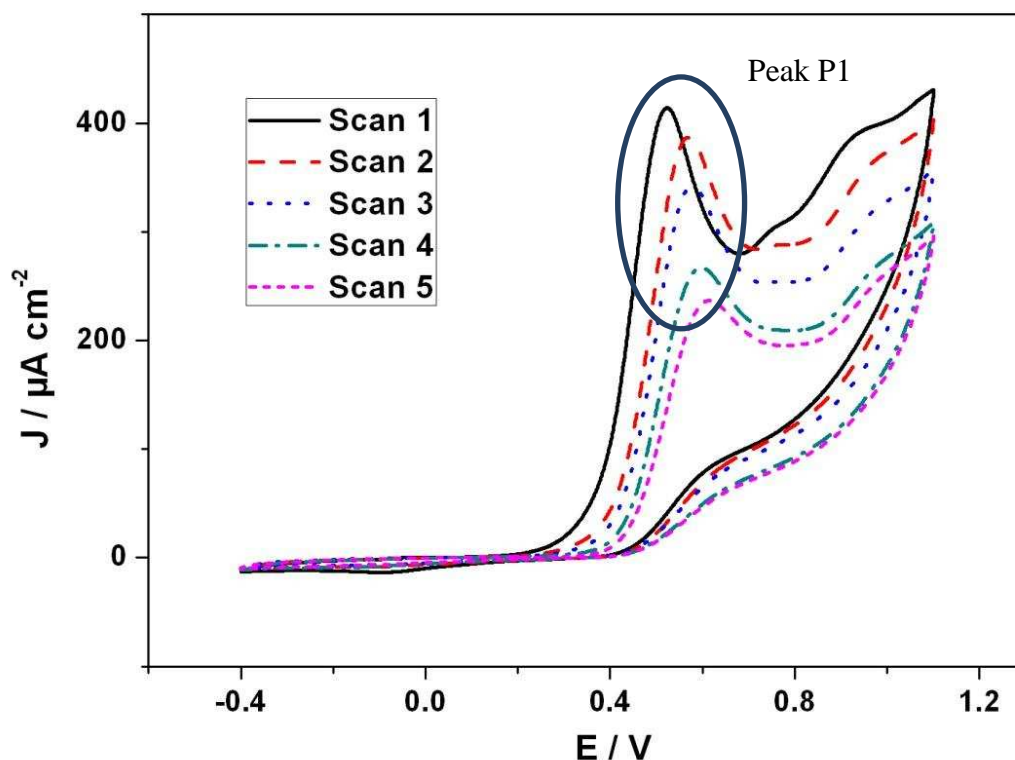


Figure 2.3 Cyclic voltammogram in human urine from -0.4 V to 1.1 V at 100 mV s^{-1} where J is the current density in $\mu\text{A.cm}^{-2}$ and E is the voltage in volts. The electrode was cleaned thoroughly in deionized water prior to each scan and hence the attenuation of the peak (P1) is due to fouling and not because the solution surrounding electrode is depleted of electro-active species.

2.2 Activation process

Several approaches have been investigated to overcome the issue of fouling and/or ageing. For instance, coating the electrochemical sensor with chemically-inert polymers such as Nafion® enhances the antifouling capability.⁶ Surfactant-modified electrodes also enhance the resistance to protein adsorption and cell adhesion. However, polymer or membrane deposition increases the degree of complexity of fabrication of the electrochemical sensor, decreases the electrode reactivity and, as a result, the lifetime of the modified electrode will be shorter than that of an ‘as grown’ electrode. Alternatively, the sono-electrochemical method provides in-situ cleaning accompanied with electrochemical measurement.⁴ Nevertheless the power consumption, accuracy of measurement and simplicity of the design

of the sensor have, in this case, to be compromised. Hydrogen plasma treatment is another approach that leads to clean H-terminated BDD surface.^{15,16} However, the use of plasma treatment is clearly not practical, especially when measurements have to be performed outside the laboratory.

Electrochemical techniques have also been developed to activate an aged or fouled electrode. In particular, an aged BDD electrode can be reactivated using cathodic pre-treatment by applying, typically, -3 V for 3 to 30 minutes in 0.5 M H₂SO₄ aqueous solution.⁹ Also the non-diamond sp² impurities can be eliminated by anodic treatment in aqueous electrolyte.¹⁵ Electrochemical reactivity of an aged electrode can be improved by performing 10 redox cycles in 0.5 M LiClO₄ aqueous electrolyte (de-aerated) from 400 μA.cm⁻² to -400 μA.cm⁻² at 100 mV s⁻¹.⁸ Rodrigo et al. have demonstrated that anodic treatment of a fouled electrode at 10 mA.cm⁻² for 30 minutes can enable one to recover the initial reactivity of the electrode.¹⁷ This is due to oxidation of the organic molecule to CO₂ by the electrogenerated hydroxyl radical (OH*). A pulsed cleaning technique has been reported by Mahé et al.¹⁸ where alternating current pulses of amplitude ± 250 mA.cm⁻² in 1 M HNO₃ were applied to clean the graphitic domains on diamond electrodes. The total activation time was, however, 400 seconds.

We have developed an improved EC activation process for BDD electrodes, based on the application of specific current or potential pulses, that leads to electrochemical cleaning and to the recovery of remarkable electron transfer rates (k_0 value above 10⁻³ cm.s⁻¹) with good stability and an activation time shorter than known in the prior art (as short as 200 ms). Based on the activation time, pulse duration and pulse amplitude, two protocols were empirically derived: ‘standard activation protocol’ and ‘standard cathodic activation protocol’. The details are explained in section 2.4. The standard activation protocol consists of a pulse train of 50 current pulses of alternating amplitude (10 mA.cm⁻² and -10 mA.cm⁻²) and of equal duration (100 ms) applied between working and counter electrodes in 0.5 M aqueous LiClO₄ solution. The ‘standard cathodic activation protocol’ consists of a train of 50 current pulses of amplitude -20 mA.cm⁻², duration of 110 ms and a duty cycle of 91%. The optimal values required depend on the electrolyte used and were therefore modified accordingly for other electrolytes.

This innovative EC treatment was tested on the aged electrode by using the ‘standard activation protocol’ to activate the electrode. It was observed that the electrode activity was recovered, with measured ΔE_p values brought back to 60 mV and k_0 values reaching $6.1 \times 10^{-2} \text{ cm.s}^{-1}$ after this novel EC treatment. The time required to bring back the lost reactivity of the aged electrode, in this case, was as low as 10 seconds. The ΔE_p and k_0 values of ‘as grown’, aged and activated electrode are summarized in table 2.2. With respect to other techniques as previously reported in the literature, this technique is much faster, can be performed using an extremely simple electronic setup (pulse generator), and requires lower power resources.

Table 2.2 Comparison of the peak-to-peak voltage separation (ΔE_p) and electron transfer rate (k_0) values of ‘as grown’, aged and activated electrode.

	ΔE_p (mV)	k_0 (cm.s^{-1})
‘as grown’	60	5.94×10^{-2}
Aged	85	5.04×10^{-3}
After Activation	60	6.05×10^{-2}

Similarly, the electrode fouled in human urine was treated with the EC activation technique using the following parameters: a set of 150 current pulses of alternating amplitudes (10 mA.cm^{-2} and -10 mA.cm^{-2}) and of equal duration (100 ms) was applied to the working electrode with respect to the counter electrode in 0.5 M aqueous LiClO_4 solution. The total number of pulses was tripled when compared to the ‘standard activation protocol’ because it was observed that the k_0 value after 50 pulses was not as high as that of the ‘as grown’ electrode (although significantly higher than 0.01 cm.s^{-1}). This corresponds to an overall activation time of 30 seconds.

The results were extremely encouraging as it can be observed in figure 2.4 that the CV curve after activation almost perfectly coincides with that of the first scan in urine. The difference in amplitude of the P1 peak for these two curves remained below 0.01% and the k_0 value was brought back to more than 0.2 cm.s^{-1} by this activation. Activation process also shifted the peak P1 back to 0.5 V vs Ag/AgCl which was initially shifted towards more positive potentials due to fouling. During the activation, adsorbed species were oxidized to carbon dioxide by the hydroxyl radicals that were electro-generated during pulsing and/or desorbed

by the gaseous species. The explanation of the activation process is described in detail in section 2.5.

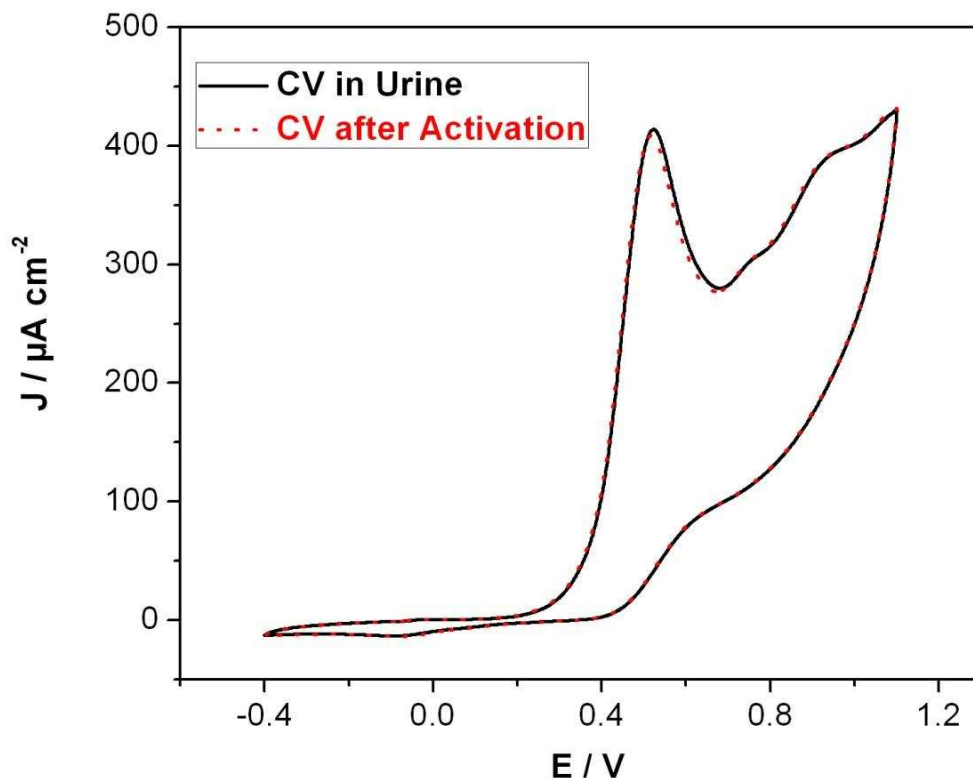


Figure 2.4 Comparison of the cyclic voltammogram of an ‘as grown’ electrode (solid line) and the same electrode after activation (dotted) where J is the current density in $\mu\text{A}\cdot\text{cm}^{-2}$ and E is the voltage in volts. The electrolyte is human urine and the scan rate is 100 mVs^{-1} .

2.3 Activation in other synthetic electrolytes

The aforementioned EC activation approach can also successfully be performed in most inorganic salt solutions as well as in organic solutions. In order to demonstrate this, electrodes were fouled and then activated in various electrolytes. For example, the BDD electrodes were fouled in red wine (Chassagne-Montrachet 1^{er} Cru) by maintaining them at 0.7 V vs Ag/AgCl for 20 s. The red wine sample was particularly chosen since it led to high levels of electrode fouling. The fouled electrodes exhibited k_0 values below $10^{-3}\text{ cm}\cdot\text{s}^{-1}$. The electrodes were then activated in different salt solutions of 0.2 M using 8 alternating current pulses ($+1.5\text{ mA}\cdot\text{cm}^{-2}$ and $-1.5\text{ mA}\cdot\text{cm}^{-2}$) of 2 seconds each. The k_0 values after activation in each salt solution is

summarized in table 2.3. This demonstrated the role of cathodic current pulses in electrode cleaning.

For non-electroactive electrolytes such as LiClO_4 and Na_2SO_4 at this current density, the negative potential goes beyond 1.6 V where H_2 gas is electro-generated. The electro-generated H_2 gas helps in desorption of adsorbed organic species and H-termination of the electrode. Electrochemical hydrogenation of the surface is due to attachment via a production of hydrogen radicals at negative voltages.¹⁹ Whereas for the electroactive electrolyte the current generated was mainly due to metal deposition rather than H_2 electro-generation and hence the k_0 value is lower. At a relatively low current density of 1.5 mA.cm^{-2} , electroactive species such as Cu, Zn and Mn ions are electrodeposited on the surface and thereby decrease the yield of OH^* , which also plays a critical role in electrode cleaning.

Table 2.3 The electron transfer rate (k_0) value determined from the Nyquist plot after activation in a range of salt solutions.

Salt	Solvent	$k_0 \text{ (cm.s}^{-1}\text{)}$
LiClO_4	Water	$0.0268 \pm 8 \times 10^{-4}$
Na_2SO_4	Water	$0.0205 \pm 6 \times 10^{-4}$
MnSO_4	Water	0.0108 ± 0.004
ZnSO_4	Water	$0.0027 \pm 7 \times 10^{-4}$
CuSO_4	Water	$0.0013 \pm 6 \times 10^{-4}$
H_2SO_4	Water	$0.0197 \pm 3 \times 10^{-3}$
TBATFB	Acetonitrile	$0.0095 \pm 4 \times 10^{-4}$

The deposition of metal was observed by the anodic stripping voltammogram where Zn was stripped at -0.9 V, Cu at 0.4 V versus Ag/AgCl and for Mn two peaks were observed (oxidation and reduction peaks). Figure 2.5 shows the anodic stripping voltammogram indicating that at low current densities metal ions were deposited on the surface. It was observed that at higher current densities ($> 10 \text{ mA.cm}^{-2}$), the k_0 value was higher after activation in some electro-active electrolyte because the yield of H_2 generation and H termination increases with current density. Activation process in 0.2 M tetrabutylammonium tetrafluoroborate (TBATFB) in acetonitrile solution demonstrated that the activation process

can also be successfully performed in organic solvents to achieve considerably high k_0 values above $10^{-3} \text{ cm.s}^{-1}$.

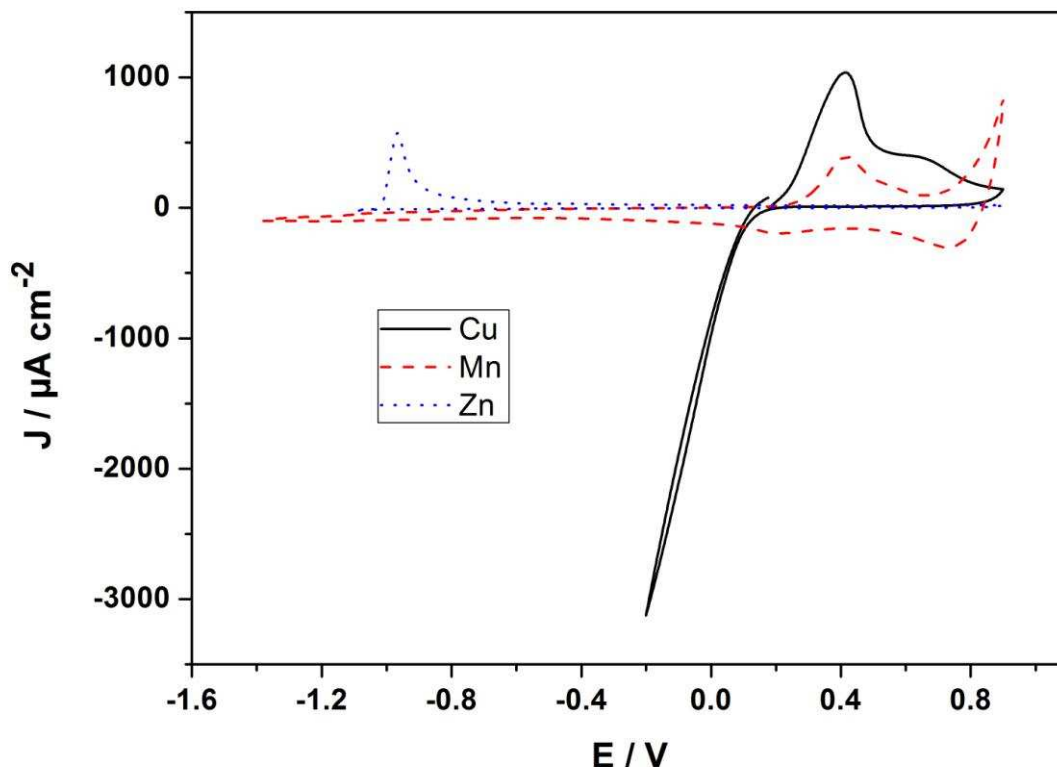


Figure 2.5 Stripping voltammogram for copper, manganese and zinc. The electrolyte solution contained 0.2 moles of either Cu^{2+} , Mn^{2+} or Zn^{2+} ions.

2.4 Influence of pH, current density and number of pulses on activation

To probe the influence of factors such as the amplitude of the current density, the pH of the electrolytic solution and the number of pulses in a pulse train, one such parameter was varied at a time while the two others were kept constant. To understand the influence of pH and number of pulses, the total activation duration was fixed at 16 seconds. To analyze the influence of current density on activation, the duration of activation was limited to 100 ms because the current density was varied from $1 \mu\text{A.cm}^{-2}$ to 100 mA.cm^{-2} . 16 seconds of activation at 100 mA.cm^{-2} electrolyzes the solution rapidly and may also affect the surface termination although BDD is known to be robust. At first, the electrodes were fouled in the

red wine to reach k_0 values below $10^{-3} \text{ cm.s}^{-1}$ and then activated in 0.5 M aqueous LiClO_4 solutions with different parameters.

2.4.1 pH vs activation

After fouling, the electrodes were activated in 0.5 M aqueous LiClO_4 solutions with varying pH values. The pH was adjusted to 1.5, 4.5, 7, 9.5 and 12.5 by adding either H_2SO_4 or NaOH . Activation was performed using 8 current pulses of alternating amplitude (1.5 mA.cm^{-2} and -1.5 mA.cm^{-2}) and duration of 2 seconds each. The more the alkaline the solution, the better the activation of the electrode as displayed in figure 2.6. The k_0 value of the electrode after activation in a solution of pH 1.5 was found to be $1.34 \times 10^{-2} \text{ cm.s}^{-1}$ whereas that of an electrode activated in alkaline solution of pH 12.5 was $4.82 \times 10^{-2} \text{ cm.s}^{-1}$.

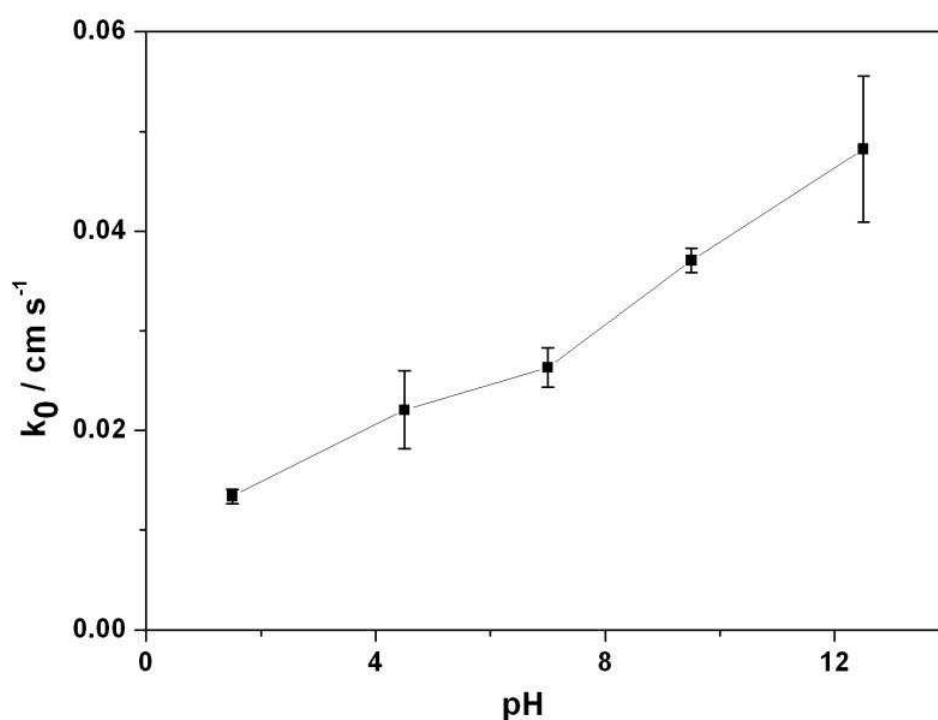


Figure 2.6 pH dependence of the activation process. The higher the pH, the better the activation as well as the value of electron transfer rate (measured in 1mM ferro/ferricyanide in 0.5 M KCl) k_0 measured in cm.s^{-1} .

We observed an increase of around 250% in k_0 when the fouled electrode is activated in an alkaline medium as compared to that in an acidic medium. This could possibly be associated with the fact that, when alternating positive and negative pulses were applied through the

working electrode, OH^* radicals generated may play a relevant role in oxidizing organic compounds.^{20,21} Electrode fouling is associated with the deposition or adsorption of organic compounds on the electrode surface and the OH^* radicals oxidize them to CO_2 . Alkaline solution produce more OH^* radicals when compared to acidic solutions.

2.4.2 Current density vs activation

Increasing the current density of the current pulses causes a very dramatic increase in k_0 values (figure 2.7). The electrodes were fouled in red wine and then were activated in 0.5 M aqueous LiClO_4 solution using 4 alternating current pulses of 100 ms duration each, while the pH of the solution was kept constant (pH = 4.5). This activation was performed using varying current density amplitudes of $1 \mu\text{A}\cdot\text{cm}^{-2}$, $10 \mu\text{A}\cdot\text{cm}^{-2}$, $100 \mu\text{A}\cdot\text{cm}^{-2}$, $1 \text{mA}\cdot\text{cm}^{-2}$, $10 \text{mA}\cdot\text{cm}^{-2}$ and $100 \text{mA}\cdot\text{cm}^{-2}$, respectively. The k_0 of the electrode after activation using a current density of $1 \mu\text{A}\cdot\text{cm}^{-2}$ was $6.97 \pm 0.8 \times 10^{-4} \text{cm}\cdot\text{s}^{-1}$ and that of an electrode activated using a current density of $100 \text{mA}\cdot\text{cm}^{-2}$ was $1.71 \pm 0.3 \times 10^{-2} \text{cm}\cdot\text{s}^{-1}$. Maintaining both the total time of activation and pH constant, the result is an increase in the k_0 value by up to a factor 25 with the current density.

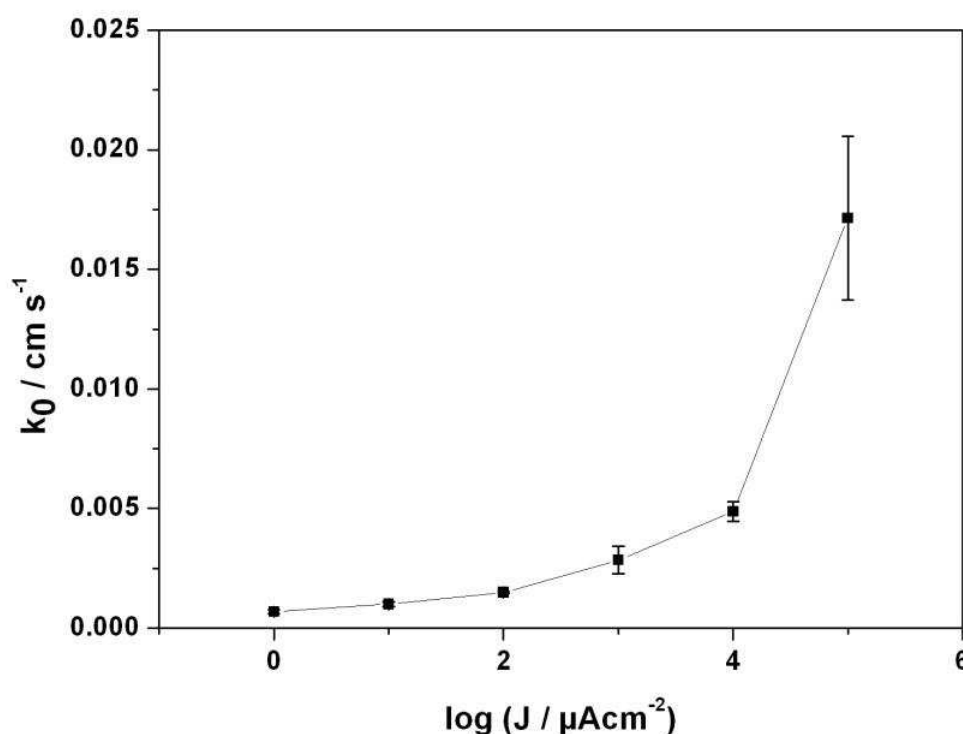


Figure 2.7 Effect of current density on the activation process. The higher the current density, the higher the electron transfer rate k_0 ($\text{cm}\cdot\text{s}^{-1}$), where J is the current density in $\mu\text{A}\cdot\text{cm}^{-2}$.

2.4.3 Number of pulses vs activation

The number of pulses required to activate the electrode also plays a very critical role. This was assessed by varying the total number of pulses per activation while the total activation time, pH and current density were kept constant (pH = 4.5). Alternating current pulses with absolute amplitude of 1.5 mA.cm^{-2} were applied through the fouled electrode in 0.5 M LiClO_4 solution and the total activation time was 16 seconds. The fouled electrode was activated using series of 2, 4, 8, 16, 32 and 64 alternating pulses and with the corresponding pulses exhibiting durations of 8, 4, 2, 1, 0.5 and 0.25 seconds, respectively. It was observed that the higher the number of pulses for a finite activation time, the better the yield of activation. When two alternating pulses of 8 seconds each were applied, the post activation k_0 was $8.2 \pm 0.7 \times 10^{-3} \text{ cm.s}^{-1}$, and values reached $2.1 \pm 0.1 \times 10^{-2} \text{ cm.s}^{-1}$ for k_0 when 64 alternating pulses were applied (figure 2.8). A 250% increase was observed for the k_0 value when the number of pulses was increased from 2 to 64 while the total activation time was kept constant for both. This justifies using several pulses instead of just 2 pulses (alternating cathodic and anodic pulses).

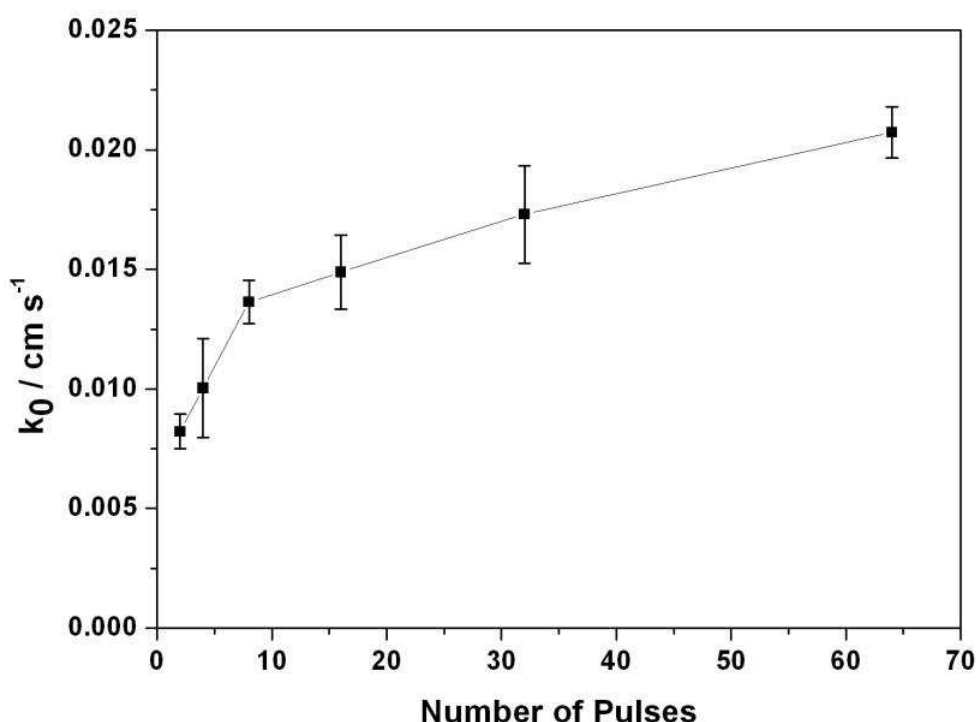


Figure 2.8 Impact of the number of pulses on the activation process, where k_0 is electron transfer rate (cm.s^{-1}).

From figure 2.8 it is clear that there is a large increase in k_0 value when the number of pulses was increased from 1 to 10 and the slope tends to level off when the number of pulses was increased further. Similarly, there is a large increase in k_0 value when the current density was increased beyond 10 mA.cm^{-2} as seen in figure 2.7. Based on these observations it is suggested that the ‘standard activation protocol’ successfully cleans the electrode in a non-reactive aqueous electrolyte: Positive and negative trains of pulses of the same amplitude ($\pm 10 \text{ mA.cm}^{-2}$) and duration (100 ms each) and series of 100 such pulses.

2.5 Surface analysis and activation mechanism

The surface analysis was performed using X-ray Photoelectron Spectroscopy (see chapter 1, section 1.4.1 for more details). XPS analysis was carried out on two ‘as grown’ electrodes: one sample was analyzed directly after growth and the other sample was activated using ‘standard activation protocol’ prior to the XPS analysis. For the ‘as grown electrode’ no oxygen was detected using XPS corresponding to values below the detection threshold of 0.5 at %. In addition to the C-C sp^3 / C-H major peak located at 283.9 eV, the C1s signal exhibits a shoulder at + 0.6 eV corresponding to CH_x ($x>1$) bonds which represent 19% of the C1s total area (table 2.4). This signature was previously reported for hydrogenated diamond surfaces.⁸ Finally, a negligible contribution (< 0.5 at %) was detected at 282.5 eV corresponding to sp^2 carbon. This is related to the grain size of nanocrystalline boron-doped diamond films leading to a weak contribution from grain boundaries.

Table 2.4 Percentages of total C1s area of the XPS components for ‘as grown’ electrode and electrode after EC activation.

	C-C sp^2	C-C sp^3 / C-H	CH_x	C-OH	C-O-C
‘As grown’ BDD	< 0.5 %	81 %	19 %	-	-
Activated BDD	< 0.5 %	72 %	20 %	6 %	2 %

After activation, the oxygen concentration extracted from the O1s core level was 3.8 at %. Two new contributions have to be taken into account at the C1s core level. The first one is located at + 1.3 eV from the C-C sp^3 / C-H peak and could be assigned to C-OH bonds. The second weaker contribution at 1.9 eV from the C-C sp^3 is attributed to C-O-C bonds. The respective area ratios are given in table 2.4. This surface chemistry is close to the one

measured after activation in LiClO₄ electrolyte where C-OH (4 %) and C-O-C (5 %) contributions were also present.⁸ Figure 1.4 and 2.9 shows the XPS spectra of ‘as grown’ and activated BDD electrodes.

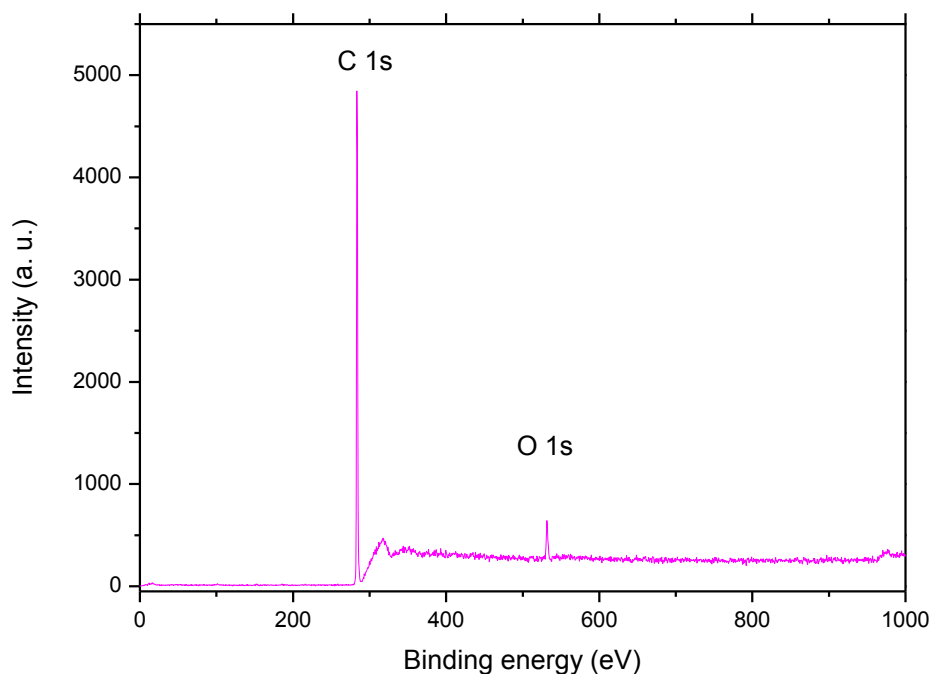


Figure 2.9 XPS of BDD electrode after ‘standard activation protocol’

During EC activation, three mechanisms are believed to occur:

- (i) oxidation of adsorbed organic molecule by OH*
- (ii) H-termination during cathodic pulsing¹⁹
- (iii) desorption of adsorbed organic compounds by electro-generated gaseous species.

It was experimentally observed that the activation in basic solution has yielded better reactivity when compared to acidic solutions. OH* formation occurs via the following chemical reaction:²²



The OH* generated is an oxidant and it oxidizes the adsorbed organic molecule to CO₂.



The concentration of OH^* increases progressively until a constant value is reached due to mass transfer limitations or chemical destruction of the OH^* formed. At higher pH more OH^* is generated. LiClO_4 is a non-electroactive species and hence the only oxidant species present is OH^* .

The double layer capacitance of the electrode was measured before and after activation. Two techniques were used for measurement of capacitance: CV (the electrode was scanned in 0.5 M LiClO_4 solution at 100 mV s^{-1}) and charge-discharge curves (I-t plot, where the electrode was held at 0 V for 0.005 s and at 0.05 V for 0.005 s). Figure 2.10 shows the voltammogram of 'as grown' and activated BDD electrodes. There was no significant difference in the capacitance value (less than 0.5%) before and after activation. XPS analysis, high k_0 value and negligible change in double layer capacitance indicate that there is no significant difference between 'as grown' electrode and EC activated electrode in terms of electrochemical reactivity and surface termination.

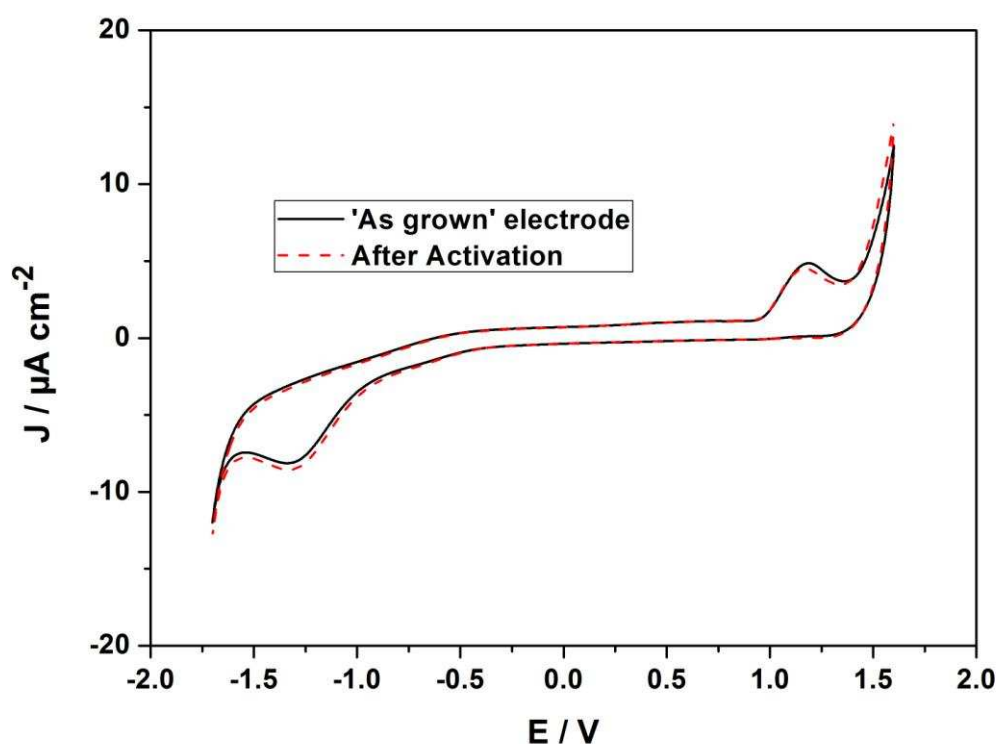


Figure 2.10 Cyclic voltammogram of BDD electrode before and after 'standard activation protocol' scanned at 100 mV.s^{-1} .

In order to investigate the action of EC activation on the electrode surface, a biofilm was grown on the electrode surface. BDD electrodes were horizontally immersed in a domestic aquarium (aerated and maintained at 23-28 °C) containing fish and aquatic plants for 90 days. The electrodes were then rinsed in DI water, dried and were observed under optical microscope. A biofilm had formed on the surface which consisted of several microbial communities. SEM images (figure 2.11) shows that the BDD surface was masked by the microbes.

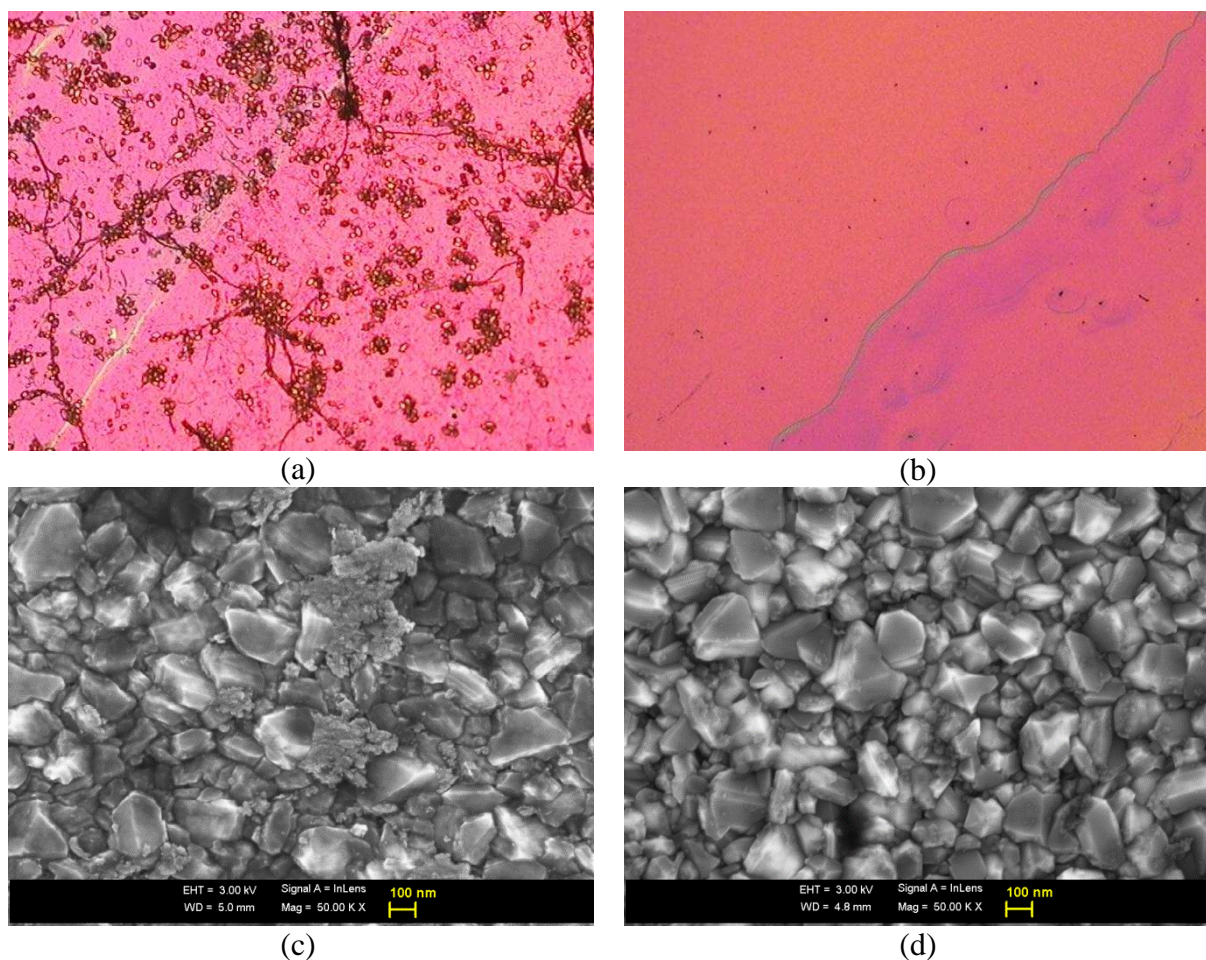


Figure 2.11 Optical microscopic (x10 magnification) and SEM images of electrode deposited with biofilm (a,c) and after three ‘standard activation protocols’ (b,d).

Electrochemical characterization such as EIS and CV were performed between various steps of EC activation. Table 2.5 summarizes ΔE_p and a k_0 values after each activation steps. It took three ‘standard activation protocols’ to clean the electrode completely and get a ΔE_p value (in $[\text{Fe}(\text{CN})_6]^{3-/4-}$ solution) of 60 mV and $k_0 > 0.1 \text{ cm}\cdot\text{s}^{-1}$. It was observed from SEM and optical images that the microorganisms had been completely removed by the three of ‘standard

activation protocol'. Three processes could explain the activation process: OH* might have destroyed the microorganisms, electro-generated O₂ and H₂ gas bubbles helped in desorbing the attached life and/or cathodic pulses have H-terminated the surface.

Table 2.5 Comparison of the peak-to-peak voltage separation (ΔE_p) and electron transfer rate (k_0) values for an electrode deposited with biofilm and after each 'standard activation protocol'.

	ΔE_p (mV)	k_0 (cm.s ⁻¹)
Biofilm	381	3.1×10^{-4}
After Activation 1	178	1.02×10^{-3}
After Activation 2	83	1.3×10^{-2}
After Activation 3	60	0.11

The same approach was also conducted in urine. Four H-terminated BDD samples were prepared: sample 1 is an 'as grown' BDD electrode, samples 2, 3 and 4 are electrodes fouled by 5 CV scans in human urine.

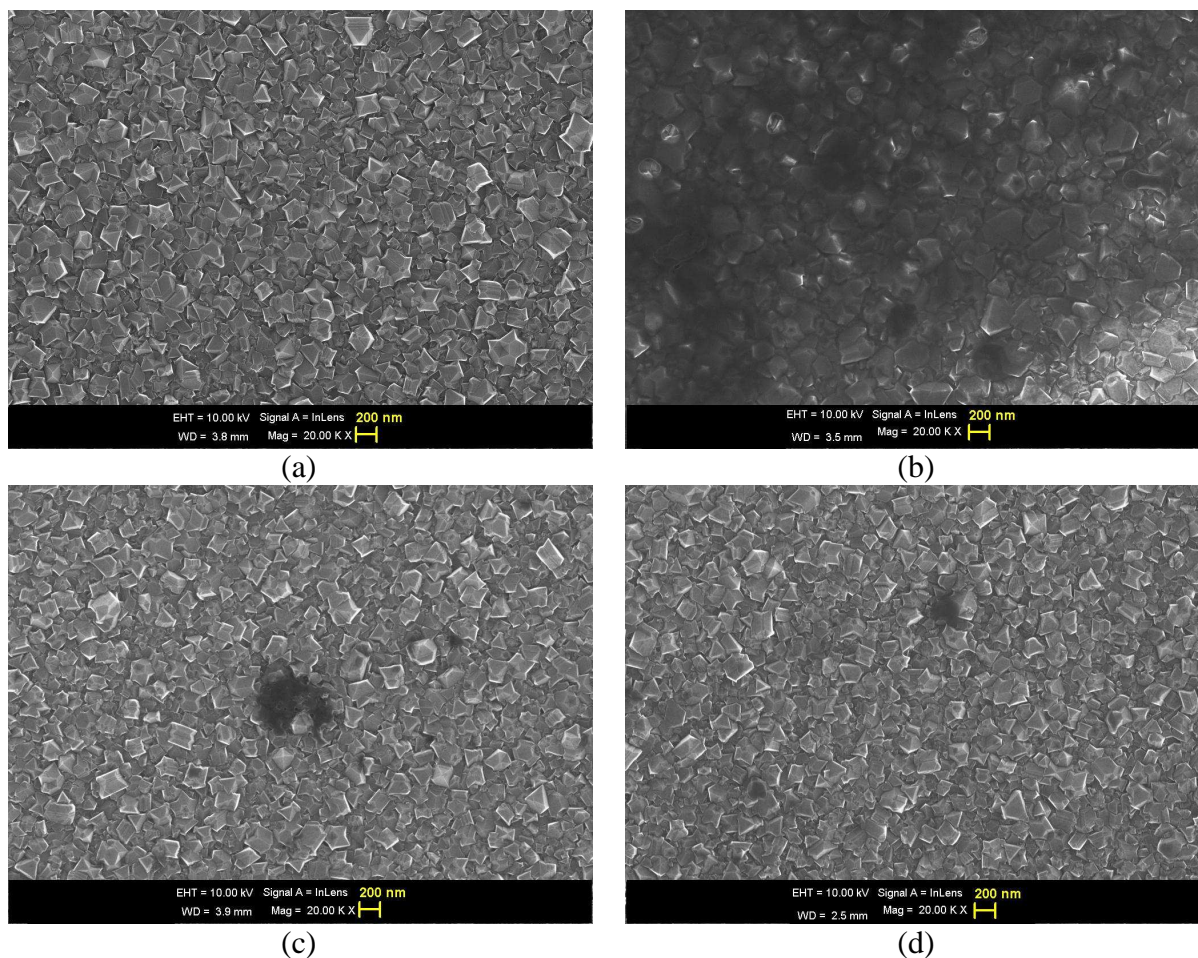


Figure 2.12 SEM images of as grown electrode (a), electrode after being fouling in urine (b) after activation in urine (c) and after activation in LiClO_4 (d)

Samples 3 and 4 were cleaned using ‘standard cathodic protocol’ in urine and ‘standard activation protocol’ respectively. Activation of electrode in urine is explained in detail in section 2.6. The fouled sample (no. 2) appeared very cloudy under SEM (figure 2.12) and the underlying BDD film could not clearly be observed suggesting the presence of nonconductive biomolecule (enzyme, protein, fat etc.) layer over the BDD film.

Samples 1 and 4 exhibit similar aspects suggesting that sample 4 has been almost cleaned with the help of the OH^* generated that has oxidized the adsorbed biomolecules, the desorption of the adsorbed species by electro-generated H_2 and O_2 bubbles and of the cathodic pulse H-termination (observed by high k_0 values). Sample 3 was almost cleaned with a less cloudy appearance. There was no generation of OH^* as the activation was cathodic. Hence the cleaning was due to desorption of the adsorbed species by electro-generated H_2 bubbles and H-termination of surface (observed by high k_0 values).

2.6 In-situ activation in biological fluids

A set of 9 trials each comprising of 3 CV scans were performed in human urine and the current densities of the 1st peak (P1) of the first scan were recorded. The electrode was then activated in urine for all the trials except for trial no: 4, 7, and 9. The EIS of the electrode was recorded in between each trials to enable the comparison of the k_0 values between activated and non-treated trials.

Activation in human urine was performed using a train of negative current pulses of 50 pulses. Each pulse had an amplitude of -20 mA.cm^{-2} , a duration of 110 ms and a duty cycle of 90.91%. It was observed that the mean value of k_0 for an activated electrode was $0.094 \pm 006 \text{ cm.s}^{-1}$. When the electrode was not activated this value was reduced by a factor of 40 with respect to that of an activated electrode. From figure 2.13 it appears that once the electrode is activated following a non-treated trial, one can bring back the initial reactivity of the electrode as well as a k_0 value close to mean values.

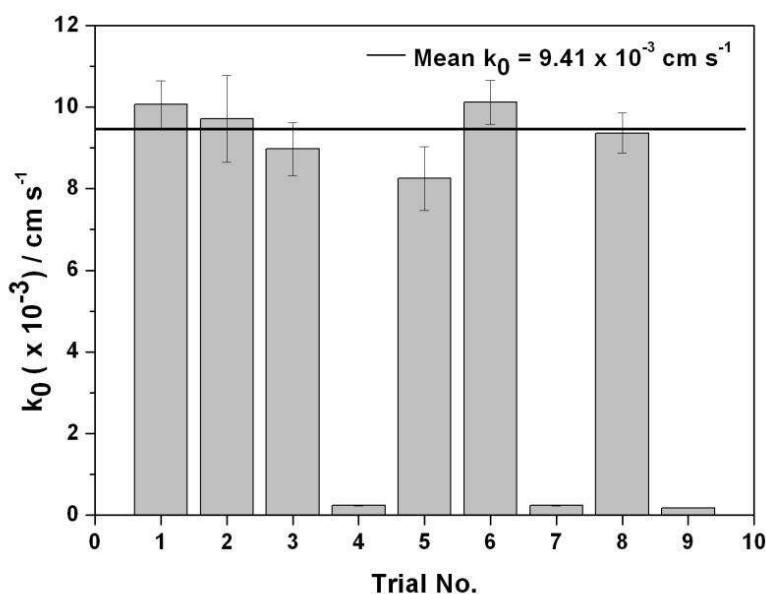


Figure 2.13 Electron transfer rate k_0 measured after each trial. For trial no: 4, 7 and 9, the electrode was not activated in urine. For all other trials, the electrode was activated in urine and as a result the k_0 of the electrode is close to 0.01 cm.s^{-1} .

Similarly the mean current density J_1 of the peak P1 for the activated trials was observed to be $344.71 \pm 9.7 \mu\text{A.cm}^{-2}$. For the non- treated trials, this value was only $3/4^{\text{th}}$ of the activated trials. This value was brought back to mean values by activation in urine as seen in figure

2.14. Although cleaning in non-electroactive solution is preferable (as the peak values differ by less than 0.01%), in-situ activation can be an alternative solution to cleaning owing to the low standard deviation of J_1 .

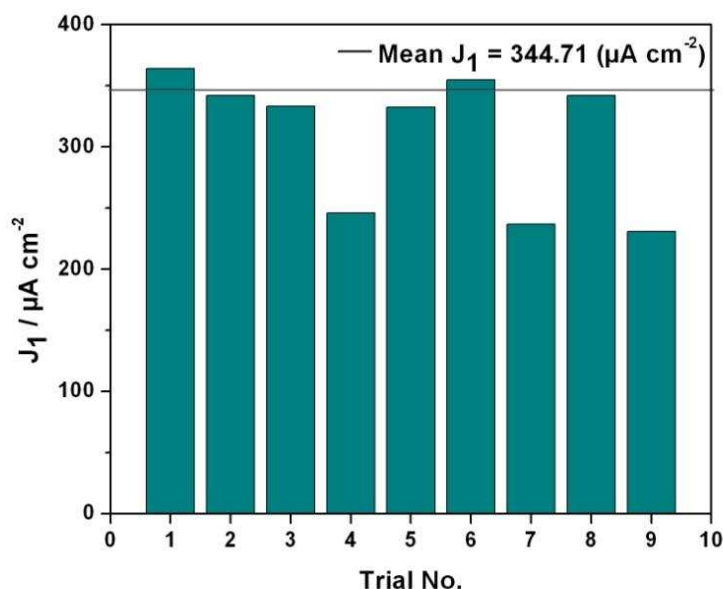


Figure 2.14 Current density J_1 ($\mu\text{A.cm}^{-2}$) of the peak P1 measured from CV in urine versus trial number. The peak values J_1 of activated trails are close to $350 \mu\text{A.cm}^{-2}$ and if the electrodes are not activated (trial no: 4, 7 and 9) this value dropped by 25%.

Another experiment used a BDD electrode of high reactivity ($k_0 = 0.1 \text{ cm.s}^{-1}$) dipped in bovine blood for two hours. This resulted in a drop of k_0 to 0.007 cm.s^{-1} . The EC activation was then performed directly in bovine blood by applying a train of negative current pulses consisting of 50 pulses where each pulse had an amplitude of -20 mA.cm^{-2} , a duration of 110 ms and a duty cycle of 90.91% (same conditions as those for urine). EIS measurement showed that the k_0 value was brought back to 0.012 cm.s^{-1} after activation.

In summary, we concluded that this very novel activation process has very significant potential in the monitoring of analytes in real samples such as blood, urine etc. because of (i) the very short activation times and (ii) the tunable current density. However, in real samples, adsorbents could accumulate on the surface of the electrode which can be desorbed by applying stronger negative pulses (indicated by an increase in k_0 value after activation).

Conclusion

It has been demonstrated that this electrochemical treatment retrieves the lost reactivity of BDD electrodes when aged in air as well as in solutions or fouled by a medium. The higher the current density, the lower the time required to activate, and the better the result. By tuning the above mentioned parameters (current density, pulse duration and number of pulses, and type of the electrolyte, etc.), one can increase the charge transfer rate constant k_0 to reach values above 0.01 cm.s^{-1} .

The other advantage of this technique is to enhance the reusability of the BDD electrode. As opposed to other more conventional pre-treatments techniques reported in the literature, such as anodic, cathodic or thermal ones, this novel electrochemical pre-treatment is relatively simple, fast, and requires a minimum of energy.

The real breakthrough is that it can be successfully done directly in the measuring solution especially in a biofluid. As a result this electrochemical activation can be performed prior to analytical measurements to ensure reliable and reproducible results, especially when the electrode has not been used for a long period of time. Although an aqueous electrolyte containing non-electroactive species is preferred for EC activation, it can also be done in biological fluids such as blood, urine etc, thereby opening the field for in-situ analysis. An example of analyte quantification (uric acid concentration) with in-situ cleaning in human urine is described in detail in chapter 4. It also opens the door to long term field measurements where electrodes are prone to fouling when immersed for long periods of time in liquids, including on-line measurement since electrodes may be regenerated very quickly in-situ within biological medium.

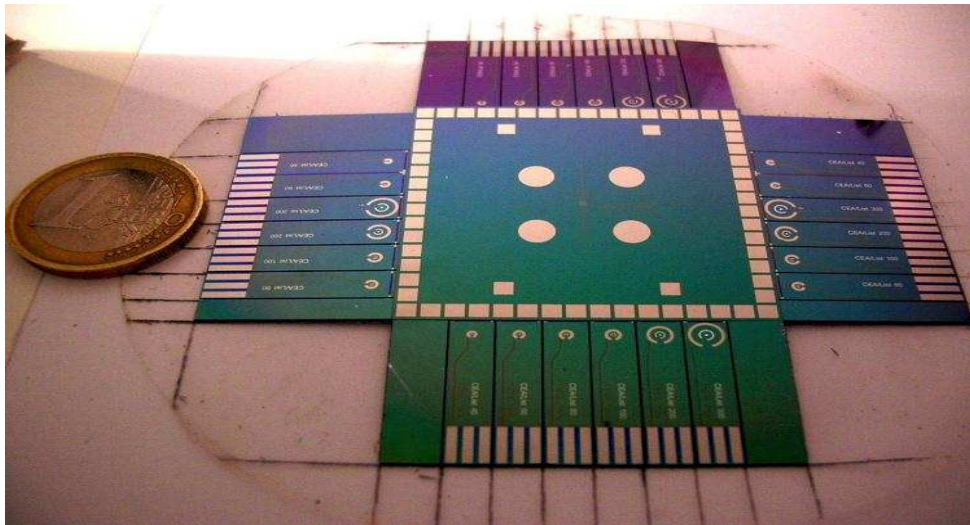
Bibliography

- (1) Iniesta, J.; Michaud, P. A.; Panizza, M.; Comninellis, C. *Electrochemistry Communications* **2001**, 3, 346–351.
- (2) Montilla, F.; Michaud, P. A.; Morallon, E.; Vazquez, J. L.; Comninellis, C. *Electrochimica Acta* **2002**, 47, 3509–3513.
- (3) Iniesta, J.; Michaud, P. A.; Panizza, M.; Cerisola, G.; Aldaz, A.; Comninellis, C. *Electrochimica Acta* **2001**, 46, 3573–3578.
- (4) Davis, J.; Compton, R. G. *Analytica Chimica Acta* **2000**, 404, 241–247.
- (5) Hin, F. Y. Y.; Lowe, C. R. *Analytical chemistry* **1989**, 59, 2111–2115.
- (6) Yantasee, W.; Charnhattakorn, B.; Fryxell, G. E.; Lin, Y.; Timchalk, C.; Addleman, R. S. *Analytica chimica acta* **2008**, 620, 55–63.
- (7) Wang, J.; Hutchins, L. D. *Analytical chemistry* **1985**, 57, 1536–1541.
- (8) Vanhove, E.; de Sanoit, J.; Arnault, J. C.; Saada, S.; Mer, C.; Mailley, P.; Bergonzo, P.; Nesladek, M. *Physica Status Solidi (a)* **2007**, 204, 2931–2939.
- (9) Salazar-Banda, G. R.; Andrade, L. S.; Nascente, P. A. P.; Pizani, P. S.; Rocha-Filho, R. C.; Avaca, L. A. *Electrochimica Acta* **2006**, 51, 4612–4619.
- (10) Duo, I.; Levy-Clement, C.; Fujishima, a.; Comninellis, C. *Journal of Applied Electrochemistry* **2004**, 34, 935–943.
- (11) Ramesham, R. *Thin Solid Films* **1998**, 315, 222–228.
- (12) Popa, E.; Kubota, Y.; Tryk, D. A.; Fujishima, A. *Analytical chemistry* **2000**, 72, 1724–1727.
- (13) Salimi, A.; Mamkhezri, H.; Hallaj, R. *Talanta* **2006**, 70, 823–32.
- (14) Anderson, N. G.; Anderson, N. L.; Tollaksen, S. L. *Clinical chemistry* **1979**, 25, 1199–210.
- (15) Kraft, A. *International Journal of Electrochemical Science 2* **2007**, 2, 355–385.
- (16) Tryk, D. a.; Tsunozaki, K.; Rao, T. N.; Fujishima, a. *Diamond and Related Materials* **2001**, 10, 1804–1809.
- (17) Rodrigo, M. a.; Michaud, P. a.; Duo, I.; Panizza, M.; Cerisola, G.; Comninellis, C. *Journal of The Electrochemical Society* **2001**, 148, D60.
- (18) Mahé, E.; Devilliers, D.; Comninellis, C. *Electrochimica Acta* **2005**, 50, 2263–2277.

- (19) Hoffmann, R.; Kriele, A.; Obloh, H.; Hees, J.; Wolfer, M.; Smirnov, W.; Yang, N.; Nebel, C. E. *Applied Physics Letters* **2010**, 97, 052103.
- (20) Panizza, M.; Cerisola, G. *Electrochimica Acta* **2005**, 51, 191–199.
- (21) Canizares, P.; Garcia-Gomez, J.; Lobato, J.; Rodrigo, M. A. *Industrial & Engineering Chemistry Research* **2003**, 42, 956–962.
- (22) Marselli, B.; Garcia-Gomez, J.; Michaud, P.-A.; Rodrigo, M. A.; Comninellis, C. *Journal of The Electrochemical Society* **2003**, 150, D79–D83.

CHAPTER III

Microelectrode: Design, fabrication and characterization



Introduction

Microelectrodes made from noble metals like platinum¹, gold², as well as silicon³ have a long history as neural electrodes. However, they are known to suffer from long term stability. Other materials such as functionalized hydrophilic Carbon nanotubes (CNT) have also been used in microelectrode arrays (MEA) as a novel prototype neural interface due to their high charge injection limit.⁴ However, the cytotoxicity of CNT and the biocompatibility issue, especially during long term in-vitro measurements, remains an issue to address.⁵ Titanium nitride and iridium oxide microelectrodes are extensively used for electrophysiological applications owing to their enhanced charge injection limit.⁶ Although these materials possess high double layer capacitance, the reduced potential window and high background current limit their use in electro-analytical applications.

Boron-doped diamond exhibits superior electrochemical properties over other conventional electrode materials, in particular its bio-inertness,⁷ corrosion resistance and long term stability.⁷⁻⁹ Thus the advantage of using MEAs over macro-electrodes has been further improved by combining their unique properties resulting from geometrical characteristics with the excellent electrochemical properties of BDD materials.¹⁰⁻¹³ Several interconnected and individually addressable diamond MEAs have been described in the literature: Hess et al. have reported on the fabrication and characterization of a 10 channel diamond on polymer MEA,¹⁴ Gao et al. on a 4 channel MEA to detect catecholamine.¹⁵ However for electrophysiological applications, much more miniaturized electrodes are desirable to record more accurately cell networks or organ (spinal cord, retina, etc.) communication mechanisms. This led us to the fabrication of a BDD ultra-MEA (UMEA) consisting of an array of 64 multiple electrodes, where each electrode is individually connected to a single electrical connector and then to a multichannel readout system. In addition to individually addressable UMEAs, strip microelectrodes and ultramicroelectrodes and interconnected MEAs were fabricated for electro-analytical applications.

The detailed fabrication processes of the different types of microelectrodes and MEAs are described in this chapter. The fabricated electrodes were characterized using SEM and electrochemical techniques such as cyclic voltammetry (CV) and electrochemical impedance spectroscopy (EIS) to appreciate the electrodes' performances namely their limiting currents (i_{lim}), electron transfer rates (k_0), electrochemical windows and background currents (i_{BG}) etc.

They are the most efficient techniques to detect any cracks or discontinuity of the insulating layer and analyzing EC properties of individual BDD UMEs.

3.1 Technological process

This work was carried out in close collaboration with ESIEE, Paris (École Supérieure d'Ingénieurs en Électronique et Électrotechnique) where the clean room facilities as well as know-how were used. The main goal was not to optimize the size of the electrode, but rather to fabricate a working device with minimal leakage current and active electrodes. Several types of designs were explored. Here we will describe just 2 types of designs (1 and 2) used to fabricate the microelectrode strips and MEAs to highlight what are the difficulties in developing such a process, and how alternatives have to be sought. In design 1 diamond was grown after the deposition of the metal contacts and passivation layer, whereas in design 2, diamond was grown prior to the deposition of metal tracks and passivation layer.

3.1.1 Design 1

Figure 3.1 shows the schematics of the fabrication process associated with design 1. Silicon dioxide insulation layer was grown on 4 inch silicon wafers. The wafers were oxidized in an oxidation oven at 1323 K, under a H₂O vapor flow to form a 500 nm thick silicon dioxide layer.¹⁶ The process time was 35 minutes.

Titanium/platinum/titanium (Ti/Pt/Ti) tracks were deposited by lift-off on the top of the oxide layer. Clariant Nlof 2020 was used as the sacrificial photoresist material. It was observed that diamond exhibits poor adhesion on Pt and SiO₂ layers and hence Ti/Pt/Ti assembly was used. The Ti layer also prevents the formation of Platinum silicide, which display a quite high resistivity.¹⁷ The thickness of the Ti and Pt layers were 50 and 150 nm respectively and 10 - 20 μm wide. A 500 nm thick silicon dioxide layer was deposited onto the substrate in order to isolate the metal tracks from the electrolyte solution. Then a conventional lithography process was carried out to define the opening of the oxide layer (5-25 μm in diameter).

Detonation diamond nanoparticles were spread onto the processed wafers.¹⁸ Diamond nanoparticles were dispersed in deionized water, and polyvinyl alcohol (PVA) was added to the solution in adequate amount and dissolved in colloidal solution by sonication. A 4 inch silicon wafer was seeded with 0.01% wt/wt diamond nanoparticles, 1.5% wt/wt PVA using spin coater. The nanoparticles were fixed on the substrate by subjecting it to short diamond

growth (5-10 minutes) in a SEKI 6500 reactor (later known as “SEKI”). The samples were exposed to hydrogen (99.4%)/methane (0.6%) plasma. The typical density range of the nanoparticles was of 10^8 - 10^{11} cm⁻². The microwave power was adjusted to 3000 W, gas flow at 200 SCCM, pressure to 35 mBar and temperature to 650 °C. After the growth period, the PVA is completely removed from the surface and nanoparticles had grown slightly and fixed on silicon wafer.

Next, an aluminum hard mask was deposited over the electrode areas by photolithography and the diamond nanoparticles outside these protected areas were etched away using ultra short RIE under oxygen/argon plasma.¹⁹ The protective aluminium layer was removed by wet etching. The diamond growth was resumed with the conditions described in chapter 1 section 1.3. The fabricated diamond electrodes exhibited a thickness of approximately 300 nm and diameter varying from 10 – 100 μm.

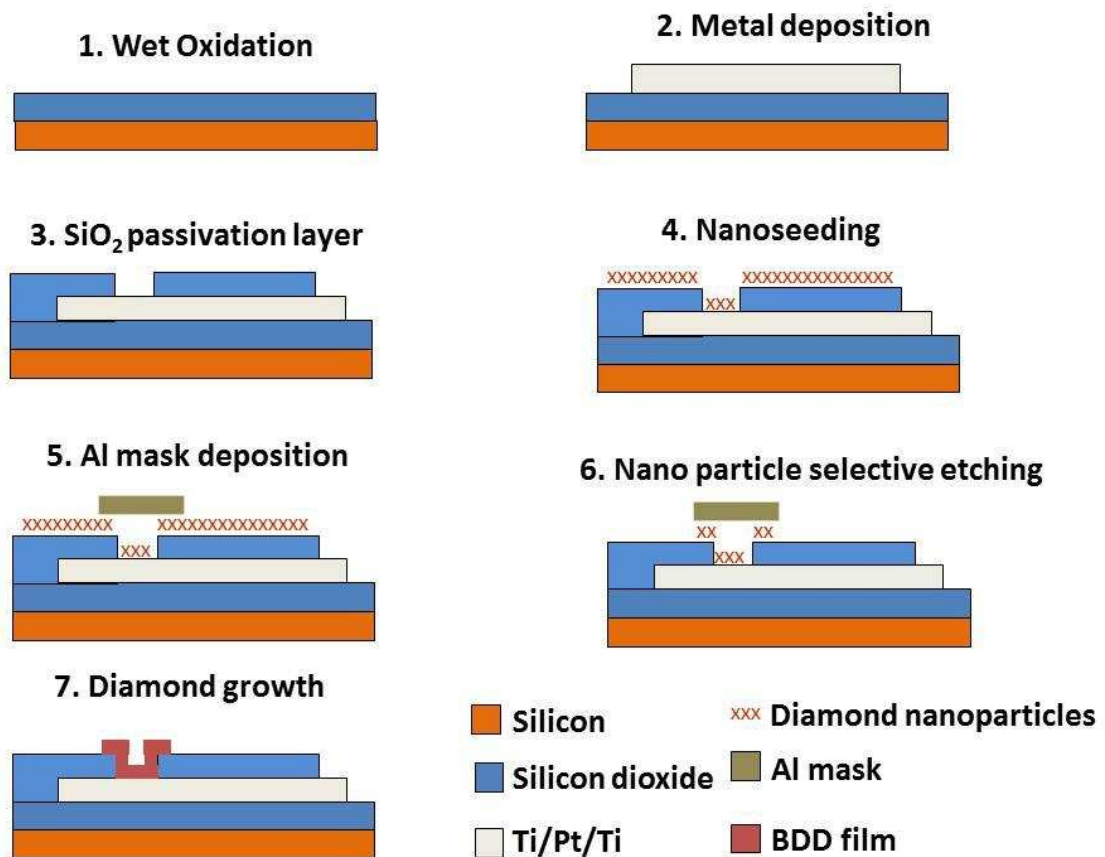


Figure 3.1 Schematics of diamond microelectrode fabrication process (Design 1)

Figure 3.2 a shows the SEM image of an ultramicroelectrode and 3.2 b that of a macroelectrode. In both cases diamond film was grown over titanium film. Non-continuous

diamond layers with impurities and pinholes are visible on diamond layer in both macro and micro-electrodes. Diamond deposition is influenced negatively as titanium shows an interaction with the carbon of the gas phase.²⁰ As a result diamond nucleation is delayed and the adhesion of the formed layers is poor, which is partly due to the occurring deformation of the substrates but also to the different thermal expansion coefficients of the different materials. The delay in diamond nucleation might be due to TiC formation. Diamond can nucleate only after saturation of surface and when TiC layer has attained certain thickness. The TiC layer is rough and porous and tends to split off easily.

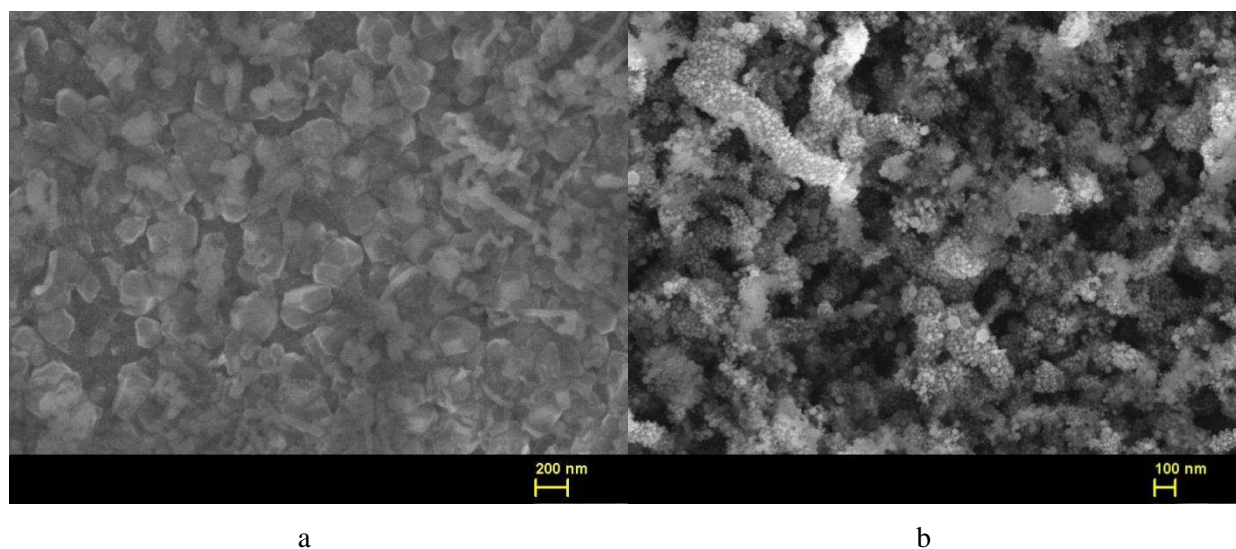


Figure 3.2 SEM images of BDD films grown over titanium: (a) microelectrode, (b) macroelectrode.

The electrochemical characterization techniques are described in detail in chapter 1 (section 1.4) and 3 (section 3.3). Cyclic voltammogram of the microelectrodes were recorded in 0.5 M aqueous LiClO_4 solution and all the electrodes exhibited an electrochemical window less than 3 V. Figure 3.3 a shows voltammogram of one microelectrode in a 64 channel MEA (20 μm in diameter) at $200 \text{ mV}\cdot\text{s}^{-1}$. The reason for the reduced window (compared to 3.4 V of BDD) might be due to pinholes in the diamond layer so that the titanium tracks were in contact with the electrolyte (as seen in SEM images – figure 3.2 a). Also the double layer capacitance C_D calculated (4 nF) at this scan rate was few orders of magnitude higher than that of diamond. It was observed that there was interconnection between different electrodes with a resistance as low as few kilo ohms between 2 electrodes. The steady limiting current (in $1\text{mM Fe}(\text{CN})_6^{4-}$ in 0.5 M KCl solution at $100 \text{ mV}\cdot\text{s}^{-1}$) was observed to be 160 nA (against theoretical value of 2.6 nA).

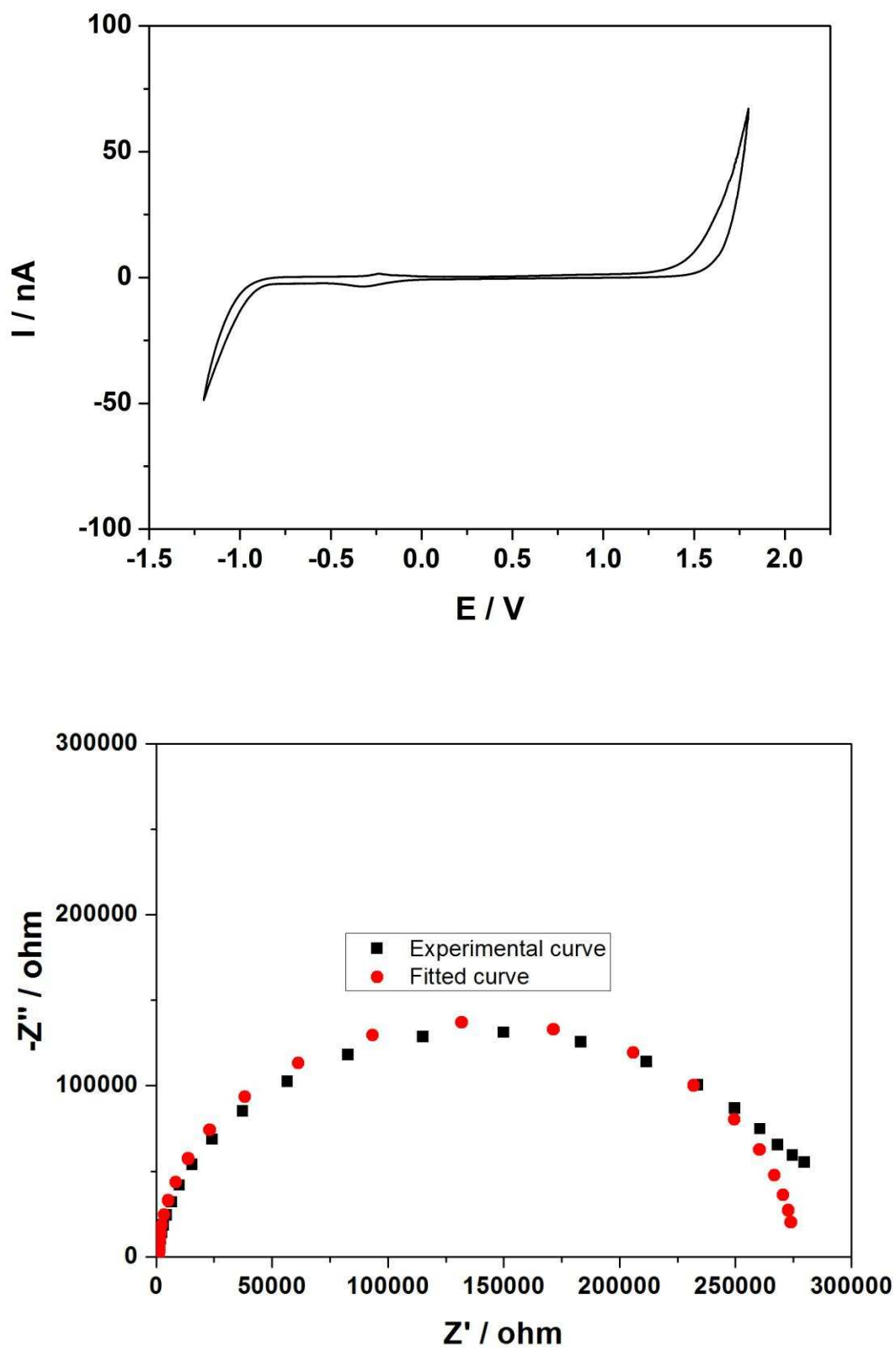


Figure 3.3 (a) Potential window observed by cyclic voltammetry (scan rate= $200 \text{ mV}\cdot\text{s}^{-1}$) in 0.5 M aqueous LiClO_4 solution and (b) Nyquist plot (experimental data and fitted data) of an ultramicroelectrode of diameter $20 \mu\text{m}$

The electron transfer rate k_0 and C_D estimated from Nyquist plots (figure 3.3 b) were $0.005 \text{ cm}\cdot\text{s}^{-1}$ and 1.5 nF . These results suggest that there is an interconnection between different electrodes and the interconnection might have arisen due to change in surface conductivity of oxide layer in hydrogen/methane/TMB plasma.²¹ Pinholes in diamond film reduced electrochemical window and electrode short circuit led us to redesign the complete technological process. Diamond films were grown at more than $650 \text{ }^\circ\text{C}$ and this high temperature might influence the physical and chemical properties of other layers (metallic and dielectric). In design 2 diamond, being very robust material was grown first followed by other layers.

3.1.2 Design 2

The process flow of design 2 is similar to design 1 (section 3.1.1). Silicon dioxide layer was grown on 4 inch silicon wafers by wet oxidation. After diamond nanoparticle fixation, an aluminum hard mask was deposited over the electrode areas by photolithography and the diamond nanoparticles outside these protected areas were etched away using ultra short RIE under oxygen plasma. The metal hard mask was then chemically removed to reveal the diamond nanoparticles patterns, on which diamond electrodes were grown in the SEKI diamond growth reactor. The fabricated diamond electrodes, typically, exhibit a thickness of approximately 300 nm over 200 micrometers in diameter. The electrodes were then individually contacted from the top by the deposition of Ti (50 nm) /Pt (150 nm) metal tracks using the lift-off process and Clariant Nlof 2020 as photoresist material. Contact on the electrodes was achieved by deposition of a metal ring across the edges of the electrodes. Finally a 600 nm thick silicon nitride (Si_3N_4) layer was deposited by CVD onto the substrate in order to isolate the metal tracks from the electrolyte solution. Several insulating passivation layers were tested including photo-resist SU-8, silicon oxide etc., but leakage capacitive and/or faradic current were observed. Si_3N_4 , having almost twice the dielectric constant of SiO_2 , was chosen as the passivation layer because of lower leakage current and high resistance to oxidation.²² Openings of the contact areas and of the diamond electrodes were achieved using local etching of the Si_3N_4 layer by RIE with SF_6 gas. It is this process step that determined the final diameter of each individual diamond electrode. Finally the photoresist used to selectively etch the nitride layer was removed and the UMEA was diced using a diamond saw. The detailed fabrication process according to design 2 is depicted in Figure 3.4. The samples were then cleaned in piranha solution (mixture of 3:1 concentrated sulfuric acid

to 30% hydrogen peroxide) for 10 minutes and was exposed to hydrogen plasma to hydrogen terminate the BDD films.

Several UMEs (strip electrodes and multi-electrode arrays) with diameters varying from 2 μm to 100 μm have been fabricated using this technique. Most of these electrodes exhibited typical BDD responses. The complete characterization of one such 8x8 diamond UMEAs with diamond electrodes of 14 μm in diameter and 100 μm of inter-electrode pitch is discussed in detail in section 3.2 and 3.3.

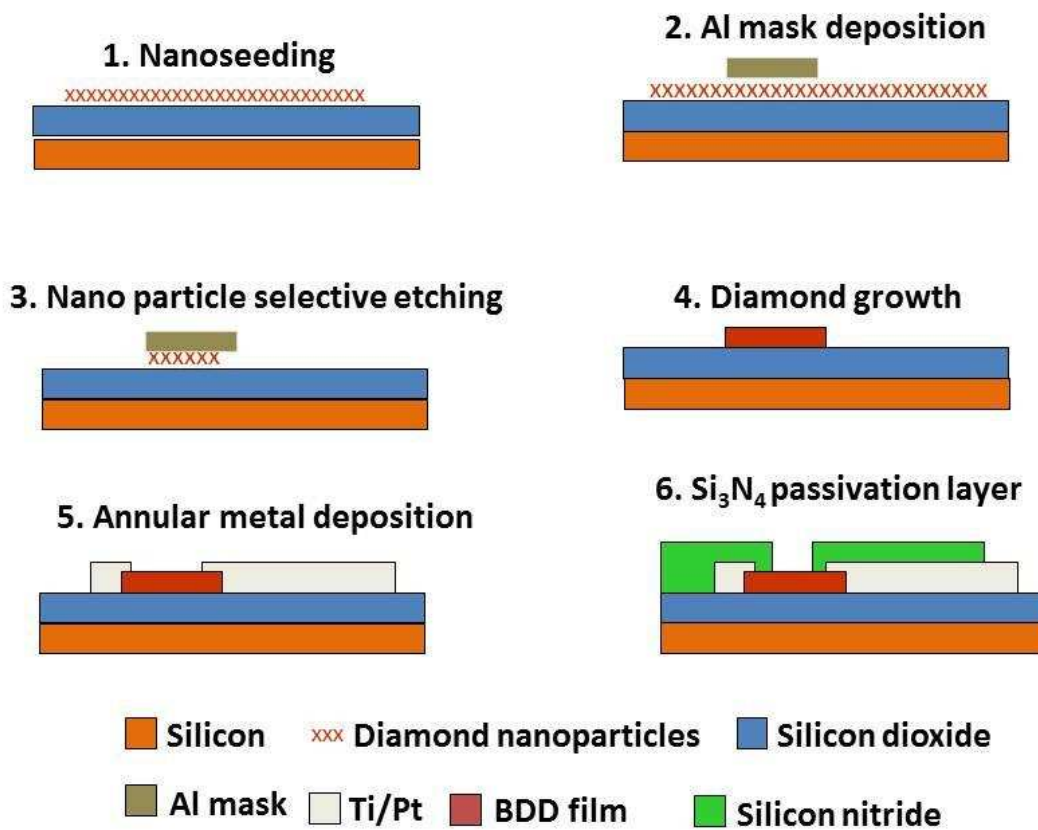


Figure 3.4 Schematics of diamond microelectrode fabrication process (design 2)

3.2 SEM Characterization

Figure 3.5 a shows the SEM image of 8x8 UMEA along with the tracks, where one can observe that each electrode is well separated (100 μm pitch). The diamond crystals are highly faceted with an average grain size of 100 nm as seen in Figure 3.5 d at higher magnification. Here neither major cracks nor pin-holes were visible, under SEM or optical microscopy, nor

on the tracks, nor on the passivation layer nor on the electrode surface as seen in Figures 3.5 b and 3.5 c. The electrode surface appears bright under SEM owing to the fact that the surface is conductive in steady state with respect to the outer passivation. In fact the observed surface conductivity may be associated to the hydrogen (H) termination of the electrode surface just after growth. A negative electron affinity is generated on the H terminated surface which increases the density of the back scattered electron.²³ The electron affinity of an H terminated diamond surface can go up to -1.3 eV.^{23,24} When compared to design 1, we get a polycrystalline film.

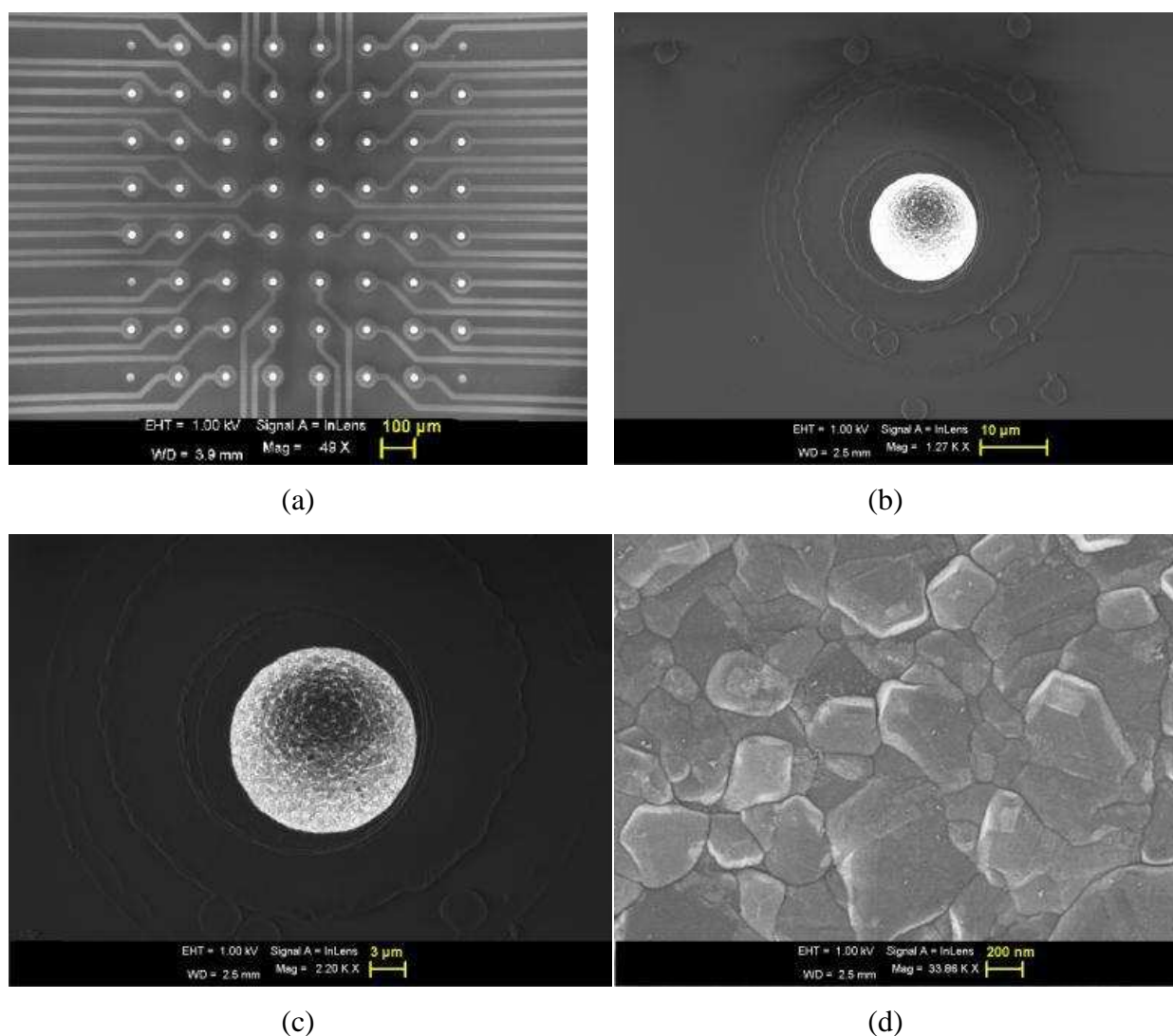


Figure 3.5 SEM image of an 8x8 UMEA along with the tracks (a) and magnified SEM image of a single electrode (b, c and d).

3.3 Electrochemical characterization

We have used electrochemical (EC) characterization techniques such as cyclic voltammetry (CV) and electrochemical impedance spectroscopy (EIS) to appreciate the electrodes performances namely their limiting currents (i_{lim}), electron transfer rates (k_0), electrochemical windows and background currents (i_{BG}) etc. They are the most efficient techniques to detect any cracks, passivation films, surface contamination or discontinuity of the insulating layer and analyzing EC properties of individual BDD UMEs.

3.3.1 Background current

CV was recorded on all the electrodes in 0.5 M aqueous LiClO_4 solution to ascertain the accessible EC window. Most of the electrodes exhibit a typical BDD window of over 3 V (in aqueous solution). CV of one such electrode is shown in Figure 3.6 where the electrode was scanned at $200 \text{ mV}\cdot\text{s}^{-1}$ (details of experimental procedures are described in chapter 1 section 1.4.2).

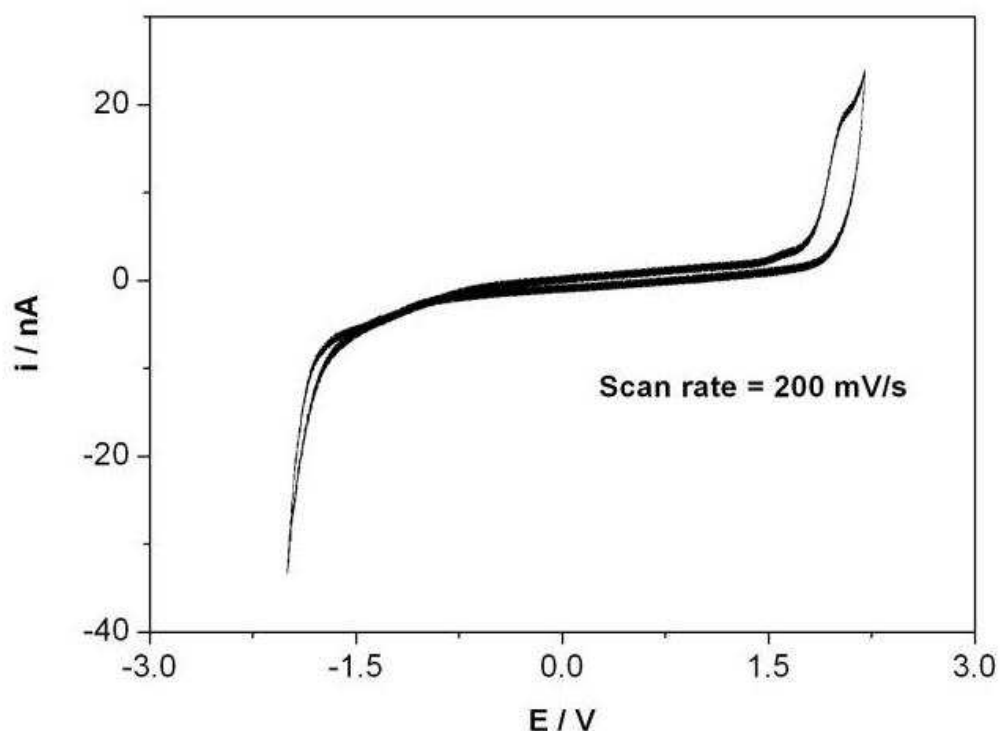


Figure 3.6 Typical potential window observed by cyclic voltammetry (scan rate= $200 \text{ mV}\cdot\text{s}^{-1}$) in LiClO_4 solution where i is the current in nA and E is the voltage in volts versus an Ag/AgCl reference electrode.

One unexpected characteristic appeared on this first prototype, as few electrodes exhibited a reduced potential window with a value typically equal to that of platinum electrodes. For this reason it was chosen not to assess further those electrodes and they hence appear as white spots on figures (3.7, 3.9 and 3.12), although of course they could be fully characterized but not relevant with the properties of diamond. This was associated with cracks or pinholes in the passivation layer so that the platinum tracks were in contact with the electrolyte. This, although, not observed with imaging techniques becomes easily identified with EC characterization. Other technique to detect the cracks or pinholes is fluorescence confocal laser scanning microscopy as demonstrated by Rudd et al. on platinum UMEA.²⁵

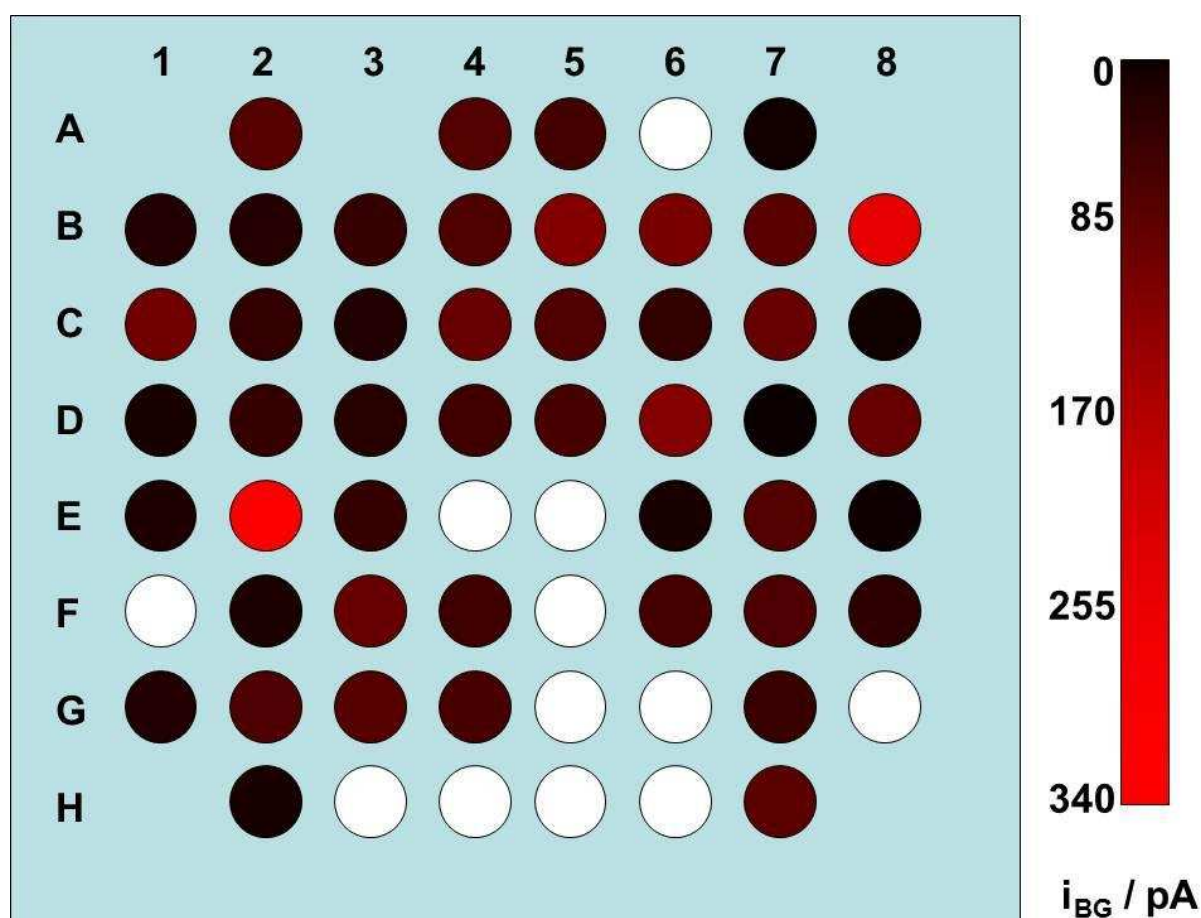


Figure 3.7 RGB model of an 8x8 electrode array where each electrode is represented by a spot and the red component value corresponds to their respective i_{BG} value. (In this first prototype, and although measurable, white spots correspond to electrodes that were not exhibiting the EC window of diamond, as attributed to Pt shorts from leaky tracks, thus not relevant for the comparison).

During CV characterization of each electrode, a transient current flows within the potential window when the potential is varied, as ions move to the surface forming a double layer.²⁶ The charging and discharging of this double layer constitutes the background current within the potential window. The background current i_{BG} was calculated for the electrodes of the array and was observed to be 94 ± 65 pA at a scan rate of $200 \text{ mV} \cdot \text{s}^{-1}$. i_{BG} of the 8×8 matrix is depicted in figure 3.7. RGB color model was used to indicate the amplitude of i_{BG} of each electrode. The green and blue color component has a value = 0 and red component vary from 0 to 255 corresponding to the amplitude of i_{BG} . The darker the spot, the lower the background current.

3.3.2 Steady state limiting current

Ideally, the limiting current of a UME is independent of the scan rate.^{27,28} The radial diffusion behavior of the UME enhances the mass transfer thus promoting steady-state electrochemical compartment. Hence, these microelectrodes exhibit typical sigmoidal shape in CV with a small hysteresis coming from double layer capacitance. On the other hand a macro-electrode shows a peak and the value of the peak current is directly proportional to the square root of the scan rate as the planar diffusion behavior limits the current.

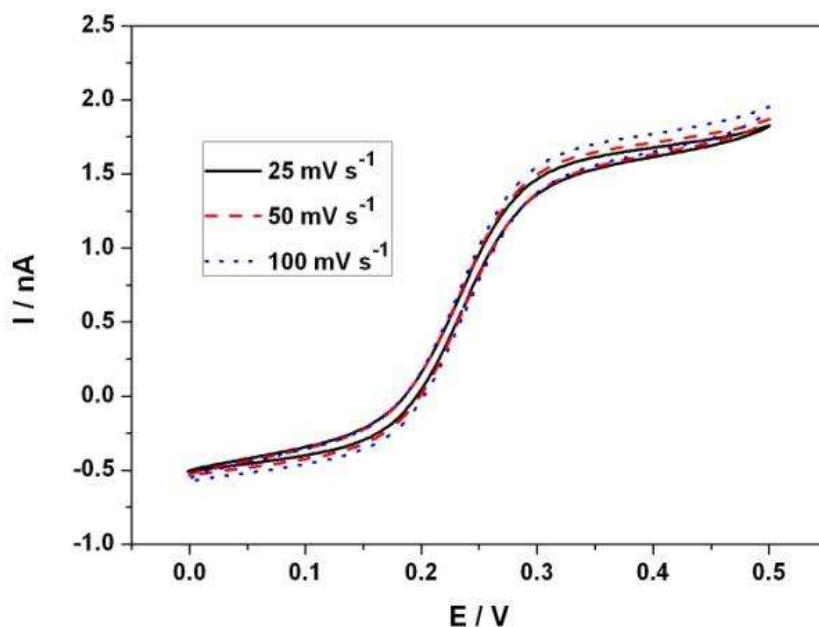


Figure 3.8 Cyclic voltammogram of an electrode at 25, 50 and $100 \text{ mV} \cdot \text{s}^{-1}$ in 0.5 M KCl aqueous solution containing $1 \text{ mM Fe(CN)}_6^{4-}$ ion.

Steady state voltammograms were recorded using CV in 1mM $\text{Fe}(\text{CN})_6^{4-}$ in 0.5 M KCl solution at $100 \text{ mV}\cdot\text{s}^{-1}$. The limiting current i_{lim} of the 8x8 matrix was recorded and the average limiting current value was of $1.83\pm 0.2 \text{ nA}$ as opposed to theoretical limiting current of 1.8 nA (Diffusion coefficient of ferrocyanide = $6.67 \times 10^{-6} \text{ cm}^2 \text{ s}^{-1}$ ²⁹). Furthermore they varied from electrode to electrode with a standard deviation of 190 pA (Table 3.1).

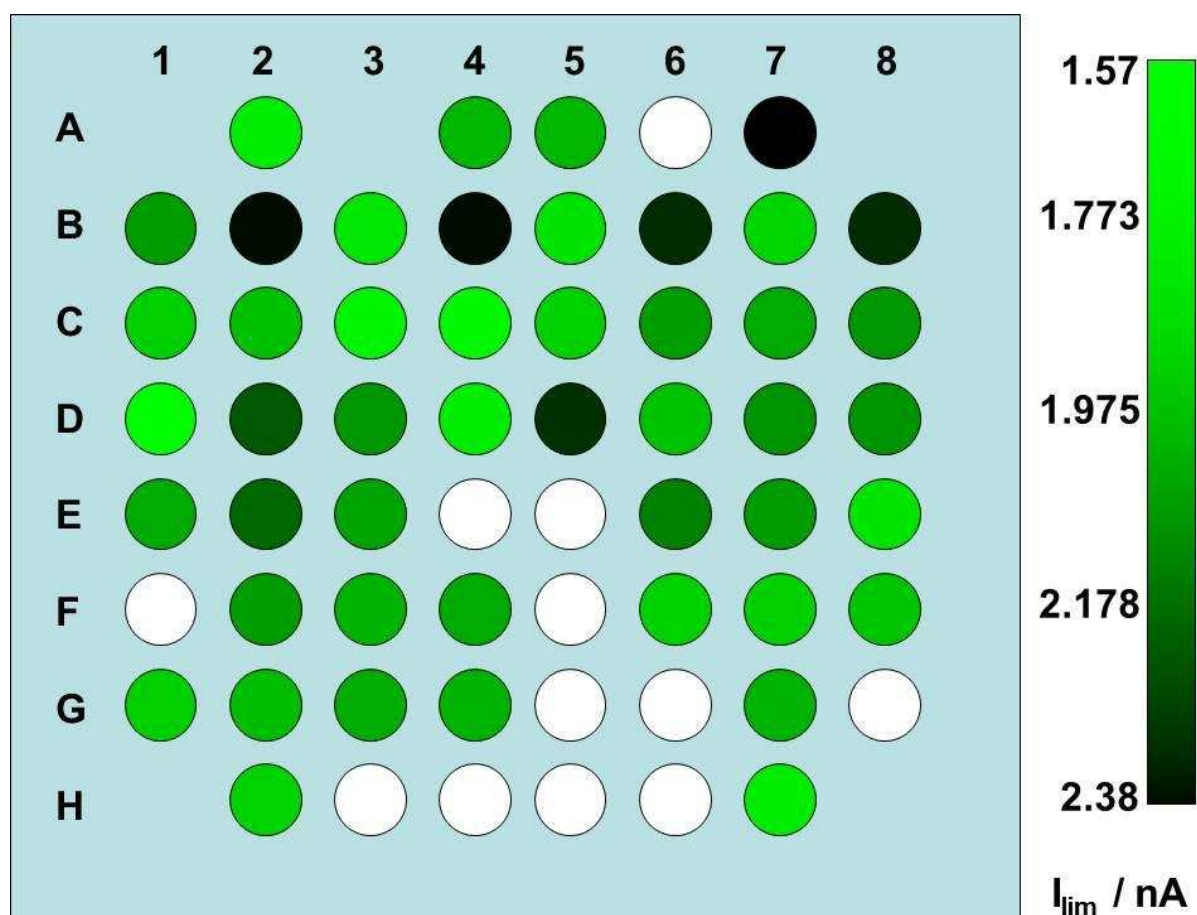


Figure 3.9 RGB model of an 8x8 electrode array where each electrode is represented by a circle and the green component value is inversely proportional to respective i_{lim} value.

Figure 3.8 shows CV of an electrode at various scan rates. When the diffusion layer d is greater than the electrode radius r , radial diffusion predominates and if $r \gg d$, planar diffusion predominates, where ‘ t ’ is the duration of experiment (refer to chapter 1 section 1.6). At slower scan rates of $25, 50$ and $100 \text{ mV}\cdot\text{s}^{-1}$ the diffusion layer thickness $d \gg$ radius r of the electrode and hence radial diffusion predominates and as a result a sigmoidal voltammogram is observed. i_{lim} observed was 1.6 nA and 1.66 nA at $25 \text{ mV}\cdot\text{s}^{-1}$ and $100 \text{ mV}\cdot\text{s}^{-1}$.

¹, respectively. Although a slight deviation from the ideal scan rate independent behavior was observed, the current density variation is negligible (below 4%) when compared to a macro-electrode at these scan rates.

Figure 3.9 represents an RGB color model indicating the value of i_{lim} of each electrode where red and blue color component has a value = 0 and green component vary from 0 to 255 and is inversely proportional to the amplitude of i_{lim} .

3.3.3 Electrochemical impedance spectroscopy

The Nyquist plots obtained from EIS of the UMEA were used to calculate the k_0 of each electrode. Electrochemical interfaces can be classically modeled by the Randles equivalent electric circuit. The latter consists of 4 electronic components: R_S the electrolytic resistance, R_T the charge transfer resistance, C_D the double layer capacitance and Z_W the Warburg element. The diameter of the semi-circle portion corresponds to the transfer resistance.^{30,31}

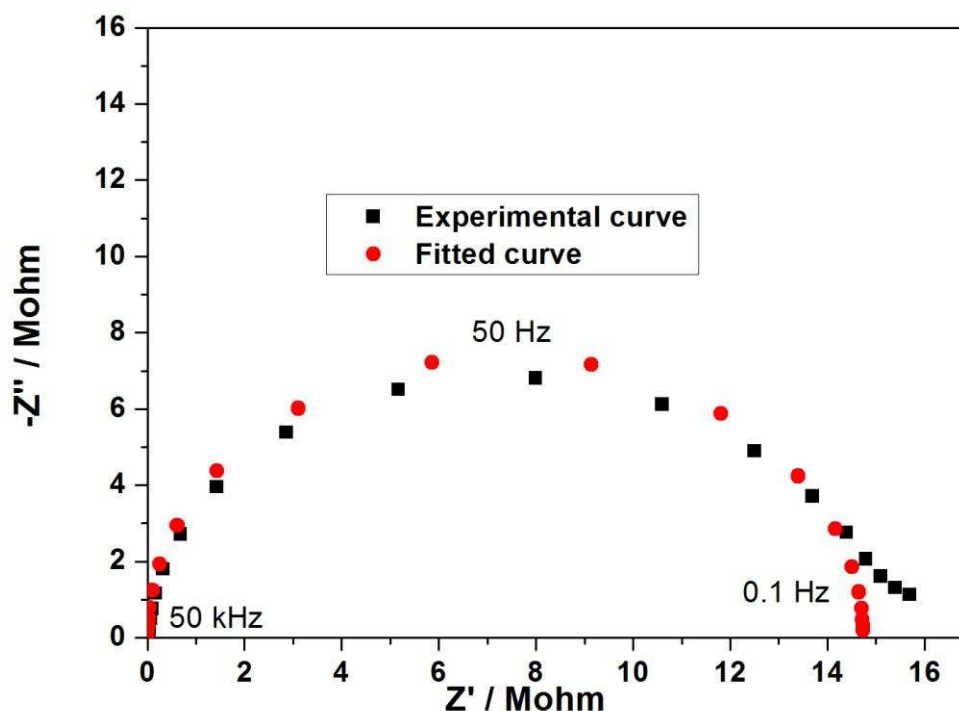


Figure 3.10 Nyquist plot (experimental data and fitted data) of an ultramicroelectrode.

From the Nyquist plot of all those electrodes, as exemplified in figure 3.10, it was observed that the straight line (Warburg element) almost disappeared since the linear correlation of $\text{Re}(Z)$ vs $-\text{Im}(Z)$ corresponds to a linear semi-infinite diffusion process (transient mass transfer).³² Elsewhere, the semi-circular shape of the spectrum is not depressed thus highlighting the pure capacitive behavior of the interface. The rate of mass transport to and from the electrode is greater in UMEs when compared to macro-electrodes. Hence the Randles circuit of a UME gets modified to a 3 impedance component (R_S , R_T and C_D , the Warburg diffusion impedance being deleted– refer figure 3.11).

An R(CR) model circuit was used to fit the experimental curves and the impedance value obtained for R_S , R_T and C_D were 414 ohm, 14.7 Mohm and 132 pF respectively. The χ^2 error was suitably low ($\chi^2 < 10^{-4}$), and the error associated with each element was below 5%. The electron transfer rate of this electrode was calculated to be 0.012 cm s^{-1} . The semicircle impedance spectra could also favorably be used for bio-sensing applications where one can observe the change in the k_0 value.³⁰ The electrode electron transfer rate k_0 is calculated using equation (1.1) and variation of k_0 along the electrodes in the chip is shown in Figure 3.12. The average value obtained for k_0 is of 0.013 cm s^{-1} which is close to the values reported by other groups for an H terminated BDD electrode.³³⁻³⁵ The mean values and standard deviations of i_{BG} , i_{lim} , and k_0 are summarized in table 3.1.

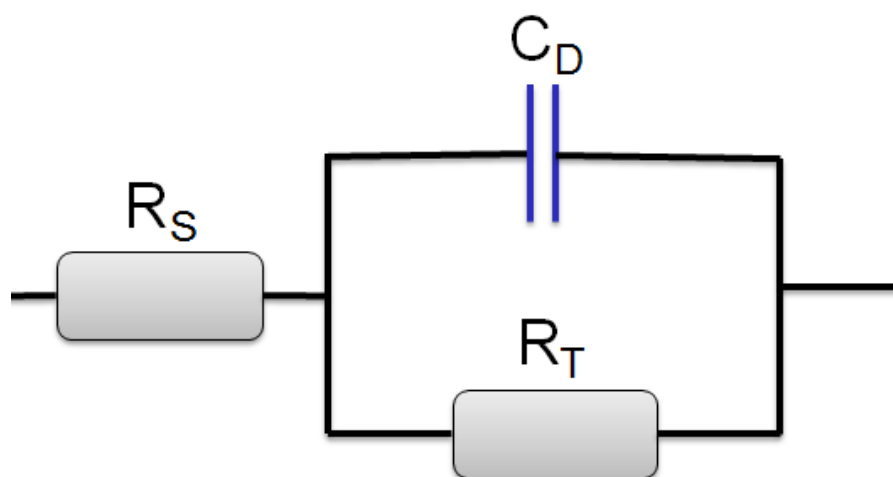


Figure 3.11 3 Component of Randles's circuit of ultramicroelectrode where R_S is the electrolytic resistance, R_T is the charge transfer resistance and C_D is the double layer capacitance.

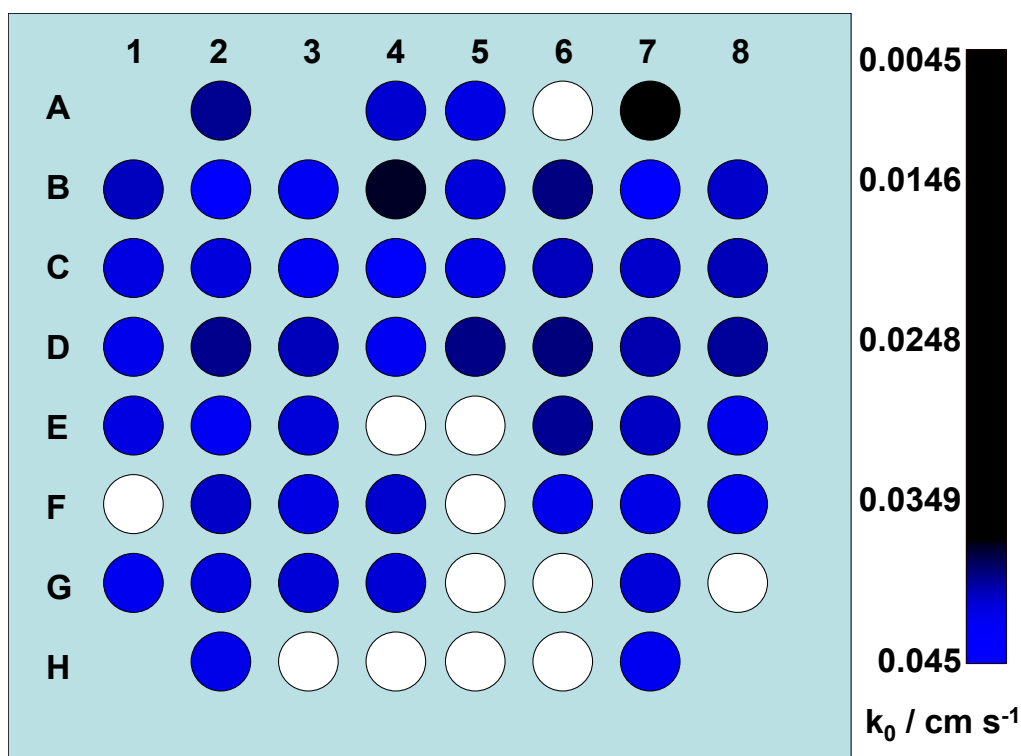


Figure 3.12 RGB model of an 8x8 electrode array where each electrode is represented by a circle and the blue component value corresponds to their respective k_0 value.

Table 3.1 Mean value and standard deviation of the background current i_{BG} , limiting current i_{lim} , and transfer rate k_0 .

Parameters	Mean value	Standard deviation
i_{BG}	94.33 pA	64.85 pA
i_{lim}	1.83 nA	0.19 nA
k_0	0.0132 cm.s^{-1}	0.008 cm.s^{-1}

The electron transfer rate of the electrodes was further enhanced by applying the electrochemical treatment mentioned in chapter 2. A train of 50 current pulses of alternating amplitude (10 mA.cm^{-2} and -10 mA.cm^{-2}) and of equal duration (100 ms) was applied between each working microelectrode and the counter electrode in 0.5 M aqueous LiClO_4 solution (standard activation protocol). After this treatment the k_0 values of the electrodes have increased by several folds and i_{lim} measured was close to theoretical values (1.8 nA). The EC treatment cleans the electrode surface further and hence improves the reactivity of the electrodes.

It has been observed that the values of k_0 , i_{lim} , C_D and i_{BG} were somehow related to each other for different electrodes. The variation of these values from electrode to electrode cannot be explained by conventional EC and SEM characterization. These variations might be due to difference in intrinsic conductivity, crystalline orientation and/or charge transfer constant of individual grains. This could be associated with varying boron intake, even at high boron concentrations, leading to varying electrical and electrochemical characteristics of diamond grains. So, comparing the grain and the microelectrode sizes, conversely to macro-electrodes, this grain distribution may statically markedly vary between each electrode and thus strongly affect their electrochemical behavior.

A comparison is made to correlate different parameters such as the k_0 , i_{lim} , C_D and i_{BG} of 2 electrodes and is summarized in table 3.2. The k_0 and C_D values were obtained from Nyquist plots.

The background current (which is attributed by the double layer capacitance) is higher when C_D is higher since capacitive current represent the main background contribution owing to the weak charge transfer associated to media hydrolysis. However, the difference in the values of double layer capacitance measured using EIS and CV is 49% and 21% for electrode 1 and 2 respectively. This difference is coherent, since CV measurements are less sensitive to the capacitive behavior (which is dominated by the faradic response) and just allow estimating the order of magnitude of the capacitance.

From the limit current recording from CV curves, one can estimate the effective surface area of the electrode, assuming a purely Nernstian electrochemical behavior (large charge transfer rate). Typically, this effective surface area depends up on the roughness of the electrode but also on the ability of the electrode toward charge transfer. Indeed, limiting current and effective surface (due to their proportional relationship) vary much less than the measured k_0 . Such a divergence can be explained through one fundamental aspects: first the limiting current is measured in the diffusion limitation part of the CV (e.g. the plateau, at high over potential) whereas k_0 is calculated from the EIS spectrum obtained at the half-wave potential of the redox couple under a charge limitation behavior. Thereby, such differences in the variations of the limiting current and on the k_0 clearly highlight the heterogeneities of the charge transfer resistance over the electrode surface and thus the accentuated and discretized role of the grain distribution on microelectrode behavior.

Table 3.2 Comparison of different parameters such as the electron transfer rate k_0 , limiting current i_{lim} , double layer capacitance C_D and background current i_{BG} of 2 electrodes.

Parameters	Electrode 1	Electrode 2	Difference % $\Delta x/x_1$
k_0 (cm s ⁻¹)	0.012	0.017	42
i_{lim} (nA)	1.74	1.76	11.5
C_D (pF)	132	197	49
i_{BG} at 200 mV.s ⁻¹ (pA)	63	76	21

3.4 All diamond microelectrode arrays

One of the disadvantages of individual microelectrodes is relative reduced currents they can drive (pico to nanoamperes), due to their small surface area.³⁶ Hence a noise canceller or signal amplifier has to be included to enhance the quality of the electrochemical recordings. To overcome this problem we have designed interconnected BDD microelectrode arrays using intrinsic diamond as the passivation layer. In theory, the microelectrode arrays behave as an independent microelectrode as their diffusional fields do not overlap at suitable scan rate.¹¹ In an interconnected MEA, the overall output of the current is the sum of the steady-state redox currents on individual electrodes of the array.

Figure 3.13 summarizes the complete fabrication process. The technological processes are similar to design 1 and 2. Silicon wafers were nanoseeded with diamond nanoparticles and BDD films were grown in the SEKI MPECVD diamond growth reactor with TMB gas (refer to chapter 1 section 1.3). The BDD film has a thickness of approximately 300 nm. Chromium mask was deposited on BDD layer with Si₃N₄ as the sacrificial layer. Intrinsic diamond was grown on top of this layer (growth conditions were similar to that of boron doped diamond except from the absence of TMB doping gas, in a twin SEKI 6500 4 inch reactor –“THOR” that was never exposed to doping gases). The intrinsic diamond film has a thickness of 800 nm. Finally the chromium mask was etched to expose the conductive BDD film. The samples were then cleaned in piranha solution for 10 minutes and exposed to hydrogen plasma to hydrogen terminate the BDD films. Each chip had a total of 58 microelectrodes of 17 μm in diameter. Hence the total surface area of BDD film in contact with the electrolyte is 0.000132 cm². The inter-electrode distance is 60 μm. Figure 3.14 shows the SEM images of the MEA.

The darker area (figure 3.14 a) is the intrinsic diamond and the lighter area is the boron doped diamond. One can observe that there is clear-cut boundary between the doped and intrinsic diamond which shows that there is no boron diffusion across the interface.

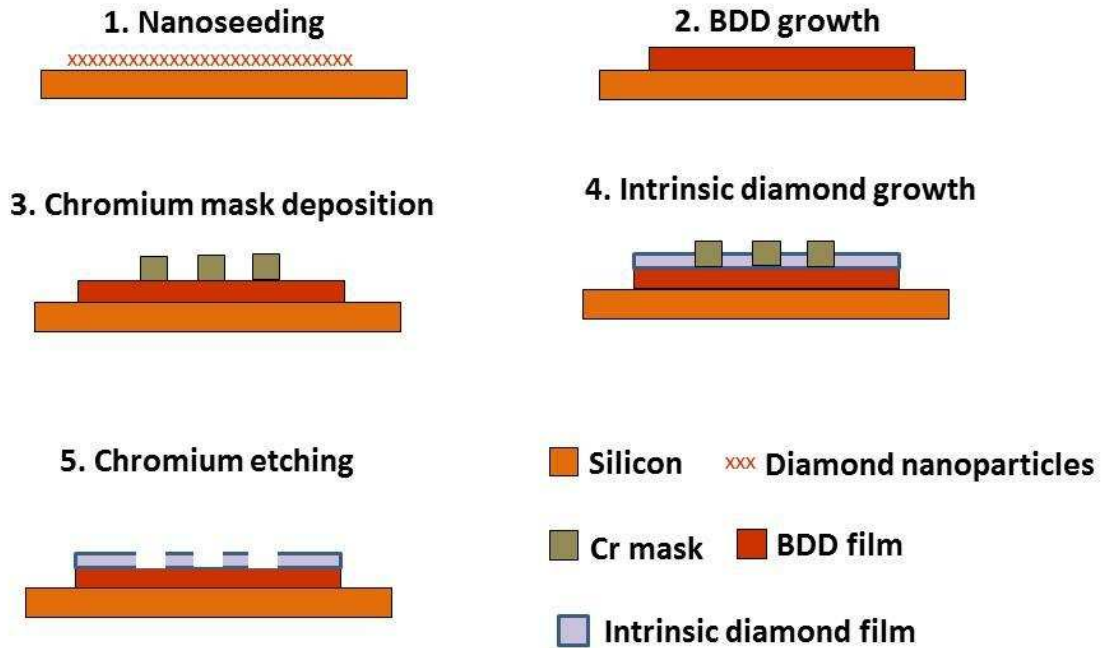


Figure 3.13 Schematics of interconnected diamond microelectrode array fabrication process.

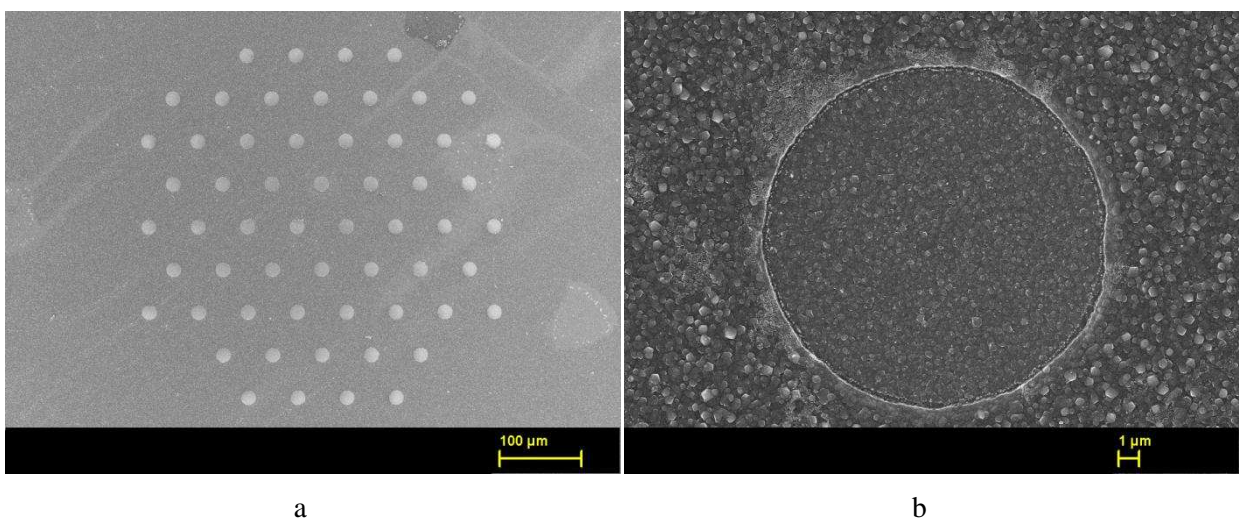


Figure 3.14 SEM images of MEA and individual BDD conducting electrode at 17 μm in diameter

The fabricated electrodes were characterized by EIS and CV to evaluate their electrochemical properties (refer to section 3.3 for more details). The CV in 0.5 M aqueous LiClO₄ solution demonstrated a large potential window greater than 3 V (figure 3.15) and a double layer capacitance of 345 nF (2.62 mF.cm⁻²) measured at scan rate of 100 mV.s⁻¹. The electron transfer rate k_0 and C_D estimated from Nyquist plot were 0.56 cm.s⁻¹ and 227 nF (1.73 mF.cm⁻²). Figure 3.16 shows the CV of MEA in 1 mM Fe(CN)₆^{3-/4-} in 0.5 M aqueous KCl solution at different scan rates: 10, 25, 50, 100, 200, 500, 1000 and 2000 mV.s⁻¹. The shape of the CV of the MEA depends on two parameters: thickness of the diffusion layer (depends on the scan rate and potential window) and the inter-electrode distance (that has to be chosen to avoid any coverage of the hemispherical diffusion profiles arising from each microelectrode). It is observed from figure 3.16 that for most of the scans (scan rate < 500 mV.s⁻¹) exhibited an electrochemical behavior similar to that of a macro-electrode. The diffusion layer of each microelectrode converges over each other to form a continuous diffusion layer. At higher scan rates, the CV is similar to that of steady-state voltammograms. The steady state limiting current of the MEA being equal to the sum of the limiting currents of the entire individual electrode, it should in theory reach 127 nA (equation 1.9). The limiting current extracted for Fe(CN)₆⁴⁻ oxidation at 500 mV.s⁻¹ from figure 3.16 is 22 μA. The peak current i_p for Fe(CN)₆⁴⁻ oxidation at 10 mV.s⁻¹ can be calculated from the following equation of a macroelectrode is 9.1 nA:

$$i_p = 2.69 \times 10^5 n^{3/2} A C_0 D^{1/2} v^{1/2} \quad (2.1)$$

Where D_0 is the diffusion coefficient, C_0 the concentration, and n the number of electrons transferred per molecule of reactant, A the total surface area and v the scan rate. The value of the peak current observed from figure 3.16 at this scan rate is 12.8 μA.

For an electrode of 17 μm in diameter the diffusion layer thickness (equation 1.5) d is 26.33 μm at 25 mV.s⁻¹ scan rate and the MEA should exhibit sigmoidal voltammogram behavior from this scan rate onwards. The high double layer capacitance, electron transfer rate and steady state limiting current suggest that the electron transfer is not only the result of the 58 electrodes but also from the intrinsic diamond which serves as the passivation layer. As the MEA is fabricated under hydrogen plasma, the H-terminated intrinsic (undoped) diamond when immersed in redox electrolyte solutions shows reversible insulator - metal transitions³⁷. The hydrogen induced surface conductivity is due to a doping mechanism where the surface adsorbates act as acceptors.³⁸ The surface acceptors can be solvated ionic species that undergo

electrochemical reactions after accepting an electron from the diamond valence band. This increases of the overall active surface area could be attributed to the high electron transfer rate and limiting current. This problem can be eliminated by selective O-termination of the intrinsic layer.

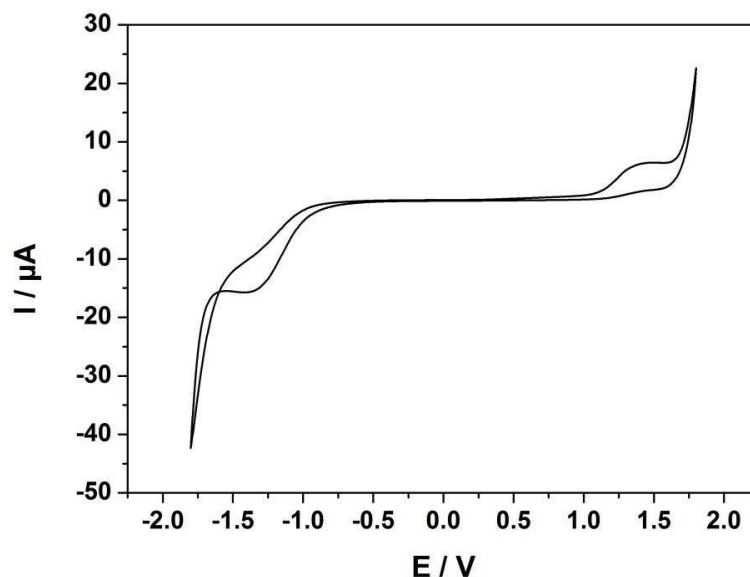


Figure 3.15 Cyclic voltammograms of boron doped diamond MEA in 0.5 M aqueous LiClO_4 solution.

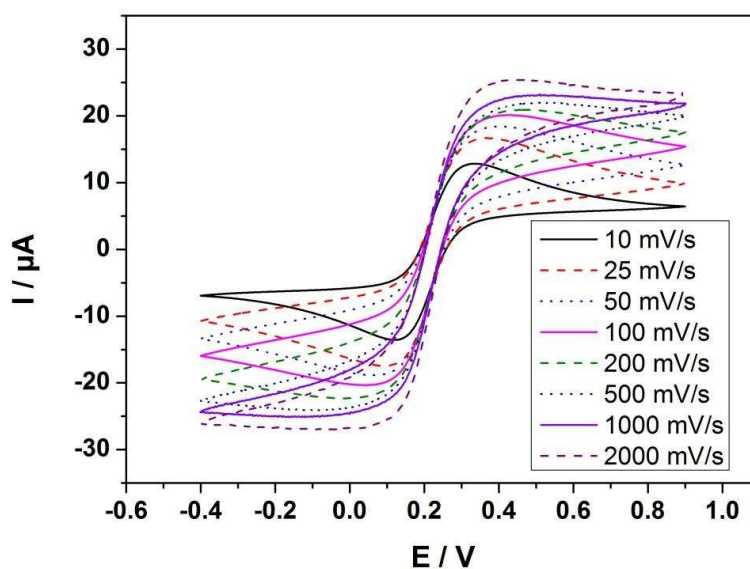


Figure 3.16 Cyclic voltammograms of boron doped diamond MEA in 0.5 M aqueous KCl solution containing 1 mM $\text{Fe}(\text{CN})_6^{3-/4-}$ at scan rate $10 \text{ mV}\cdot\text{s}^{-1}$ to $2 \text{ V}\cdot\text{s}^{-1}$.

Conclusions

A novel, high yield and reproducible lithographic process has been used to fabricate the UMEAs. BDD UMEAs suitable for use in electrochemical sensors were prepared by micro-fabrication technique compatible with standard clean room technology. Topographical characterization and detailed electrochemical study of individual UMEs revealed only few faulty electrodes within an array. In electrochemical tests, the UMEs exhibited low background currents, almost theoretical steady state limiting currents and fast electron transfer rates (close to 0.01 cm s^{-1}). Further improvement in these two values was achieved through EC activation. The long term goal of this work was ultimately to develop biosensing platforms for the monitoring of neural activities for electrophysiology. Electro-analytical and electrophysiological applications of those microelectrodes and MEA platforms are mentioned in detail in chapter 4 and 5.

Bibliography

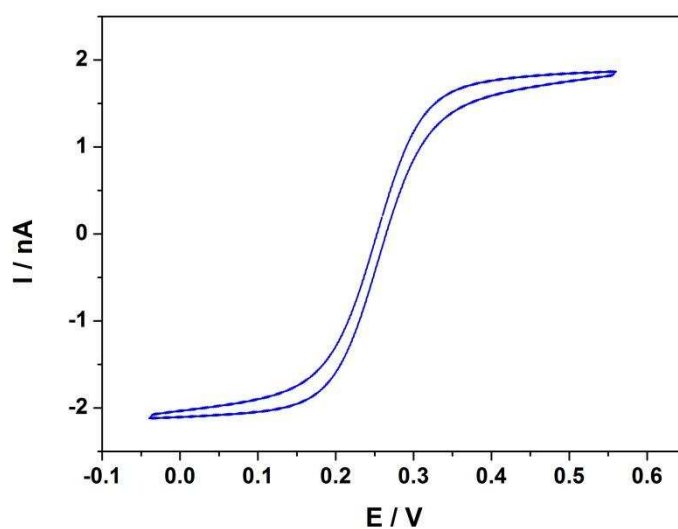
- (1) Thiébaud, P.; Beuret, C.; Koudelka-Hep, M.; Bove, M.; Martinoia, S.; Grattarola, M.; Jahnsen, H.; Rebaudo, R.; Balestrino, M.; Zimmer, J.; Dupont, Y. *Biosensors & bioelectronics* **1999**, 14, 61–65.
- (2) Liu, S.; Chen, Y.; Fang, F.; Xu, J.; Sheng, G.; Yu, H.; Liu, G.; Tian, Y. *Environmental Science & Technology* **2009**, 43, 1160–1165.
- (3) Biran, R.; Martin, D. C.; Tresco, P. A. *Experimental neurology* **2005**, 195, 115–126.
- (4) Wang, K.; Fishman, H. A.; Dai, H.; Harris, J. S. *Nano letters* **2006**, 6, 2043–2048.
- (5) Abarrategi, A.; Gutiérrez, M. C.; Moreno-Vicente, C.; Hortigüela, M. J.; Ramos, V.; López-Lacomba, J. L.; Ferrer, M. L.; del Monte, F. *Biomaterials* **2008**, 29, 94–102.
- (6) Weiland, J. D.; Anderson, D. J.; Humayun, M. S. *IEEE transactions on bio-medical engineering* **2002**, 49, 1574–9.
- (7) Panizza, M.; Cerisola, G. *Electrochimica Acta* **2005**, 51, 191–199.
- (8) Yano, T.; Tryk, D. A.; Hashimoto, K.; Fujishima, A. *Journal of The Electrochemical Society* **1998**, 145, 1870–1876.
- (9) Swain, G. M. *Analytical chemistry* **1993**, 65, 345–351.
- (10) Soh, K. L.; Kang, W. P.; Davidson, J. L.; Basu, S.; Wong, Y. M.; Cliffel, D. E.; Bonds, A. B.; Swain, G. M. *Diamond and Related Materials* **2004**, 13, 2009–2015.
- (11) Lawrence, N. S.; Pagels, M.; Meredith, A.; Jones, T. G. J.; Hall, C. E.; Pickles, C. S. J.; Godfried, H. P.; Banks, C. E.; Compton, R. G.; Jiang, L. *Talanta* **2006**, 69, 829–834.
- (12) Tian, R.; Zhi, J. *Electrochemistry Communications* **2007**, 9, 1120–1126.
- (13) Pagels, M.; Hall, C. E.; Lawrence, N. S.; Meredith, A.; Jones, T. G. J.; Godfried, H. P.; Pickles, C. S. J.; Wilman, J.; Banks, C. E.; Compton, R. G.; Jiang, L. *Analytical chemistry* **2005**, 77, 3705–8.
- (14) Hess, A. E.; Sabens, D. M.; Martin, H. B.; Zorman, C. A.; Member, S. *Journal of microelectromechanical systems* **2011**, 20, 867–875.
- (15) Gao, Z.; Carabelli, V.; Carbone, E.; Colombo, E.; Dipalo, M.; Manfredotti, C.; Pasquarelli, A.; Feneberg, M.; Thonke, K.; Vittone, E.; Kohn, E. *Journal of Micro-Nano Mechatronics* **2011**, 6, 33–37.
- (16) Bongrain, A.; Scorsone, E.; Rousseau, L.; Lissorgues, G.; Gesset, C.; Saada, S.; Bergonzo, P. *Journal of Micromechanics and Microengineering* **2009**, 19, 074015.

- (17) Sreenivas, K.; Reaney, I.; Maeder, T.; Setter, N.; Jagadish, C.; Elliman, R. G. *Journal of Applied Physics* **1994**, 75, 232.
- (18) Scorsone, E.; Saada, S.; Arnault, J. C.; Bergonzo, P. *Journal of Applied Physics* **2009**, 106, 014908.
- (19) Bongrain, A.; Scorsone, E.; Rousseau, L.; Lissorgues, G.; Gesset, C.; Saada, S.; Bergonzo, P. *Journal of Micromechanics and Microengineering* **2009**, 19, 074015.
- (20) Gerger, I.; Haubner, R.; Kronberger, H.; Fafilek, G. *Diamond and Related Materials* **2004**, 13, 1062–1069.
- (21) Vande Voorde, P.; Cox, M.; Greene, W. *IEEE Electron Device Letters* **1998**, 19, 291–293.
- (22) Ma, T. P. *IEEE Transactions on Electron Devices* **1998**, 45, 680–690.
- (23) Nebel, C. E.; Shin, D.; Takeuchi, D.; Yamamoto, T.; Watanabe, H.; Nakamura, T. *Langmuir* **2006**, 22, 5645–5653.
- (24) Maier, F.; Riedel, M.; Mantel, B.; Ristein, J.; Ley, L. *Physical Review Letters* **2000**, 85, 3472–3475.
- (25) Rudd, N. C.; Cannan, S.; Bitziou, E.; Ciani, I.; Whitworth, A. L.; Unwin, P. R. *Analytical Chemistry* **2005**, 77, 6205–6217.
- (26) Qu, D.; Shi, H. *Journal of Power Sources* **1998**, 74, 99–107.
- (27) Colombo, E.; Men, Y.; Scharpf, J.; Pietzka, C.; Dipalo, M.; Herfurth, P.; Gao, Z.; Schneider, M.; Carabelli, V.; Carbone, E.; Kohn, E.; Pasquarelli, A. *Diamond and Related Materials* **2011**, 20, 793–797.
- (28) Caudill, W. L.; Howell, J. O.; Wightman, R. M. *Analytical Chemistry* **1982**, 2532–2535.
- (29) Konopka, S. J.; McDuffie, B. *Analytical Chemistry* **1970**, 42, 1741–1746.
- (30) Yun, Y.; Bange, A.; Heineman, W. R.; Halsall, H. B.; Shanov, V. N.; Dong, Z.; Pixley, S.; Behbehani, M.; Jazieh, A.; Tu, Y.; Wong, D. K. Y.; Battacharya, A.; Schulz, M. J. *Sensors and Actuators B: Chemical* **2007**, 123, 177–182.
- (31) Dumitrescu, I.; Unwin, P. R.; Macpherson, J. V. *Electrochemistry Communications* **2009**, 11, 2081–2084.
- (32) Siddiqui, S.; Arumugam, P. U.; Chen, H.; Li, J.; Meyyappan, M. *ACS Nano* **2010**, 4, 955–961.
- (33) Fischer, A. E.; Show, Y.; Swain, G. M. *Analytical Chemistry* **2004**, 76, 2553–2560.

- (34) Hupert, M.; Muck, A.; Wang, J.; Stotter, J.; Cvackova, Z.; Haymond, S.; Show, Y.; Swain, G. M. *Diamond and Related Materials* **2003**, 12, 1940–1949.
- (35) Granger, M. C.; Witek, M.; Xu, J.; Wang, J.; Hupert, M.; Hanks, A.; Koppang, M. D.; Butler, J. E.; Lucazeau, G.; Mermoux, M.; Strojek, J. W.; Swain, G. M. *Anal. Chem.* **2000**, 72, 3793–3804.
- (36) Hayashi, K.; Takahashi, J.; Horiuchi, T.; Iwasaki, Y.; Haga, T. *Journal of The Electrochemical Society* **2008**, 155, J240–J243.
- (37) Shin, D.; Watanabe, H.; Nebel, C. E. *Journal of the American Chemical Society* **2005**, 127, 11236–7.
- (38) Ristein, J. *Journal of Physics D: Applied Physics* **2006**, 39, R71–R81.

CHAPTER IV

Diamond microelectrodes: Electroanalytical application



Introduction

This chapter deals with an electro-analytical application of microelectrodes fabricated using the technology described in chapter 3: Quasi real time quantification of uric acid in human urine. Uric acid (UA) is the principal breakdown product of purine metabolism¹ and the normal UA concentration in human urine is around 2 mM.² Overconsumption of protein, overdrinking of alcoholic beverages, heavy stress and lack of exercise increases the amount of uric acid in blood serum.³ Hyperuricemia, associated with renal disease, can cause gout,⁴ cardiovascular diseases,⁵ kidney stones⁶ etc. whereas hypouricemia can be due to Fanconi syndrome,⁷ Nephritis⁸ and other kidney disorders. Hence it is important to monitor UA levels in bodily fluids such as blood and urine.

Nowadays, the determination of uric acid in urine is performed in medical laboratories using mainly spectrophotometric analysis methods. Other techniques reported in the literature include chromatographic methods, capillary electrophoresis and electrochemical (EC) methods.³ Enzyme-based quantification techniques are associated to oxidation of uric acid in the presence of uricase yielding allantoin, carbon dioxide and hydrogen peroxide. However there is also an interest in continuous monitoring of UA in urine, in particular for patients admitted in intensive care units (ICU), where the early diagnostic of acute renal failure (ARF) observed in up to 25% of the patients and it can have a major impact on the survival rate of those patients.⁹ In this context electrochemical detection techniques are seen as a promising alternative to conventional optical methods due to their good sensitivity, fast measuring time, portability, low power consumption and cost effectiveness, thus enabling direct bedside monitoring.

Various electrochemical approaches such as a polymer modified electrode,¹⁰⁻¹² a chemically modified electrode,¹³⁻¹⁶ an enzyme modified electrode,¹⁷ an electrochemical pre-treatment¹⁸ have been developed to detect UA. However UA coexists with ascorbic acid (AA) in biological fluids and has got nearly the same oxidation potential.¹¹ Although modified electrodes show good selectivity to UA, complications such as adsorption, fouling etc. are associated with those techniques.¹⁴ Simultaneous determination of dopamine, AA and UA were also investigated using fast cyclic voltammetry (CV) and differential pulse voltammetry (DPV) without any electrode modification.¹⁹ However, using this techniques, the analyte must be diluted to prevent the surface from fouling.

Popa et al. has achieved UA and AA peak separation by anodizing the diamond surface.² However, at high pH values the peak separation was diminished thus making UA quantification difficult in the presence of AA. Moreover, the analyte has to be diluted by several thousand fold to obtain reliable results. Fast CV demonstrates the production of a very reducible electro-active species that has been produced as a result of oxidation of UA.²⁰

The typical CV response of UA shows one broad irreversible peak at slow potential sweeping (down to $1 \text{ V}\cdot\text{s}^{-1}$) on classical macro-electrodes. By using fast CV ($1 \text{ V}\cdot\text{s}^{-1}$), Dryhurst demonstrated the existence of a weak reduction peak resulting from UA oxidation.²⁰ Indeed, the oxidation of $\text{C}_4=\text{C}_5$ bond of UA gives readily reducible bis-imine (on C_4 atom) that may undergo further irreversible chemical hydration reaction if not quickly electrochemically reduced (figure 4.3). This bis-imine compound is highly reactive and readily reducible. Complete hydration of bis-imine gives rise to uric acid-diol. Conversely, electrochemical oxidation of AA is known to be highly irreversible.²¹ Hence fast CV may be used to selectively determine the concentration of UA in the presence of AA.

The BDD microelectrode (of $40 \mu\text{m}$ diameter) strips fabricated using our technology (refer to chapter 3) were used for the selective and sensitive detection of UA in the presence of low and high quantities of AA. The low double layer capacitance of diamond reduces the background current and potentially increases the signal-to-background ratio. Microelectrodes show a decreased ohmic drop, a hemispherical diffusion layer and a fast establishment of a steady-state signal when compared to macro-electrodes.²² This chapter discusses the electrochemical characterization of the microelectrode, quantification of UA in presence of low and high concentration of AA and in-situ cleaning techniques.

4.1 Electrochemical characterization of BDD microelectrode

Electrochemical characterization where carried out in order to know the reactivity of the electrode, background current and the accessible electrochemical window. A low background current, high reactivity and theoretical steady state limiting current (in a redox couple) is essential for accurate and reproducible measurements.

Figure 4.1a shows the CV in 0.5 M aqueous LiClO_4 solution demonstrating that the accessible potential window of the BDD film is about 3.4 V with a background current of 30 pA at $0.2 \text{ V}\cdot\text{s}^{-1}$. The equivalent Randles circuit of this microelectrode is a three impedance component

(R_S , R_T and C_D), where R_S is the series resistance, R_T the transfer resistance and C_D the double layer capacitance.

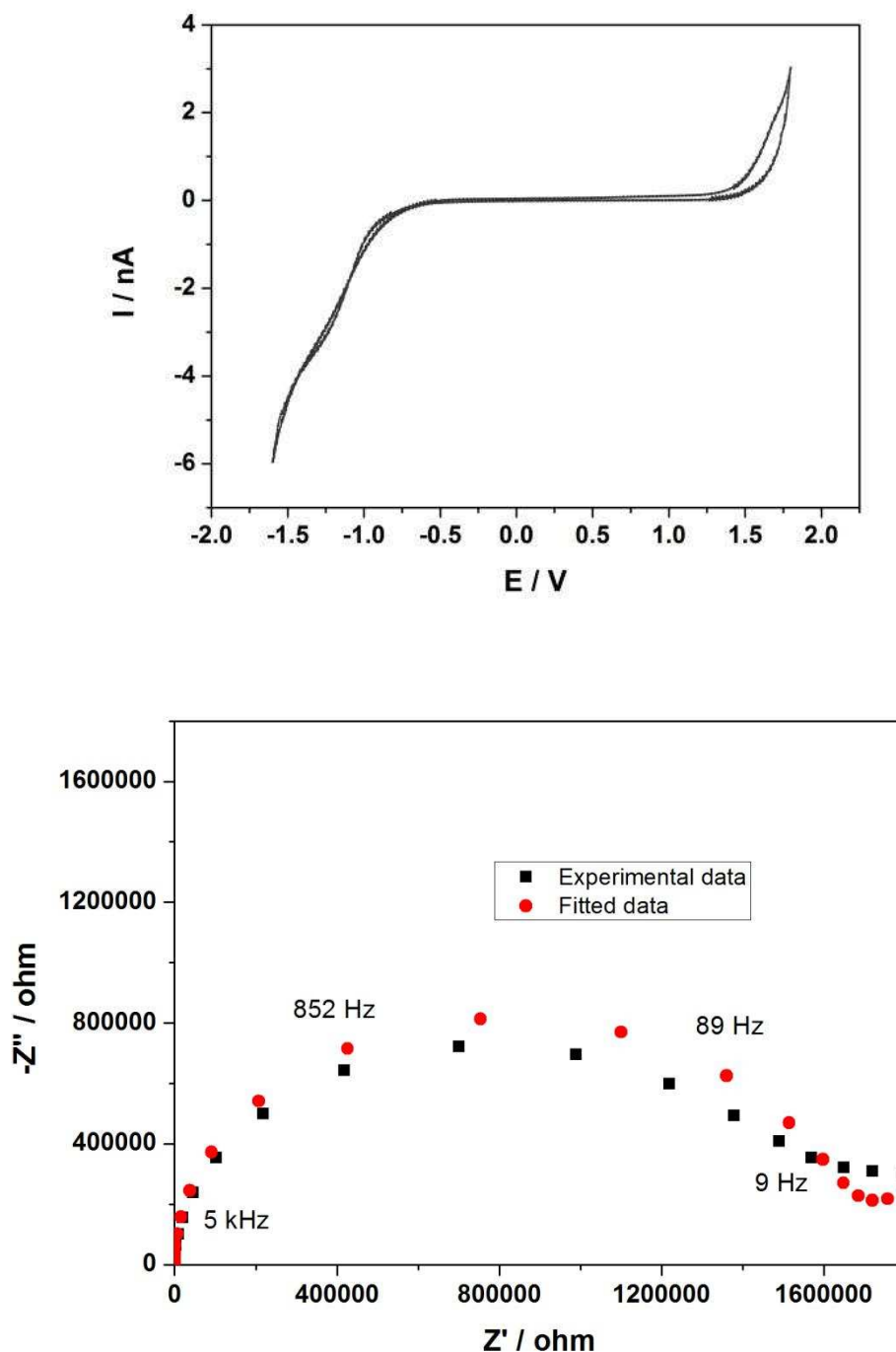


Figure 4.1 (a) Cyclic voltammogram of 40 μm diameter microelectrode in 0.5 M aqueous LiClO_4 solution at 0.2 $\text{V}\cdot\text{s}^{-1}$ and (b) experimental and fitted Nyquist plot obtained at open circuit potential for a modulation of 10 mV rms in aqueous 0.5 M KCl solution containing equimolar ferri/ferrocyanide (1 mM).

An R(C/R) model circuit was used to fit the experimental curves and the impedance values obtained for R_S , R_T and C_D were 263 ohm, 1.4 Mohm and 183 pF respectively. The χ^2 error was suitably low ($\chi^2 < 10^{-4}$), and the error associated with each element was less than 5%. Figure 4.1b shows the experimental and fitted Nyquist plot where the electrodes exhibit a very fast electron transfer rate (k_0) up to $0.02 \text{ cm}\cdot\text{s}^{-1}$. The steady state limiting current i_{lim} is 4.7 nA in a 0.5 M potassium chloride aqueous solution containing 1 mM $\text{Fe}(\text{CN})_6^{4-}$ ion. The variation of calculated i_{lim} from theoretical i_{lim} (5.1 nA) for this electrode was, however, observed to be less than 8% (Diffusion coefficient of ferrocyanide = $6.67 \times 10^{-6} \text{ cm}^2\cdot\text{s}^{-1}$ ²³).

The potential window corresponds to that of diamond and low background current demonstrates that neither cracks nor pinholes were detected in the passivation layer. High electrochemical reactivity characterized by the quick electron transfer rate of $0.02 \text{ cm}\cdot\text{s}^{-1}$ makes this electrode sensitive to amperometric sensing of biomolecules such as uric acid and ascorbic acid. Although several electrodes were tested, this particular electrode (40 μm in diameter) was used for the electro-analytical based on its closeness to the theoretical limiting current values and low background current.

4.2 Cyclic voltammogram of uric acid and ascorbic acid

UA and AA coexist in physiological liquid with overlapping oxidation potential on most electrodes. We did some studies on diamond electrodes to analyze the overlapping CV behavior.

UA and AA solutions were prepared daily by dissolving in phosphate buffered saline (PBS) aqueous solution of pH 7.2. The electrode was scanned from -0.3 V to 1.4 V vs Ag/AgCl. Figure 4.2 shows the CV of AA and UA recorded at low scan rate ($0.1 \text{ V}\cdot\text{s}^{-1}$) under steady state hemispherical diffusion in PBS buffer. Both AA and UA exhibit well defined oxidation waves with half-wave potentials around 0.5 V vs Ag/AgCl that correspond to the irreversible exchange of 2 electrons and 2 protons^{20,21} at this scan rate. These CVs clearly indicate the overlapping of the electrochemical oxidation waves of both species at the same potential range.

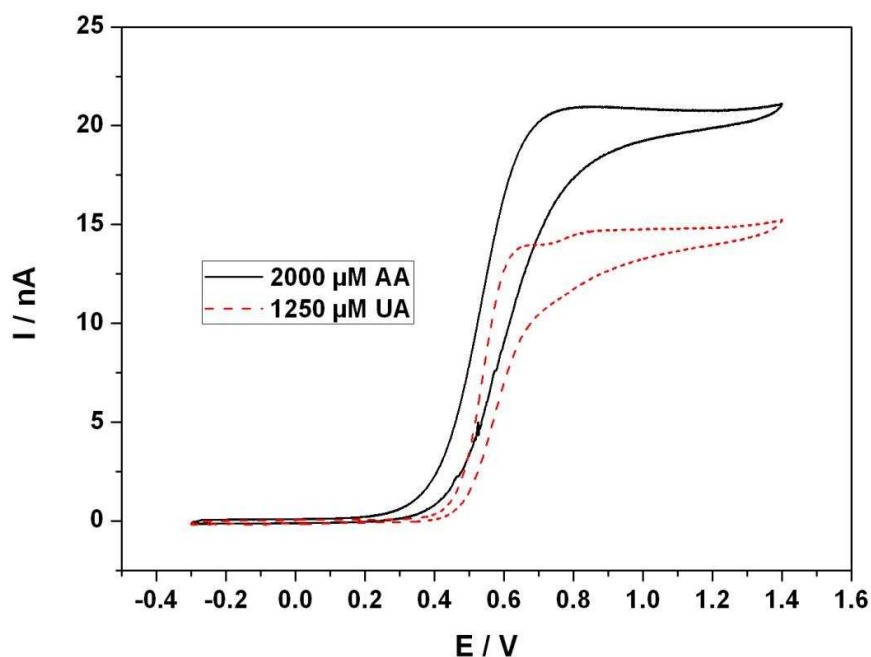


Figure 4.2 Cyclic voltammogram of uric acid (dashed line) and ascorbic acid in phosphate buffer solution scanned at $0.1 \text{ V}\cdot\text{s}^{-1}$ indicating overlapping oxidation potential with half-wave potentials around 0.5 V vs Ag/AgCl.

More precisely, the EC oxidation of UA gives, through reversible 2 electrons-two protons exchange, an unstable bis-imine that could exist in two tautomeric forms (species IIa and IIb, figure 4.3).²⁴ This bis-imine compound is then decomposed, at the experimentally used pH of 7.2, into uric acid-4,5-diol (species IV, figure 4.3), through two, fast irreversible hydration steps.

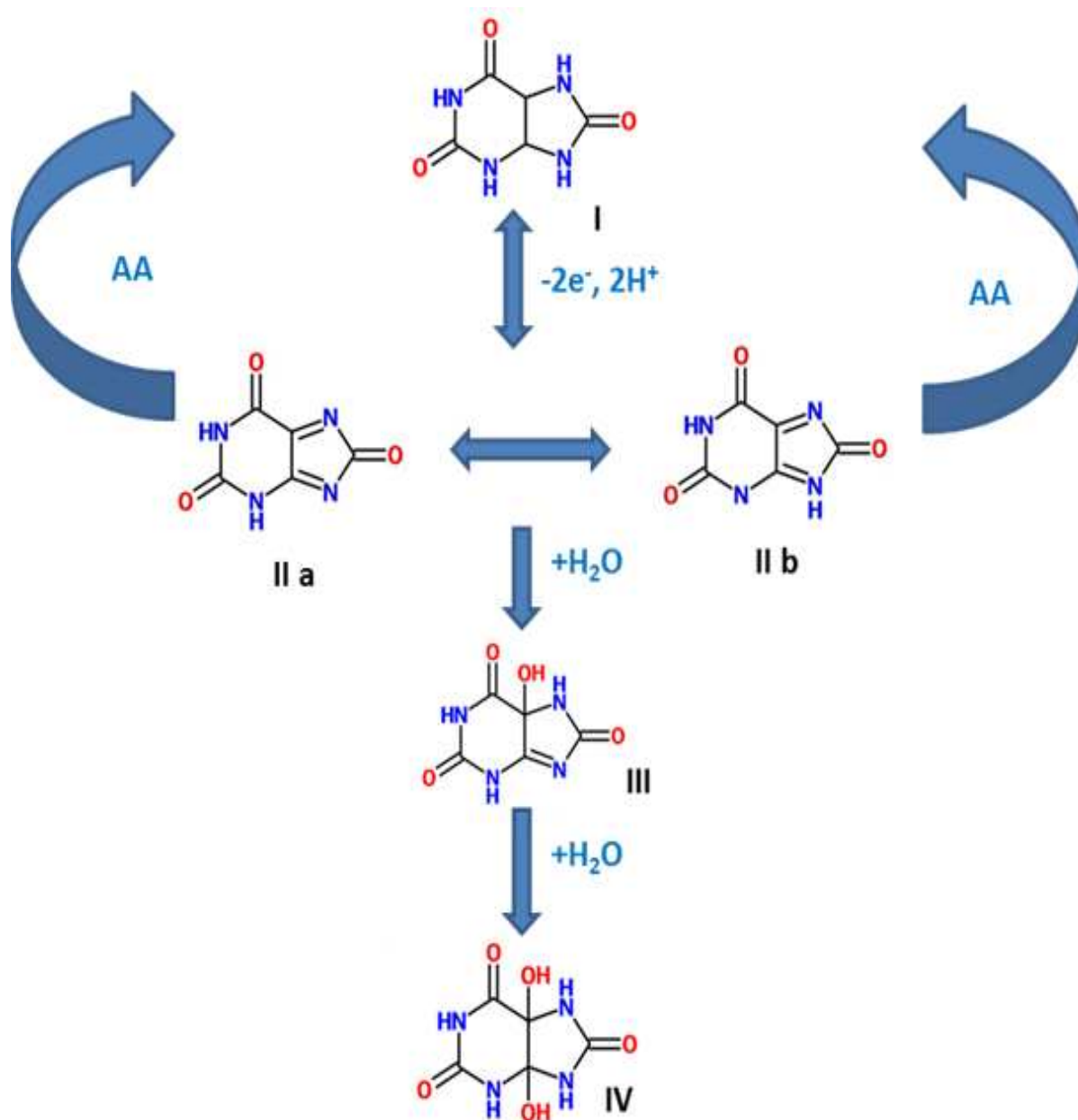


Figure 4.3 Proposed schematics for UA oxidation in the presence/absence of AA where (I) is UA, (II) bis-imine compound, (III) imine-alcohol compound and (IV) uric acid-4,5-diol.

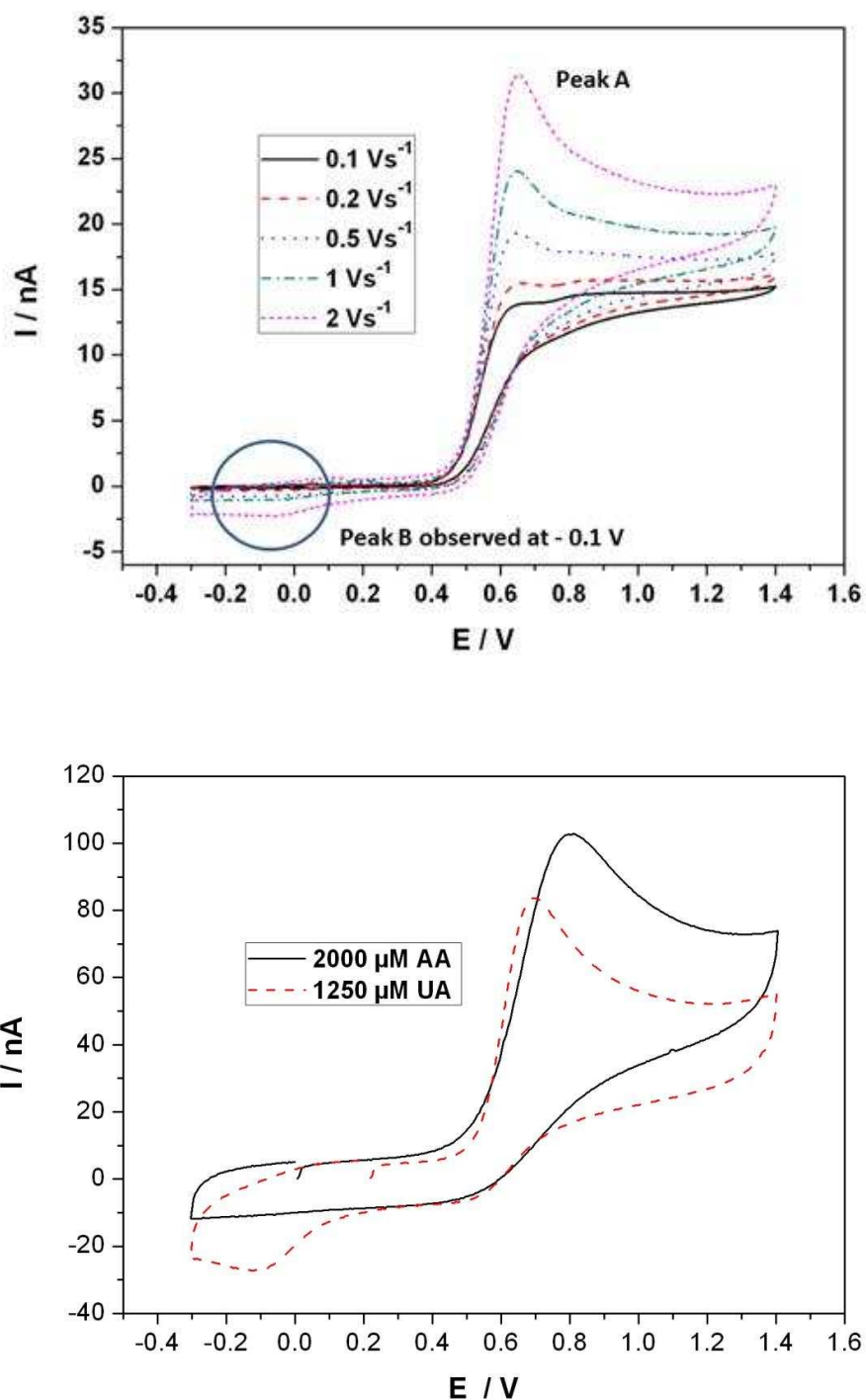


Figure 4.4 (a) Cyclic voltammogram of uric acid scanned from 0.1 to 1 V.s⁻¹. When the scan rate is higher than 0.5 V.s⁻¹, a reduction peak (peak B) appears around -0.1 V vs Ag/AgCl and (b) cyclic voltammogram of uric acid (dashed line) and ascorbic acid in phosphate buffer solution scanned at 20 V.s⁻¹.

By increasing the scan rate from 0.1 to 20 V.s⁻¹, one can see, as already mentioned by Dryhurst,²⁰ the appearance of a weak reduction peak (for which the amplitude increases with the scan rate; refer to figure 4.4a) at a potential of -0.1 V vs Ag/AgCl (figure 4.4b). Indeed, provided the sweep rate is fast enough, the primary oxidized products IIa or IIb can be electrochemically reduced owing to the reversibility of the first oxidation step due to the instability of the imine compound. At slower scan rates, oxidation products of UA are rapidly hydrated to irreversible uric acid-4,5-diol. In contrast to UA and as expected, no reduction wave of the electrochemically produced dehydroascorbic acid (DHAA) was observed within the scanned potential window (figure 4.4b), even at the highest investigated scan rate of 20 V.s⁻¹. However, DHAA is known to strongly adsorb at electrochemical interfaces and may induce diamond fouling along UA determination. Hence, according to the aforementioned electrochemical behavior, fast CV can be used to selectively determine the concentration of UA.

Elsewhere, one can deduce from figure 4.2 for UA, the existence of a second flat wave (oxidation half-wave potential of 0.8V vs Ag/AgCl). Indeed, uric acid-4,5-diol undergoes subsequent chemical rearrangement at pH 7 leading to the formation of allantoin and urea as main products. However, parabanic acid can be also produced from uric acid-4,5-diol, through complex chemical rearrangement to dihydroxyimidazole and subsequent 2 electrons-2 protons electrochemical oxidation. Indeed, Dryhurst clearly shown that such latter decomposition follows a minority path which increases in yield with acidity of the media.^{20,24} Moreover, the yield of this secondary path strongly depends on the electrode material as reported by Struck et al.²⁵ who detected parabanic acid reduction using polarography following UA oxidation at spectroscopic graphite electrode in place of pyrolytic graphite. In such a way, according to the local pH decrease at the vicinity of the electrode owing to UA oxidation and to the acidic compartment and the nature of hydrogenated diamond electrodes, parabanic acid may be produced with a yield of around 6 % (obtained from ratio of the plateau limiting currents that involve both 2 electrons and 2 protons). One can notice, the disappearance of such a second electrochemical step in fast CV (figure 4.4b), this behavior can be ascribed to the enhanced electrochemical recycling of UA that decreases the yield of production of parabanic acid which is produced through a slow chemical and electrochemical pathway. Moreover, this second electrochemical oxidation is hardly visible due to the Cottrell behavior of the anodic current of UA primary oxidation wave.

4.3 Calibration curves for UA concentration

Cyclic voltammograms of PBS solution containing uric acid and ascorbic acid are different when the concentration of ascorbic acid exceeds 1 mM. For lower concentrations of ascorbic acid (less than 1 mM) an oxidation and a reduction peak were observed and the calibration process is explained in section 4.3.1. Section 4.3.2 explains the calibration of uric acid at higher ascorbic acid concentration (more than 1 mM) where two oxidation peaks were observed. Hence two calibration processes were modeled for low and high concentration of ascorbic acid and are termed as Model 1 and 2 respectively.

4.3.1 Model 1: Low ascorbic acid concentration

CV of UA (1 mM), at BDD electrode in a solution that contains varying concentrations of AA, is shown in figure 4.5. In order to plot the calibration curve, the concentration of UA solution was varied from 0, 500, 1000, 1500, 2000 to 2500 μM and AA concentration from 0, 250 to 500 μM . CVs of different combinations of UA and AA mixtures were carried out and the peak oxidation current (i_A) and peak reduction current (i_B) were recorded at $20 \text{ V}\cdot\text{s}^{-1}$.

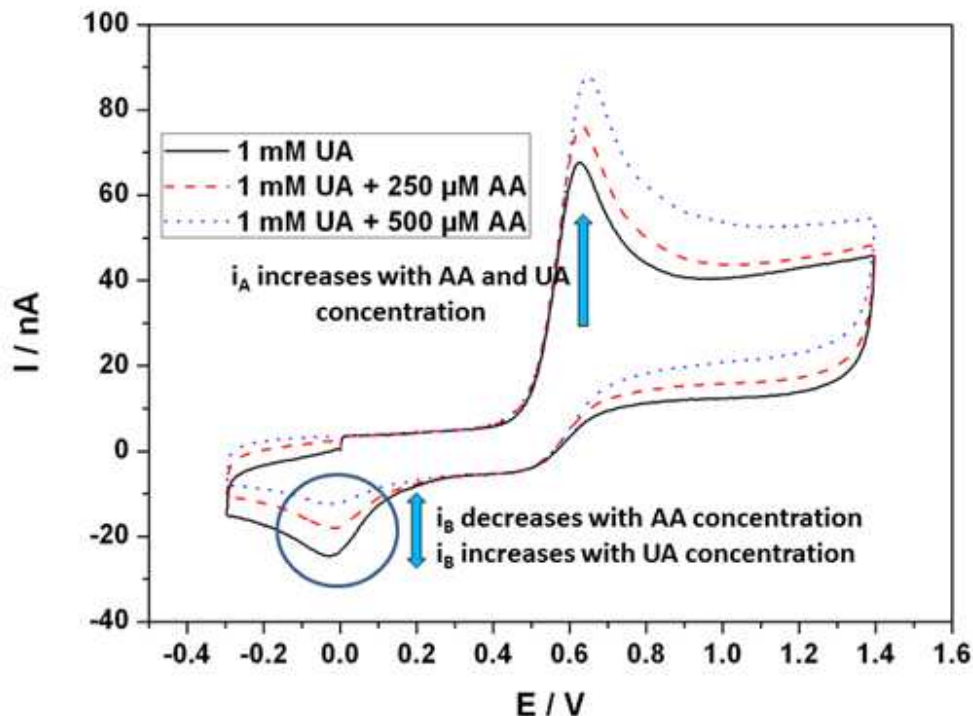


Figure 4.5 Cyclic voltammogram of 1 mM uric acid and ascorbic acid (0, 250 and 500 μM) in phosphate buffer solution scanned at $20 \text{ V}\cdot\text{s}^{-1}$.

Two 3D curves (figure 4.6 and 4.7) were plotted with UA and AA concentrations (C_{UA} and C_{AA}) on X and Y axis and i_A or i_B values on Z axis respectively (see Appendix A for more details). Two second order equations were derived from the curve which corresponds to Model 1:

$$i_A = 4.24 + 0.07C_{UA} + 0.06C_{AA} - 2.9 \times 10^{-6}C_{UA}^2 - 2.36 \times 10^{-5}C_{AA}^2 - 1.82 \times 10^{-5}C_{UA}C_{AA} \quad (4.1)$$

$$i_B = 8.2 + 0.02C_{UA} - 0.009C_{AA} - 1.9 \times 10^{-6}C_{UA}^2 - 2.67 \times 10^{-7}C_{AA}^2 - 8.52 \times 10^{-6}C_{UA}C_{AA} \quad (4.2)$$

By solving the equation 4.1 and 4.2, the concentration of UA and AA (C_{UA} and C_{AA}) can be obtained. It was observed that i_A increases with the concentration of UA as well as that of AA whereas i_B decreases with concentrations of AA but increases with concentrations of UA. AA can deactivate the BDD electrode due to deposition of its oxidation product. It was observed that the reactivity (k_0) of the active BDD electrode was reduced by 10% after few CVs in solutions containing AA. This could be one explanation for the decrease in i_B values when the concentration of AA is increased. The other assumption is derived from the anti-oxidant nature of AA. AA is known to reduce quinone imines.²⁶ In the presence of AA, the bis-imines might have been attacked or quickly reduced to UA chemically. Hence, as the concentration of AA is increased, the amplitude of i_B is decreased.

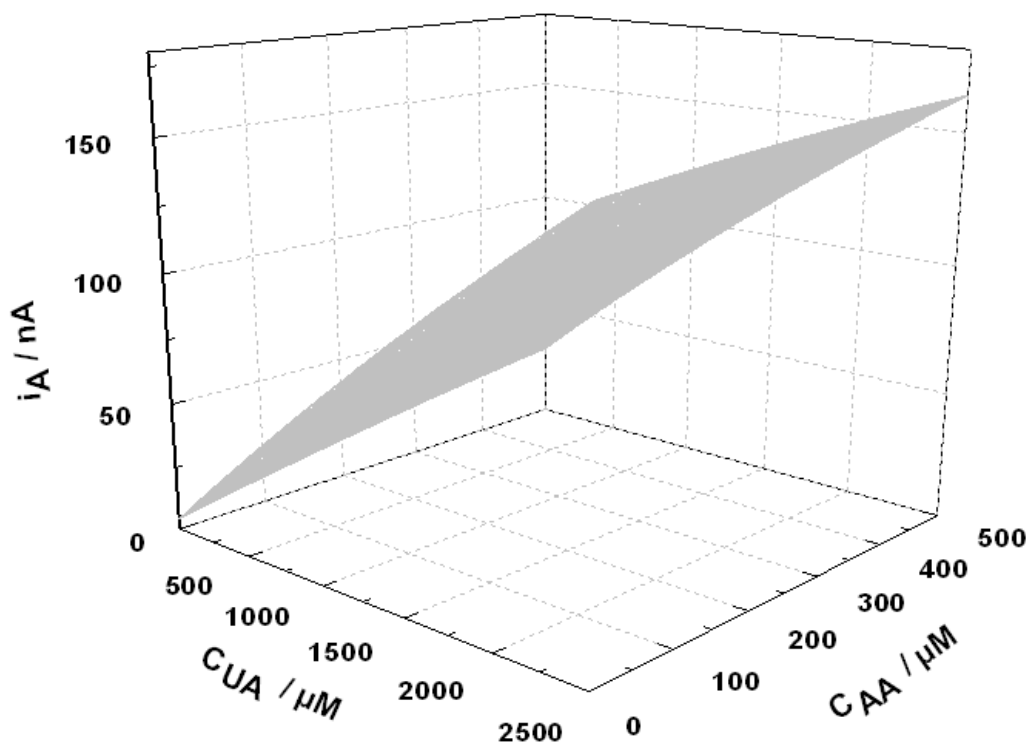


Figure 4.6 Second order curve fitting results for UA concentration (C_{UA}) at low concentration of AA (C_{AA}) where i_A is the peak oxidation current observed at 20 V.s⁻¹.

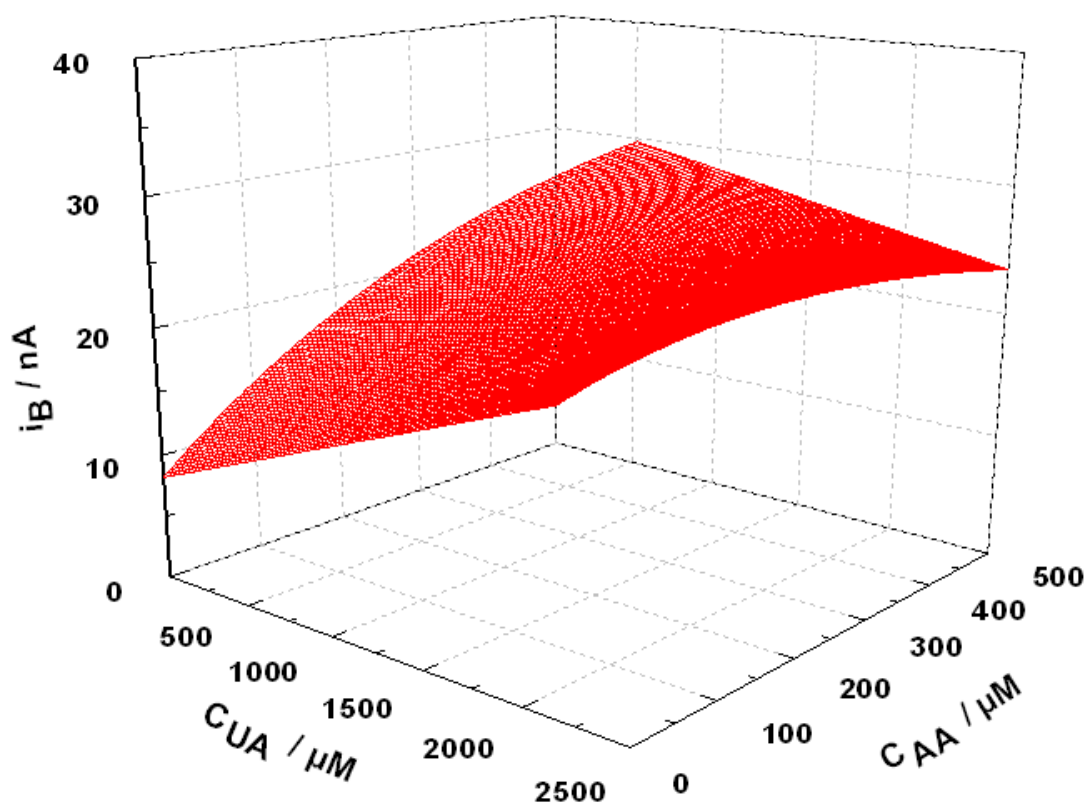


Figure 4.7 Second order curve fitting results for UA concentration (C_{UA}) at low concentration of AA (C_{AA}) where i_B is the peak reduction current observed at 20 V.s^{-1} .

4.3.2 Model 2: High ascorbic acid concentration

When the concentration of AA was increased beyond 1mM, the peak B disappeared completely for UA concentrations below 2 mM. Hence model 1 cannot be used to determine the concentration of UA. However a third peak (peak C) appears at 0.8 V vs Ag/AgCl as seen in figure 4.8 when the electrodes were scanned from -0.3 V to 1.4 V. Thus, a second model (Model 2) is proposed using the two peaks (peak A and C) and their corresponding oxidation peak currents (i_A and i_C). For different concentrations of UA and AA mixtures, the peak oxidation current (i_A) and second peak oxidation current (i_C) were extracted from the CV measurements at 20 V.s^{-1} . The concentration of UA solution was varied from 0, 500, 1000, 1500, 2000 to 2500 μM and AA concentration from 1, 3, 5, 7 to 9 mM.

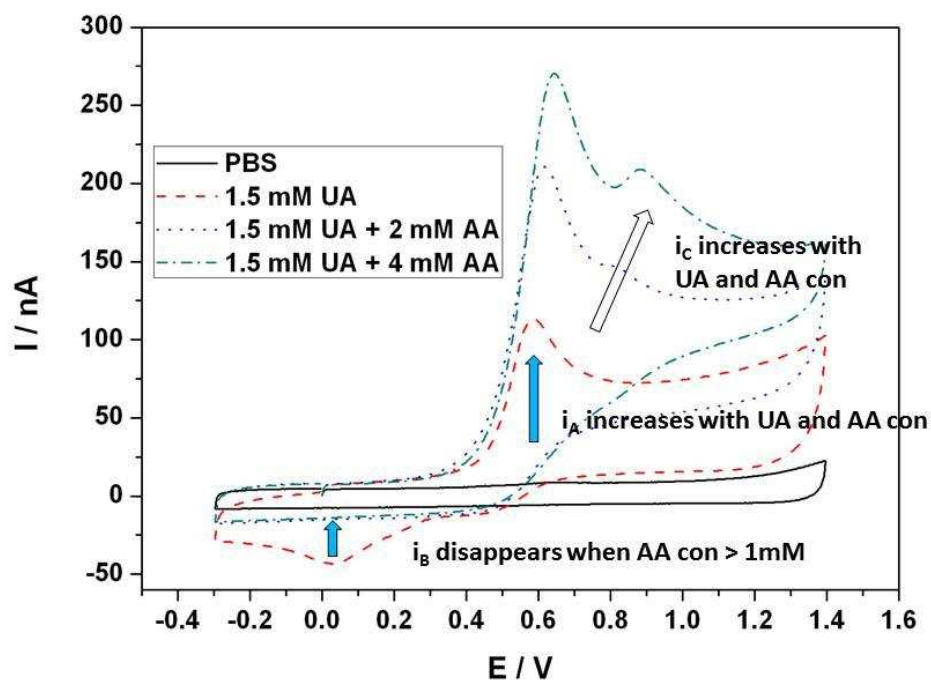


Figure 4.8 Cyclic voltammogram of 1.5 mM uric acid and ascorbic acid (0, 2 and 4 mM) in phosphate buffer saline solution scanned at $20 \text{ V}\cdot\text{s}^{-1}$.

Like Model 1, two 3D curves (figure 4.9 and 4.10) were plotted with UA and AA concentrations (C_{UA} and C_{AA}) on the X and Y axis and i_{A} or i_{C} values on Z axis respectively (see Appendix A for more details). The equations of Model 2 are:

$$i_{\text{A}} = 53.48 + 0.05C_{\text{UA}} + 0.03C_{\text{AA}} - 2.56 \times 10^{-6}C_{\text{UA}}^2 - 6.69 \times 10^{-9}C_{\text{AA}}^2 - 5.75 \times 10^{-6}C_{\text{UA}}C_{\text{AA}} \quad (4.3)$$

$$i_{\text{C}} = 38.4 + 0.015C_{\text{UA}} + 0.02C_{\text{AA}} + 3.29 \times 10^{-6}C_{\text{UA}}^2 + 5.11 \times 10^{-7}C_{\text{AA}}^2 + 3.93 \times 10^{-6}C_{\text{UA}}C_{\text{AA}} \quad (4.4)$$

The concentration of UA and AA (C_{UA} and C_{AA}) can thus be obtained by solving equations 4.3 and 4.4. Both i_{A} and i_{C} increases with the concentration of UA and that of AA. For higher concentrations of AA ($> 5 \text{ mM}$), it was observed that the value i_{A} does not depend much on UA concentration. As proposed earlier, the AA catalyzes the production of imine-alcohol, no peak B is observed at higher concentrations of AA. On BDD electrodes, the peak C was not observed during the CV in solely AA even at higher concentrations.

The simultaneous oxidation of UA in presence of high concentrations of AA presents a complex mechanism. At higher concentration of AA, the adsorbed oxidation products of AA influence the electro-kinetics of UA oxidation. A possible explanation is related to the fouling properties of DHAA. Thereby, due to the blockade of electroactive sites by DHAA, UA

oxidation may take place through two different pathways: one via still electroactive DHAA-free diamond-surface sites and one via DHAA blocked sites through the adsorbed species.

Oxidation of UA at the active sites and at the fouled surface could cause the peak separation. On the other hand, one can note that peak C potential fits quite well with the potential of the second plateau observed at slow scan rate, thus suggesting the presence of parabanic acid. Hence, the increase in the peak C amplitude with both UA and AA can be explained first by a higher generation of parabanic acid with UA concentration and secondly to the possible recycling of parabanic acid owing to the antioxidant nature of AA. Indeed, some complementary studies are necessary to examine more in depth the contributions of parabanic acid and/or DHAA fouling.

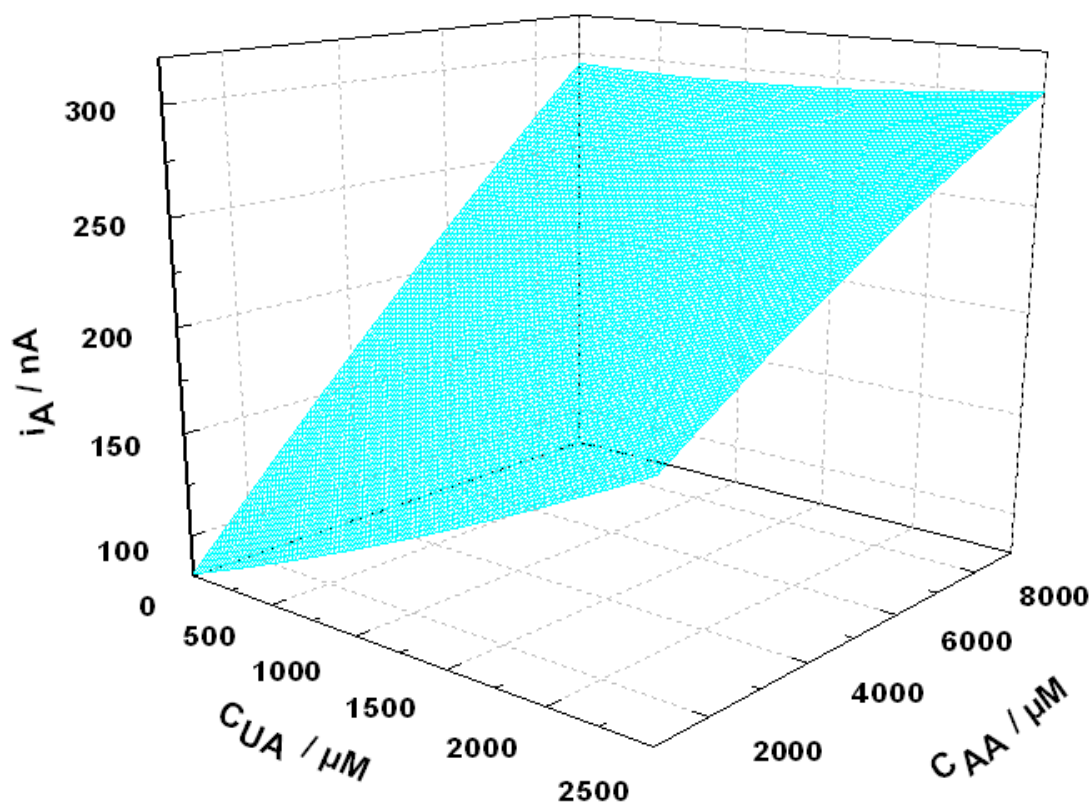


Figure 4.9 Second order curve fitting results for UA concentration (C_{UA}) at high concentration of AA (C_{AA}) where i_A is the peak oxidation current observed at $20 \text{ V}\cdot\text{s}^{-1}$.

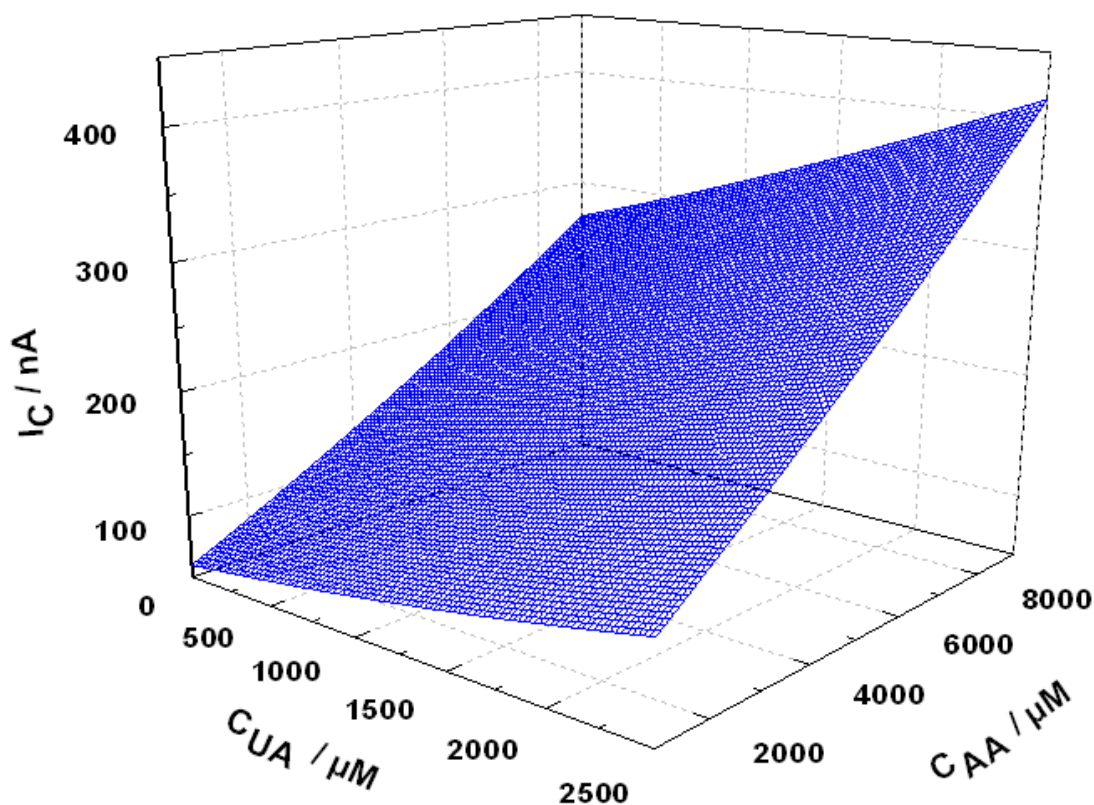


Figure 4.10 Second order curve fitting results for UA concentration (C_{UA}) at high concentration of AA (C_{AA}) where i_c is the second oxidation current observed at $20 \text{ V}\cdot\text{s}^{-1}$.

4.4 Proposed model vs Spectrophotometric quantification

Human urine samples were collected from volunteers as real samples for analysis by the proposed models and were compared to spectrophotometric method. In the spectrophotometric method, uric acid is oxidized to allantoin in the presence of enzyme uricase, which leads to formation of H_2O_2 which reacts with 4-amino phenazone in the presence of peroxidase to form quinone-diimine. The intensity of the color of the quinone diimine is directly proportional to the concentration of uric acid. Human urine samples were neither diluted nor pretreated for EC quantification by the proposed models. CV was done on each urine sample and, based on the nature of the peaks, using model 1 or model 2; the equations were solved to identify the UA value.

The results are presented in Table 4.1. The measured values using the proposed model were observed to be very close to the spectrophotometric results with a maximum difference of 13%. The percentage error was calculated using the following formula:

$$\%E = (P.M - S)/S \quad (4.5)$$

where P.M is the values obtained from proposed models and S that of spectrophotometry. The spectrophotometric measuring technique, although widely used in the field of UA estimation has an error percentage of 5%. UA and AA are fast antioxidants and the time lag between the spectrophotometric and EC measurement might have also influenced the difference in the results. The other parameter which could affect the measurement is the variation in electron transfer rate k_0 of the electrode.

Table 4.1 Comparison of uric acid concentration measured in different urine sample using model 1 or model 2 and the spectrophotometric technique.

Sample No.	Spectrophotometer (mM)	Proposed Model (mM)	% Error
1	3.66	4.15	13
2	4.76	5.1	7
3	3.01	2.68	-11
4	5.90	5.15	-12
5	2.78	2.74	-1.4

4.5 Automation of quantification procedure and in-situ cleaning

When electrodes are used continuously in a biological fluid, they lose their reactivity because of fouling²⁷. Electrode fouling can be due to adsorption or adhesion of biomolecules such as proteins, enzymes, cells, intermediate products of oxidation of organic compounds, etc²⁸. Although hydrogen-terminated BDD exhibit high reactivity, continuous use in urine leads to deactivation of electrode reactivity because of fouling. This would lead to difficulty in the automation of the quantification process. In chapter 2, we demonstrated an in-situ activation process of BDD electrodes which has been tried on several biological and synthetic fluids.

Human urine samples were diluted 2 fold in PBS solution. From this solution, 5 other solutions were prepared by adding different quantities of UA (400, 800, 1200, 1600 and 2000 μ M). CVs at 20 V.s⁻¹ were performed in solutions 1 (diluted urine) to 6 (diluted urine + 2000 μ M UA). i_A and i_B values were obtained from each scan and from the CV of solution 1 the UA concentration was estimated to be 2012 μ M. It was observed that the values of i_A and i_B were not increased as expected, after each scan (solution 1 to 6) despite the increase in concentration of UA (figure 4.11). This is due to fouling of the electrode. The electrodes were EC cleaned and CVs were carried out from solution 1 (diluted urine) to 6 (diluted urine + 2000 μ M UA). Between each CV the electrodes were activated in the previous solution. The

EC activation was performed directly in the solution containing urine, by applying a train of negative current pulses consisting of 3 pulses where each pulse had an amplitude of $-100 \text{ mA}\cdot\text{cm}^{-2}$ and duration of 100 ms and duty cycle of 90 % (refer to chapter 2 section 2.6). The values of i_A and i_B increased after each scan as expected (figure 4.12).

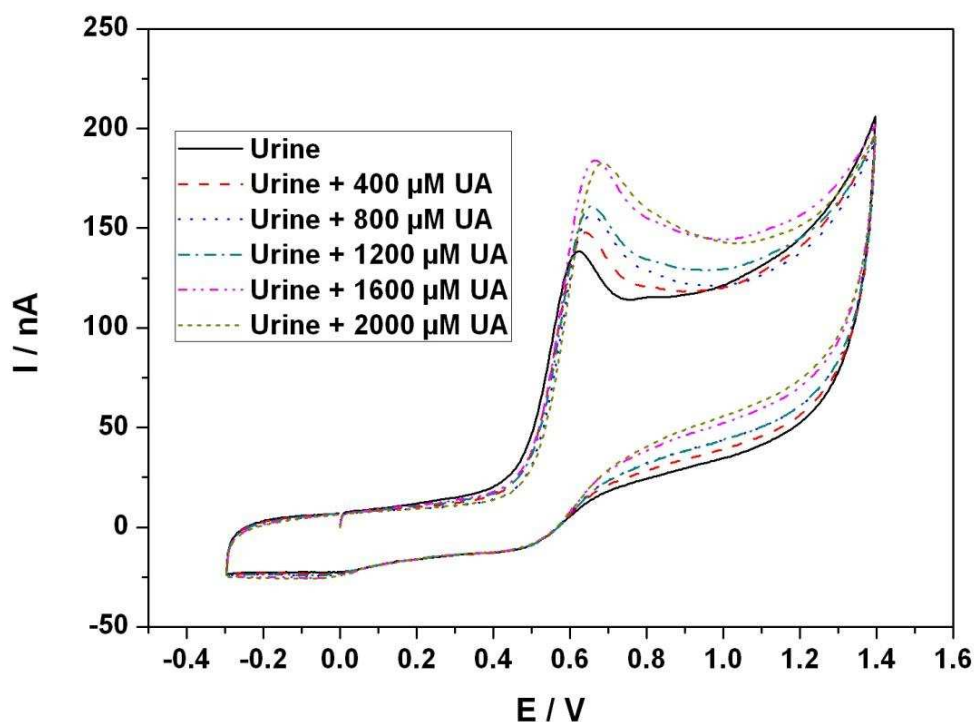


Figure 4.11 Cyclic voltammogram of urine diluted by 2 fold and that of diluted urine containing added uric acid ($250 - 1250 \mu\text{M}$) scanned at $20 \text{ V}\cdot\text{s}^{-1}$.

Values of i_A and i_B were extracted from these graphs and are denoted i_{AO1} , i_{BO1} and i_{AO2} , i_{BO2} for trials with and without activation in between two CVs. Also the theoretical values of i_A and i_B were calculated using the models and were denoted i_{AC} and i_{BC} . Comparison between the calculated value i_{AC} and the observed values i_{AO1} (trials with activation) and i_{AO2} (trials without activation) shows that there is a negligible difference between i_{AC} and i_{AO1} when compared to the difference between i_{AC} and i_{AO2} . The percentage difference between calculated and observed values was estimated using the following formula:

$$E = (i_C - i_O) / i_C \quad (4.6)$$

with E_{A1} the percentage difference between i_{AC} and i_{AO1} and E_{A2} the percentage difference between i_{AC} and i_{AO2} , E_{B1} is the percentage difference between i_{BC} and i_{BO1} and E_{B2} is the

percentage difference between i_{BC} and i_{BO2} . A detailed comparison between the different values is depicted in table 4.2 and figure 4.13.

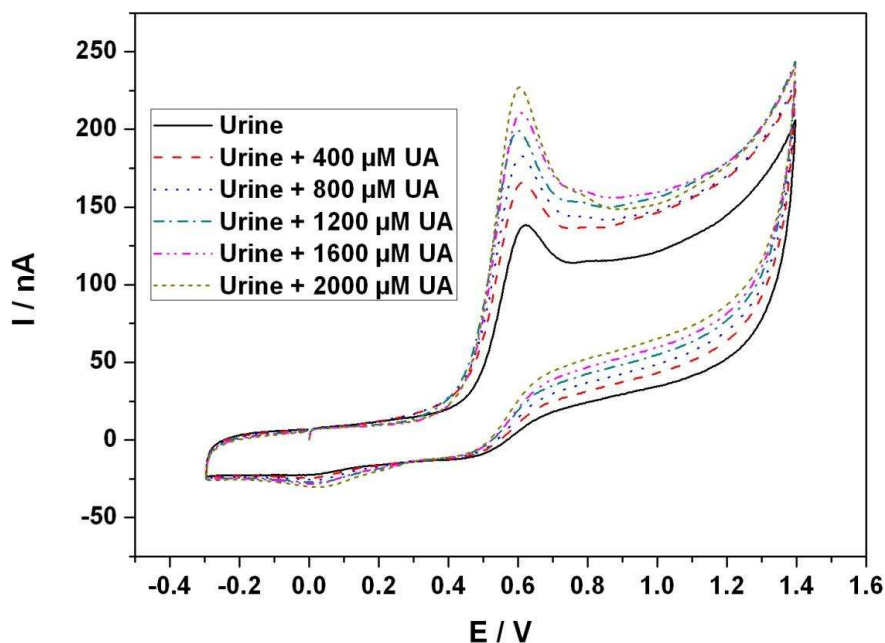


Figure 4.12 Cyclic voltammogram of urine diluted 2 fold and that of diluted urine containing added uric acid (250 – 1250 μ M) scanned at 20 $V.s^{-1}$. The electrodes were activated electrochemically in the same solution in between two successive scans.

Table 4.2 Comparison between the calculated values (i_{AC} , i_{BC}), observed values with activation between CVs (i_{AO1} , i_{BO1}) and observed values without activation between CVs (i_{AO2} , i_{BO2}) for the peak currents i_A and i_B extracted from CV in urine solutions 1 to 6 where E_{A1} , E_{A2} , E_{B1} and E_{B2} are percentage differences of observed values from calculated values.

UA Conc. (μ M)	i_{AC} (nA)	i_{AO1} (nA)	E_{A1} (%)	i_{AO2} (nA)	E_{A2} (%)	i_{BC} (nA)	i_{BO1} (nA)	E_{B1} (%)	i_{BO2} (nA)	E_{B2} (%)
2012	138	138	0	138	0	-25	-25	0	-25	0
2412	157.3	162	-2.99	150	4.64	-27.06	-26	3.92	-26	3.92
2812	176.83	182	-2.92	156	11.77	-28.54	-27	5.39	-25	12.40
3212	194.85	200	-2.64	161	17.37	-29.39	-28	4.72	-25	14.94
3612	211.95	210	0.92	174	17.90	-29.63	-28.5	3.81	-25	15.63
4012	228.1	228	0.04	172	24.59	-29.95	-30	-0.17	-24	19.87

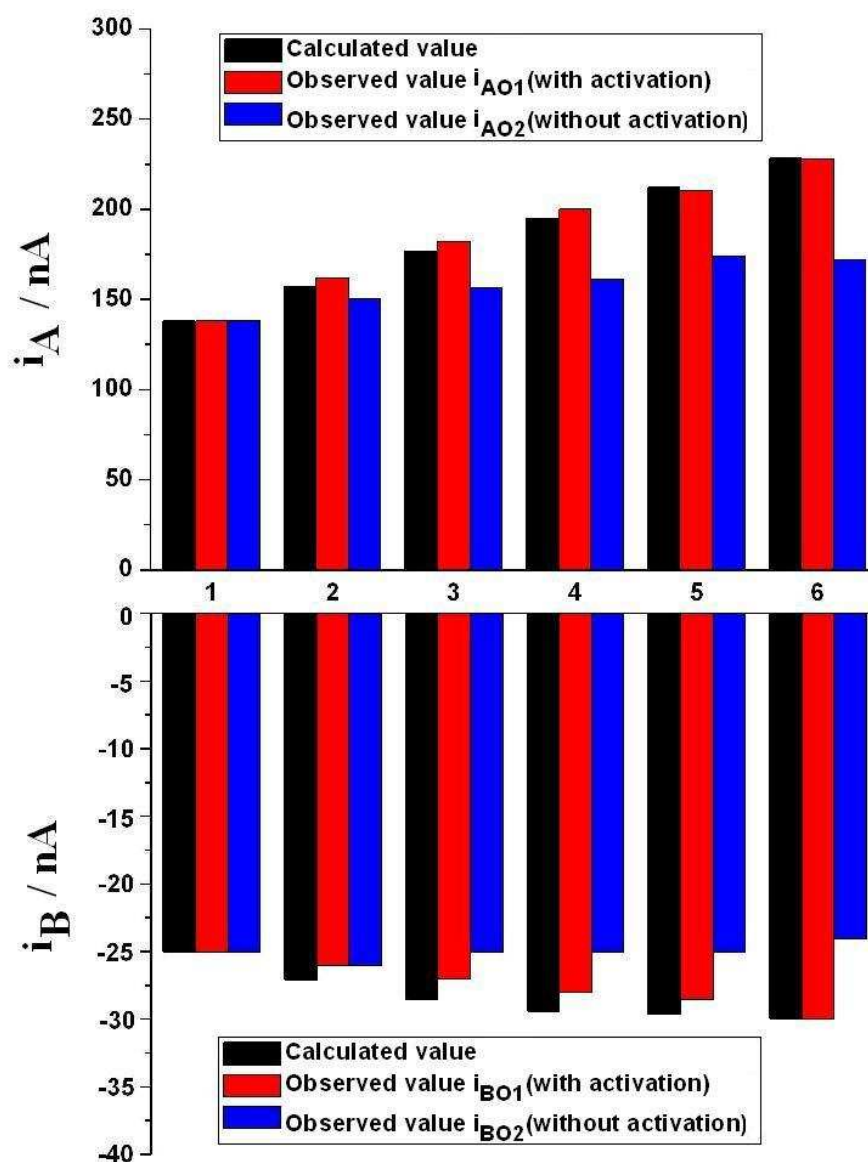


Figure 4.13 Comparison between the calculated value (i_{AC} , i_{BC}), observed value with activation between CVs (i_{AO1} , i_{BO1}) and observed value without activation between CVs (i_{AO2} , i_{BO2}) for the peak currents i_A and i_B extracted from CV in urine solutions 1 to 6.

Due to heavy fouling of the electrode, the electrode was deactivated and hence the value of E_{A2} is as high as 25%. As the electrode is not activated after each CV, the value of E_{A2} increased after each scan. In contrast, the value of E_{A1} is less than 3% indicating the closeness of calculated values and observed values. The same is the case for E_{B1} and E_{B2} with a maximum E_{B1} of 5.4% and E_{B2} of 20%. It is clearly demonstrated that a simple EC activation

procedure can restore the lost reactivity of the electrode and the electrode can be reused in the sample solution for further measurements.

Conclusions

Selective determination of UA in the presence of AA was achieved using a BDD microelectrode without any further modification. Comparison of the EC quantification technique and the spectrophotometric technique shows that an accurate measurement can be carried out using the 2 proposed models. This technique highlights the potential of BDD microelectrodes as electro-analytical sensors owing to their low double layer capacitance, robustness at high current density and corrosion resistance. The EC treatment retrieves the lost reactivity of an electrode fouled by urine without using any specific reagent or solution. The advantage of this technique is that it can enhance the reusability of the BDD microelectrode by activating in urine itself. This demonstrates the possibility of automation of UA quantification as the electrode can be activated directly in urine and hence it can be used for continuous monitoring for long period of time. The time taken for activation is 300 ms and the time taken for CV at 20 V.s^{-1} is less than 200 ms.

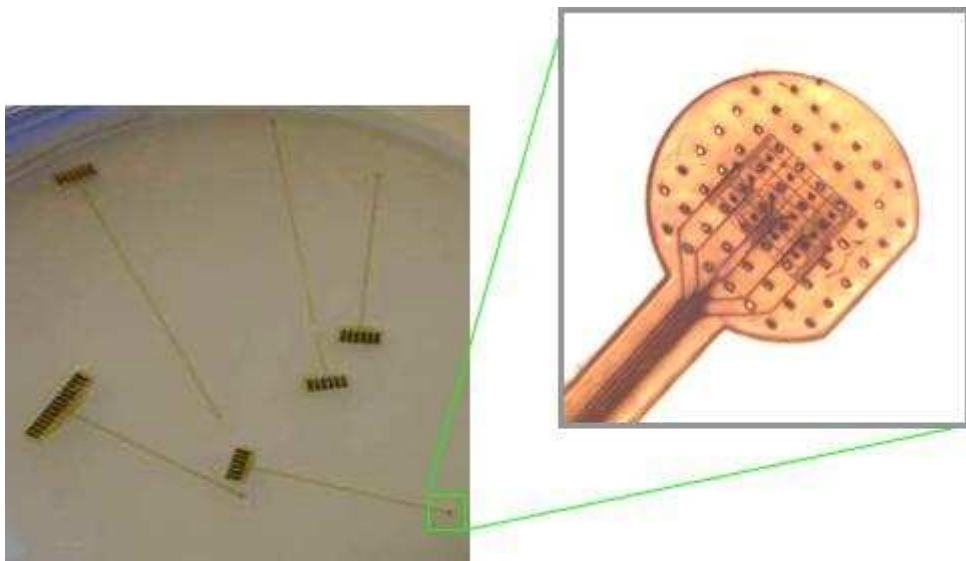
Bibliography

- (1) Álvarez-Lario, B.; Macarrón-Vicente, J. *Rheumatology (Oxford, England)* **2010**, *49*, 2010–2015.
- (2) Popa, E.; Kubota, Y.; Tryk, D. A.; Fujishima, A. *Analytical chemistry* **2000**, *72*, 1724–1727.
- (3) Amir, W.; Mohammad, Y.; Abdul, N.; Ghulam, M.; Izhar, H. *Chemical Research in Chinese Universities* **2011**, *27*, 929–933.
- (4) Martinon, F.; Pétrilli, V.; Mayor, A.; Tardivel, A.; Tschopp, J. *Nature* **2006**, *440*, 237–241.
- (5) Daoussis, D.; Kitas, G. D. *Rheumatology (Oxford, England)* **2011**, *50*, 1354–1355.
- (6) Sun, Q.; Shen, Y.; Sun, N.; Zhang, G. J.; Chen, Z.; Fan, J. F.; Jia, L. Q.; Xiao, H. Z.; Li, X. R.; Puschner, B. *European journal of pediatrics* **2010**, *169*, 483–489.
- (7) Shaikh, A.; Wiisanen, M. E.; Gunderson, H. D.; Leung, N. *The Annals of pharmacotherapy* **2009**, *43*, 1370–1373.
- (8) Dinour, D.; Gray, N. K.; Campbell, S.; Shu, X.; Sawyer, L.; Richardson, W.; Rechavi, G.; Amariglio, N.; Ganon, L.; Sela, B.-A.; Bahat, H.; Goldman, M.; Weissgarten, J.; Millar, M. R.; Wright, A. F.; Holtzman, E. J. *Journal of the American Society of Nephrology : JASN* **2010**, *21*, 64–72.
- (9) Lameire, N.; Van Biesen, W.; Vanholder, R. *Nephrology, dialysis, transplantation : official publication of the European Dialysis and Transplant Association - European Renal Association* **1999**, *14*, 2570–2573.
- (10) Li, Y.; Lin, X. *Sensors and Actuators B: Chemical* **2006**, *115*, 134–139.
- (11) Lin, X.; Zhang, Y.; Chen, W.; Wu, P. *Sensors and Actuators B: Chemical* **2007**, *122*, 309–314.
- (12) Lin, L.; Chen, J.; Yao, H.; Chen, Y.; Zheng, Y.; Lin, X. *Bioelectrochemistry (Amsterdam, Netherlands)* **2008**, *73*, 11–17.
- (13) Zen, J.; Tang, J. *Anal. Chem.* **1995**, *67*, 1892–1895.
- (14) Zen, J.-M.; Chen, P.-J. *Analytical Chemistry* **1997**, *69*, 5087–5093.
- (15) Wang, Z.; Wang, Y.; Luo, G. *The Analyst* **2002**, *127*, 1353–1358.
- (16) Fernandez, L.; Carrero, H. *Electrochimica Acta* **2005**, *50*, 1233–1240.
- (17) Nakaminami, T.; Ito, S.; Kuwabata, S.; Yoneyama, H. *Analytical chemistry* **1999**, *71*, 1928–1934.

- (18) Strochkova, E. M.; Tur'yan, Y. I.; Kuselman, I.; Shenhar, a Talanta **1997**, 44, 1923–8.
- (19) Safavi, A.; Maleki, N.; Moradlou, O.; Tajabadi, F. Analytical biochemistry **2006**, 359, 224–9.
- (20) Dryhurst, G. Journal of electrochemical society **1972**, 119, 1659–1664.
- (21) Hu, I.-F.; Kuwana, T. Analytical chemistry **1986**, 58, 3235–3239.
- (22) Lawrence, N. S.; Pagels, M.; Meredith, A.; Jones, T. G. J.; Hall, C. E.; Pickles, C. S. J.; Godfried, H. P.; Banks, C. E.; Compton, R. G.; Jiang, L. Talanta **2006**, 69, 829–834.
- (23) Konopka, S. J.; Mcduffie, B. Analytical chemistry **1970**, 42, 1741–1746.
- (24) Fry, A. J.; Dryhurst, G. Organic Electrochemistry; Springer-Verlag, 1972; p. 85.
- (25) Struck, W. A.; Elving, P. J. Analytical chemistry **1964**, 36, 1374–1375.
- (26) Kang, P.; Dalvie, D.; Smith, E.; Renner, M. Chemical research in toxicology **2009**, 22, 106–117.
- (27) Iniesta, J.; Michaud, P. A.; Panizza, M.; Comminellis, C. Electrochemistry Communications **2001**, 3, 346–351.
- (28) Wang, J.; Hutchins, L. D. Analytical chemistry **1985**, 57, 1536–1541.

CHAPTER V

Diamond microelectrodes: Electrophysiological applications



Introduction

Electrophysiology is the study of electrical properties of cells and tissues which involve measurement of the voltage change of a biological entity. It is a powerful approach not only to study the electrical activity of animal cells to understand the working of the nervous system, brain, hypothalamus, etc. but also to diagnose and treat nervous system disorders. The electrical activity of neurons can be measured directly using extracellular microelectrode arrays. Using the microelectrodes the potential changes in the vicinity of the electrode, caused by currents flowing across neuronal membranes of multiple neurons, can be detected. Neural recording can be performed both in-vivo¹⁻³ (on live animal) and in-vitro⁴⁻⁶ (extracted cells).

Electrical stimulation of nerve cells is widely employed in neural prostheses, clinical therapies and neuroscience studies, as it has the potential to excite virtually every tissue. It is highly significant for individuals to restore the senses of hearing⁷ and vision⁸ and in the treatment of Parkinson disease,⁹ Paraplegia,¹⁰ etc. An implanted multichannel microelectrode array can be used to transmit electrical signals to the neurons and thus modulate their behavior. The electrodes should be biocompatible, micro-structured, deliver high charge injection limit without degradation and corrosion resistant.

Boron-doped diamond films, with their morphological and microstructural stability at high anodic current densities¹¹ and wide electrochemical potential window in aqueous electrolytes¹², are ideal candidates for neural recording and stimulation. Several studies have been conducted on diamond microelectrodes for neuro-chemical and neuro-electrical recording.¹³⁻¹⁵ The biocompatibility of diamond surfaces has been investigated by our group by implanting BDD microelectrodes in rat's eyes and no major gliosis was detected, which is commonly used as a biocompatibility indicator.¹⁶ Another advantage of diamond is the weak adsorption of polar molecules on its surface.¹⁷ As neural recording is done in ion and protein-rich environments which cause electrode fouling and hence to a decrease in the signal-to-noise ratio (SNR), a foul-resistant and chemically stable electrode is required.

The MEAs fabricated using the technique described in chapter 3 (design 2) were used for in-vitro electrophysiological measurements. Additionally we describe the fabrication and characterization process of a neural prosthesis: a retinal implants using BDD MEAs. Studies on the improvement of the charge injection limit are also included. This was achieved by nano-structuring the electrode.

5.1 Electrophysiological characterization of MEA

The 8x8 UMEA (diameter of the electrode = 14 μm) was characterized (refer to chapter 3 section 3.1.2) in collaboration with Prof. Blaise Yvert from INCIA, Bordeaux. Electrophysiological characterization included impedance measurement and noise level calculation.

5.1.1 Impedance measurement

Impedance measurements at 1 kHz (sine wave) were performed using either an IMP-I Electrode Impedance Tester from Bak Electronics Inc (Mount Airy, USA) or a NanoZ device from Multichannel Systems (Reutlingen, Germany, refer figure 5.1) in 0.1 0.5 M KCl aqueous solution.¹⁸ Figure 5.2 a and b shows the magnitude and phase of the impedance value obtained. The red spots in those figures shows abnormal value (typically very low magnitude and phase angle) and are omitted from the estimation of average impedance of the array. Also the green spots correspond to the electrodes that exhibited reduced electrochemical window (refer to chapter 3 section 3.3.1) and were also omitted from the calculation (associated with non-continuous diamond film).

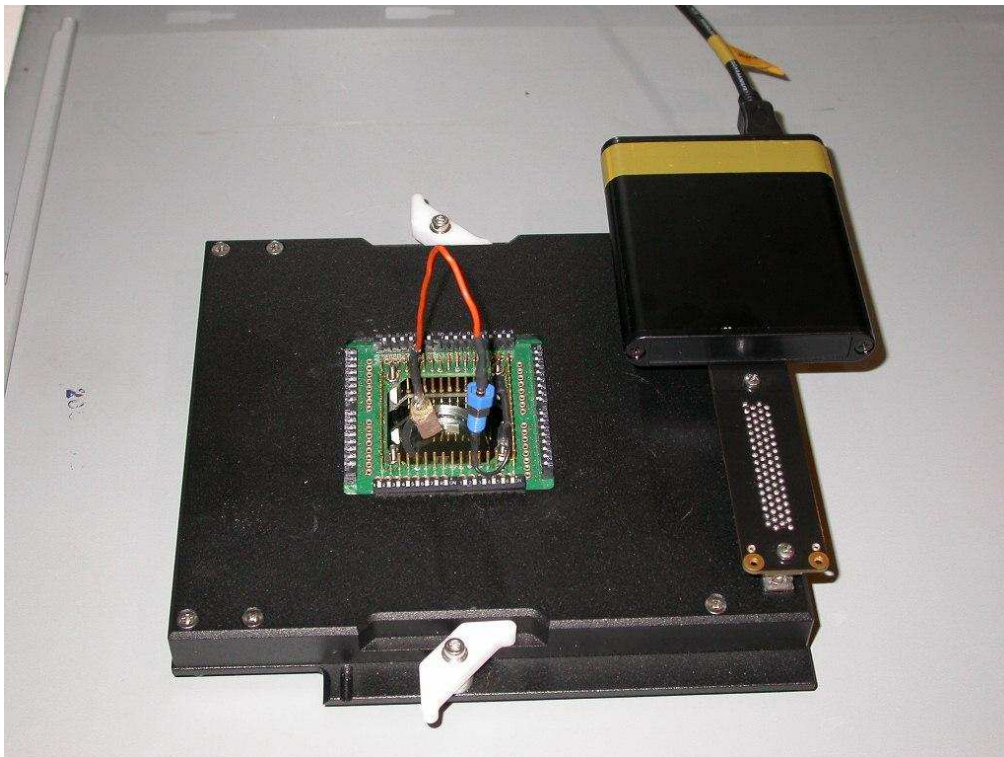
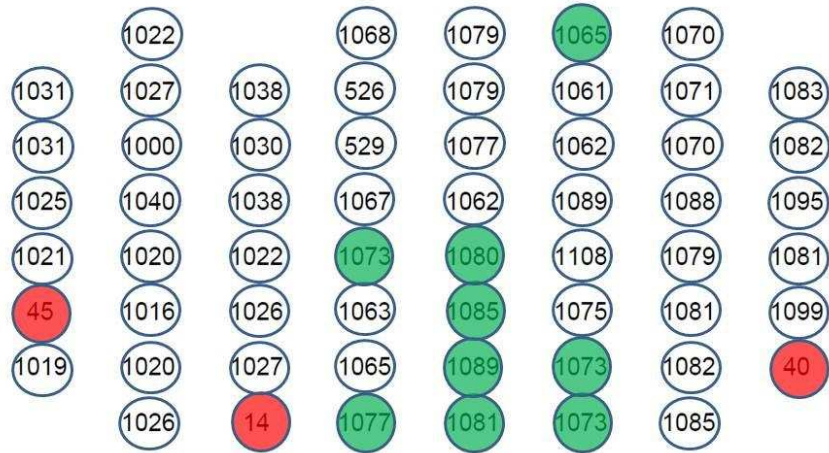
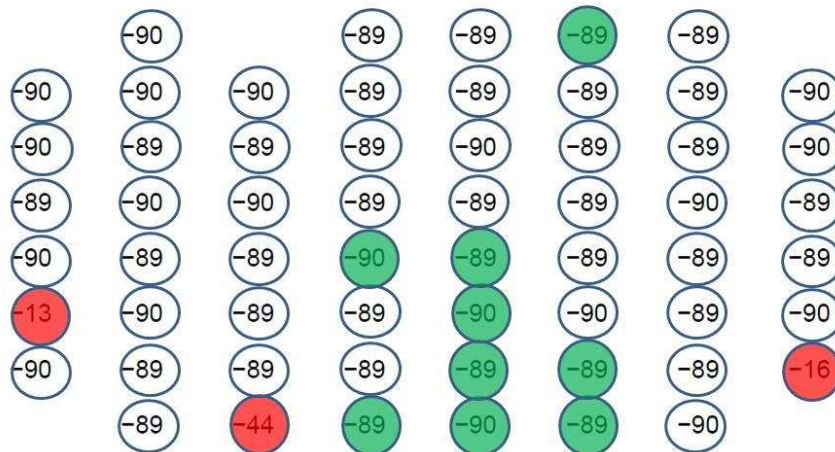


Figure 5.1 8x8 BDD UMEA fixed on NanoZ device to measure the magnitude and phase of the impedance at 1 kHz.



(a)



(b)

Figure 5.2 (a) Magnitude and (b) phase of the impedances at 1 kHz for all 59 boron doped diamond ultra-microelectrodes of 14 μm diameter. The red spots correspond to those electrodes with abnormal magnitude and phase and the green spots correspond to those electrodes which did not exhibit typical diamond potential window.

The impedances (Z) of other electrodes of this array measured at 1 kHz, were found to be very homogenous around 1033 ± 50 kohm, (mean \pm sd). One can observe from figure 5.2 b that the impedance measured is purely reactive as the phase angle is almost -90° . The double layer capacitance obtained from the Nyquist plot (chapter 2 section 3.3.3) for the electrodes were 150 pF and at 1 kHz the impedance is 1061 kohm (equation 2.1) which shows a very good correlation to the observed average value (of 1033 kohm).

$$Z = \frac{1}{2\pi f C_D} \quad (5.1)$$

where f is the frequency of the sinusoidal wave and C_D is the double layer capacitance.

5.1.2 Noise level measurement

To measure the intrinsic noise level of the electrodes, the electrical potential was recorded for 1 min in physiological liquid between each of the 60 microelectrodes and an Ag/AgCl ground electrode pellet. Signals were 1100 x amplified and band-pass filtered between 1 Hz and 3 kHz using MCS MEA1060-Up-BC filter amplifiers from Multichannel Systems (Reutlingen, Germany). Data were acquired at 10 kHz using two synchronized CED Power1401 AD converters and the Spike2 v6 software from Cambridge Electronic Design (Cambridge, England). The standard deviation of the signal σ_s was then calculated over the 1 min recording period for each electrode of the array. Because this noise level was composed of both the intrinsic noise level of the electrodes σ_e and the electronic noise level of the amplifiers σ_a , we assumed statistical independence of these two noise sources and estimated the intrinsic noise level of each electrode as:

$$\sigma_e = \sqrt{\sigma_s^2 - \sigma_a^2} \quad (5.2)$$

where $\sigma_a = 1.4 \mu\text{V}$ was measured with the amplifier inputs connected to the ground. The average noise level of the electrodes was observed to be $6 \mu\text{V}$. This value is significantly higher when compared to commonly used implants like titanium nitride.¹⁹

5.1.3 Neural recording

Embryos were surgically removed from pregnant mice and the hindbrain-spinal cords were dissected in cooled Ringer solution (pH 7.5) composed of (in mM): 113 NaCl, 4.5 KCl, 2 CaCl₂.2H₂O, 1 MgCl₂.6H₂O, 25 NaHCO₃, 1 NaH₂PO₄.H₂O and 11D-Glucose gassed with carbogen (95% O₂ and 5% CO₂).²⁰ The dissected hindbrain-spinal cords were placed dorsally

in the MEA cylindrical chamber, with the external side of the neural tube in contact with the microelectrodes of the array (refer figure 5.3). The neural tissue was stabilized using a plastic net with small holes ($70\ \mu\text{m} \times 70\ \mu\text{m}$) in order to achieve a tight and uniform contact with the microelectrodes. Experiments were conducted at room temperature. For recording and stimulating the neurons, a 64 channel electronic device called BioMEA™ (from Biologic) has been used and the whole experimental setup was mounted on it.²¹

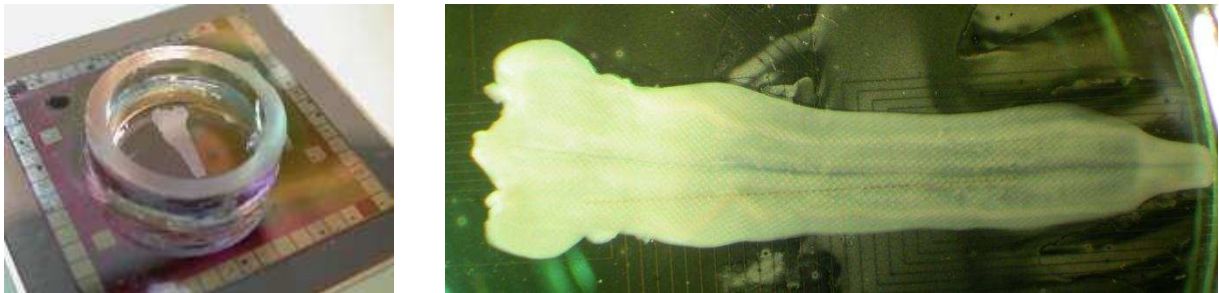


Figure 5.3 A whole mouse embryonic hindbrain-spinal cord system positioned on an 8 x 8 microelectrode array.

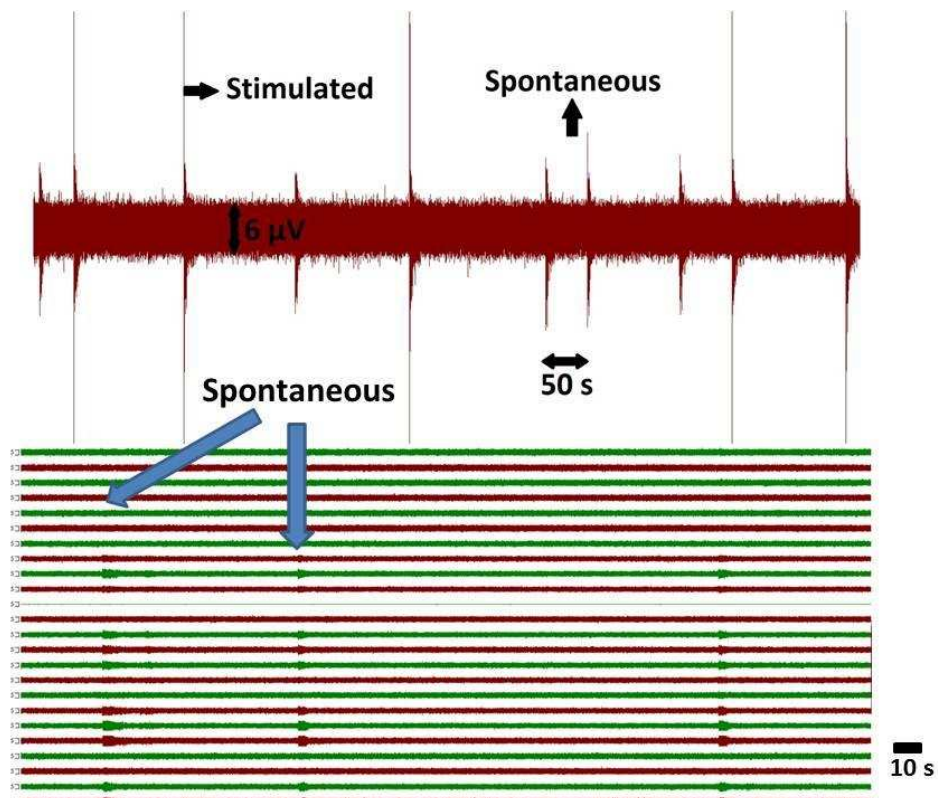


Figure 5.4 A close-up view of wave propagation triggered by electrical stimulation on 1 channel and waves of spontaneous activity on 24 channels

The spontaneous activity of the developing neural network was recorded with the help of the microelectrodes. Each spike lasts for a few seconds and recurs every few minutes. The spontaneous spikes generated by the neural network change with the development in the embryonic stage. For the establishment of neural connectivity it is essential to have this spontaneous neural activity.²⁰ This activity is due to intracellular calcium influxes which play an important role in promoting axonal growth. The spontaneous spikes generated exhibit typical amplitude of 20 μV .

The BioMEA™ system was used to stimulate neurons electrically through one microelectrode with biphasic current stimuli ($\pm 100 \mu\text{A}$, 500 $\mu\text{s}/\text{phase}$) with an external reference electrode (Ag/AgCl). All other electrodes are used to record the stimulated activity of the neuron. Each stimulus triggered an episode of activity which propagated rostrocaudally along the whole preparation. Figure 5.4 shows the stimulated and spontaneous activity of the neurons.

There are several possible reasons for the low SNR.¹⁵ If the probe position is not close enough to the neurons, then the strength of the neuron signal attenuates with increasing distance between the recording site and the target neurons. When compared to metal electrodes, the resistivity of boron doped-diamond is relatively high and this causes an increased thermal noise. A novel fabrication technique is developed and is described in section 5.3 to decrease the impedance and increase the SNR.

5.2 Diamond microelectrode array as neural prosthesis: Retinal implants

The neural interface and prosthesis presents many significant challenges in the development of advanced devices designed to restore function in neurologically impaired patients. Implantable microelectrodes can be used to record neuronal action potentials or local field potentials and stimulate the neurons. European (NEUROCARE, DREAMS) and French (MEDINAS, IMPLANT) research projects aim to develop better retinal implants based on carbon materials. Diamond, being robust and bio-inert, has been chosen as a candidate for recording and stimulating the neurons. Age-related macular degeneration, retinis pigmentosa, etc. can lead to partial or complete blindness and despite enormous advancement in clinical treatments, there are no methods to prevent or cure these diseases.²² The development in micro-fabrication techniques have opened new possibility for developing microelectrode arrays that can be implanted in the retina and can stimulate electrically the neural network to restore lost function.

5.2.1 Platinum microelectrode arrays

Implantable platinum microelectrode arrays were fabricated as well as the boron-doped diamond MEA in order to compare their performances in the electrochemical, electrophysiological and biocompatibility tests. Figure 5.5 describes the technological processes used in the fabrication of Pt MEAs. Four inch silicon wafers were oxidized to form a 500 nm silicon dioxide layer (refer to chapter 3 section 3.1 for more details). The oxide layer acts as the sacrificial layer. A 10 μm layer of polyimide precursor was applied on top of the oxide layer by spin coating and was cured at 375 $^{\circ}\text{C}$ under nitrogen. The polyimide was etched selectively under oxygen plasma using a metal etch mask. Pt was deposited by physical vapor deposition over the patterned polyimide layer and was patterned using a lift-off process. A second polyimide layer of 10 μm thickness was deposited and the contact pads were exposed by selective etching of the polyimide. The polyimide was then detached from the silicon substrate by dissolution in HF.

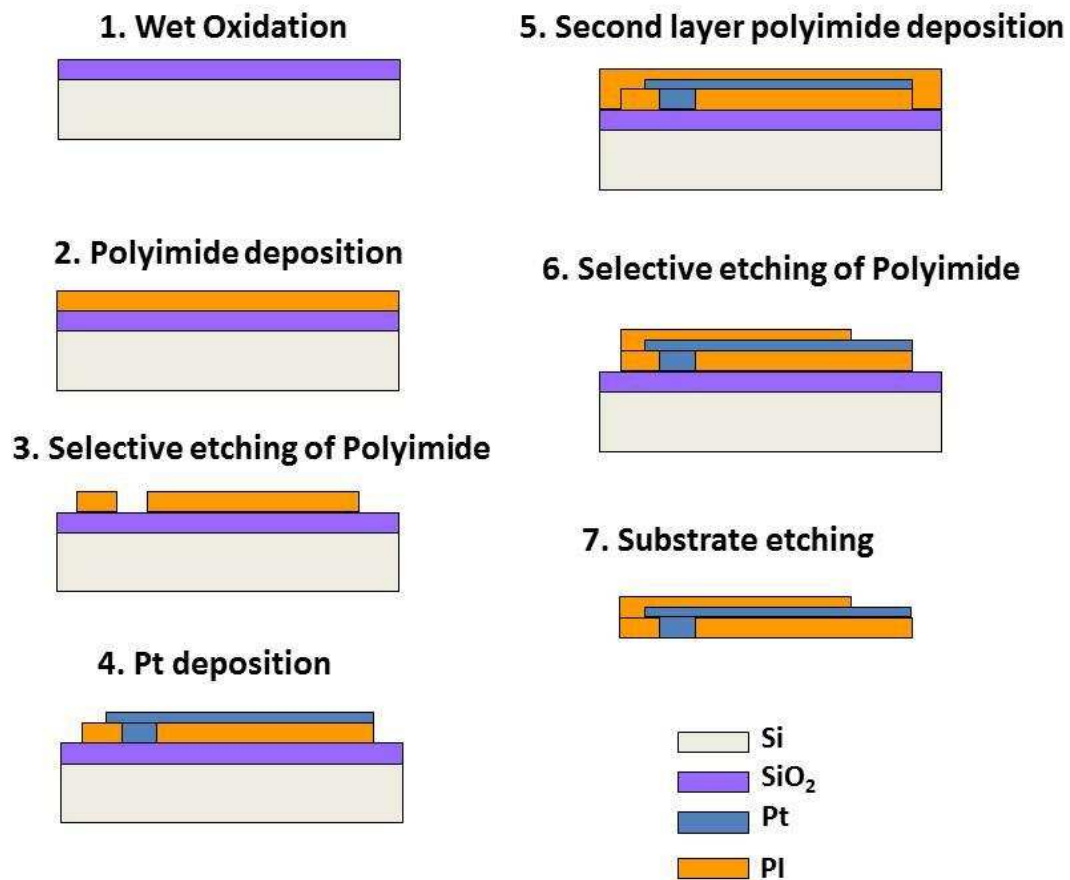


Figure 5.5 Schematics of implantable 8 x 8 Pt microelectrode array fabrication process.

The polyimide coated Pt retinal implants have an implant “head” dimension of 1.8 mm in diameter and rectangular “tail” of 27 mm long and 1.6 mm wide. Figure 5.6 shows the photos of 8x8 electrode array. The electrodes are of 14 μm in diameter and inter-electrode distance of 100 μm .

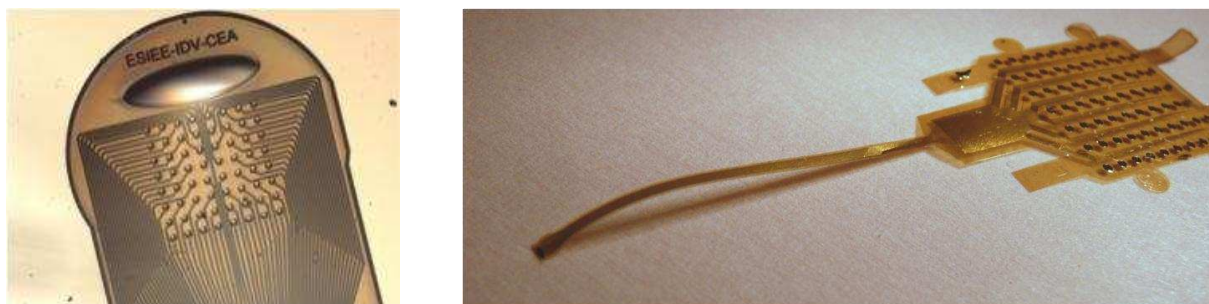


Figure 5.6 Pt soft implant (8 x 8 electrode array)

The Pt microelectrode arrays were characterized to evaluate their electrochemical performances. Detailed characterization techniques are described in chapter 1 (section 1.4) and 3 (section 3.3). Typically the electrochemical window recorded for the Pt electrodes was 1.8 V (measured in in 0.5 M aqueous LiClO_4 solution) and hence close to the values reported by other groups.²³ Figure 5.7 shows a voltammogram of one of the microelectrode (14 μm in diameter) scanned at 100 $\text{mV}\cdot\text{s}^{-1}$.

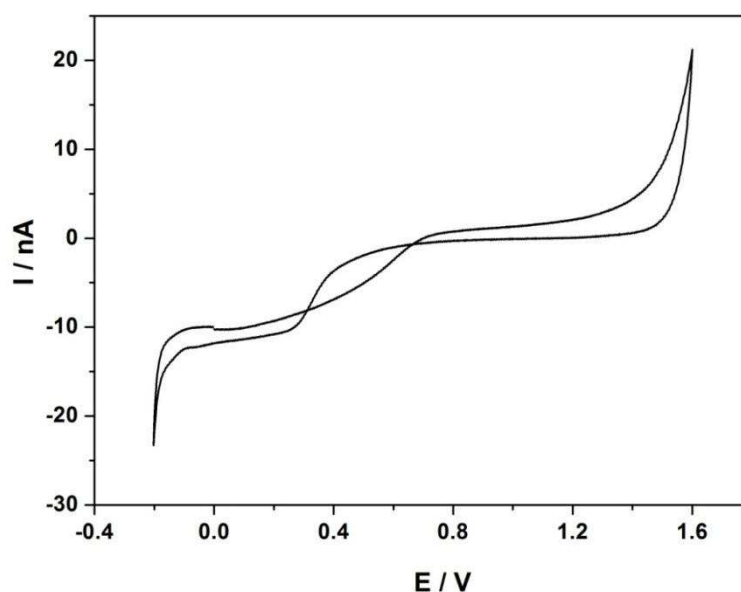


Figure 5.7 Cyclic voltammetry (scan rate=100 $\text{mV}\cdot\text{s}^{-1}$) of Pt microelectrode in 0.5 M aqueous LiClO_4 solution

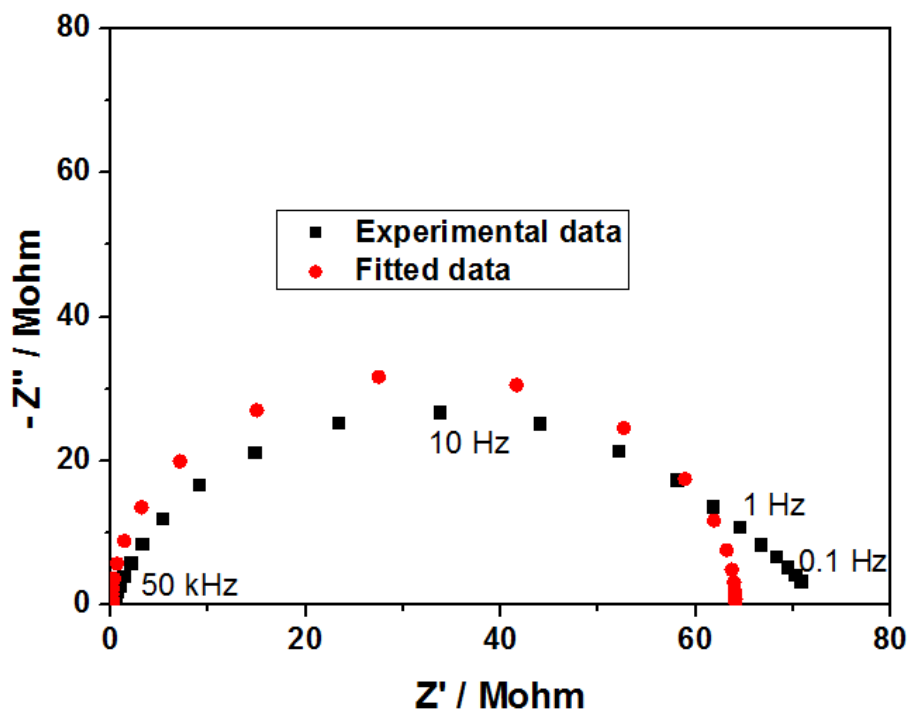


Figure 5.8 Nyquist plot (experimental data and fitted data) of Pt microelectrode.

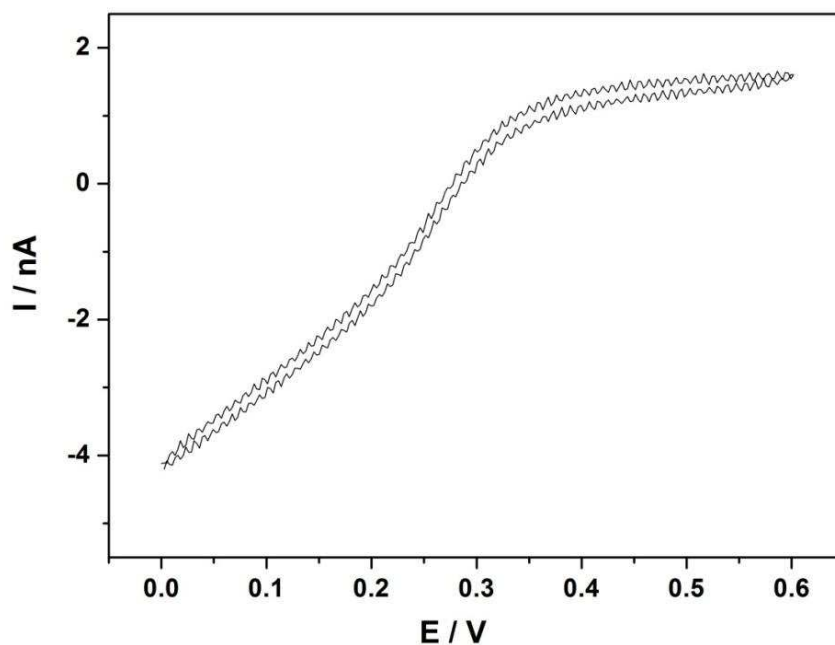


Figure 5.9 Cyclic voltammogram of Pt microelectrode at $100 \text{ mV}\cdot\text{s}^{-1}$ in 0.5 M potassium chloride aqueous solution containing $1 \text{ mM Fe}(\text{CN})_6^{4-}$ ion.

The steady state limiting current (in 1mM $\text{Fe}(\text{CN})_6^{3-/4-}$ in 0.5 M KCl solution at 100 mV.s^{-1} - figure 5.9) was observed to be 1.5 nA (compared to the theoretical value of 1.8 nA). The electron transfer rate k_0 and the double layer capacitance C_D estimated from Nyquist plot (figure 5.8) were 0.003 cm.s^{-1} and 126 pF respectively. Although the microelectrodes exhibit poor electron transfer rates and limiting current, they find application in electrophysiological applications due to its high double layer capacitance that reduces the noise level and increases the charge injection limit.^{15,24}

5.2.2 Diamond microelectrode arrays

Implantable BDD microelectrode arrays were fabricated using a similar process to that described in section 5.2.1 and figure 5.10. Diamond nanoparticles were fixed on an oxidized silicon wafer and were patterned using a metal mask (refer to chapter 3 section 3.1). After the diamond growth, a polyimide precursor was applied on top of the oxide layer by spin coating and was cured. The polyimide was etched selectively and Ti/Pt contacts and tracks were deposited by physical vapor deposition over the patterned polyimide layer and are in contact with BDD film. A second polyimide layer of $10 \mu\text{m}$ thickness was deposited and the contact pads were exposed by selective etching of the polyimide which is followed by substrate detachment.

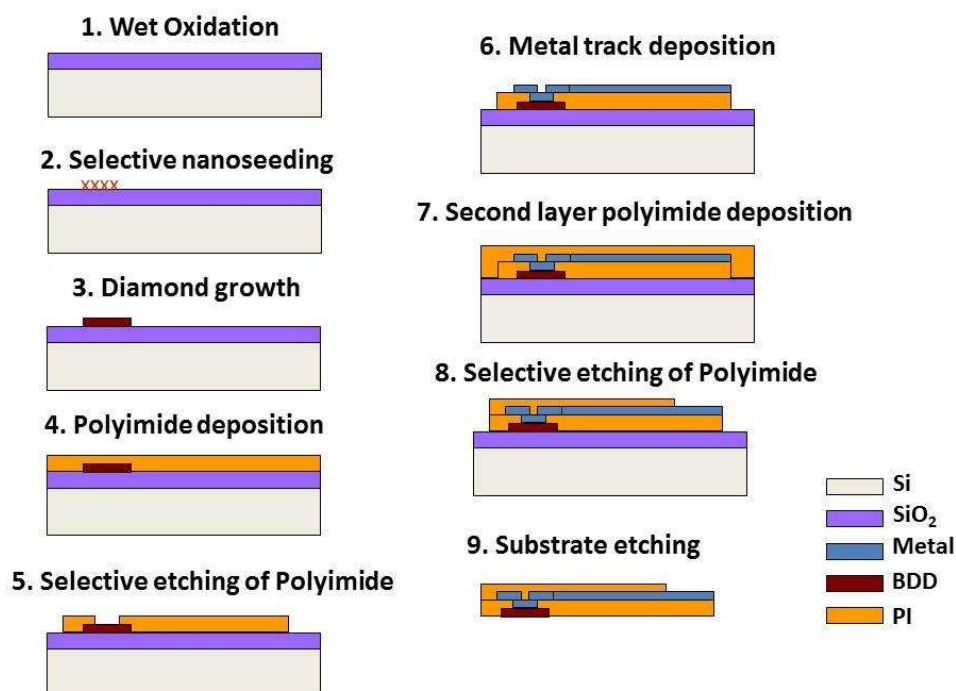


Figure 5.10 Schematics of implantable 8 x 8 BDD microelectrode array fabrication process.

The electrochemical window recorded for the BDD electrodes was typically 3 V and is less than the values reported by other groups.²⁵ Figure 5.11 shows a voltammogram for a BDD microelectrode (14 μm in diameter) scanned at $100 \text{ mV}\cdot\text{s}^{-1}$. The peak current (in $1 \text{ mM Fe(CN)}_6^{3-/4-}$ in 0.5 M KCl solution at $100 \text{ mV}\cdot\text{s}^{-1}$ - figure 5.12) was observed to be 320 nA which is 178 times higher than the theoretical value (assuming a steady state voltammogram). From the Nyquist plot (figure 5.13), k_0 and C_D were estimated and were $2.1 \text{ cm}\cdot\text{s}^{-1}$ ($R_T = 84 \text{ kohm}$) and 24 nF (again the values are much higher than the expected values). The high electron transfer rate, capacitance and limiting current suggest that there might be some leakage during the fabrication process where the electrodes are shorted or in contact with the grid (which is used to achieve focal stimulation). Also the reduced window suggests that titanium or the electrolyte itself might have diffused through the polyimide and thus demonstrates the difficulty of structuring a coherent process here.

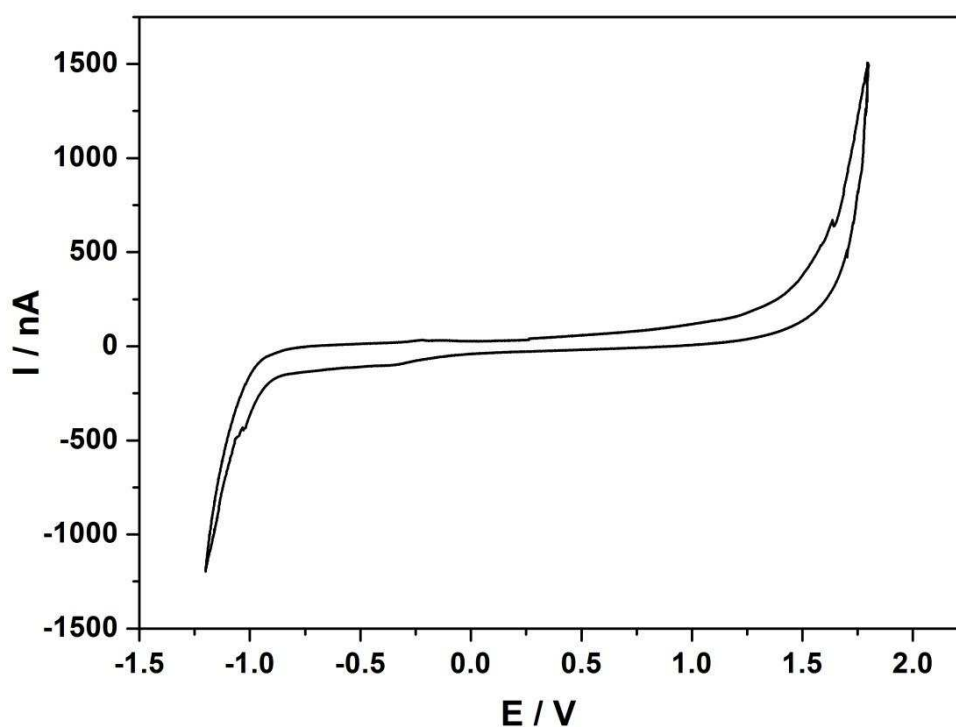


Figure 5.11 Cyclic voltammetry (scan rate= $100 \text{ mV}\cdot\text{s}^{-1}$) of BDD microelectrode in 0.5 M aqueous LiClO_4 solution

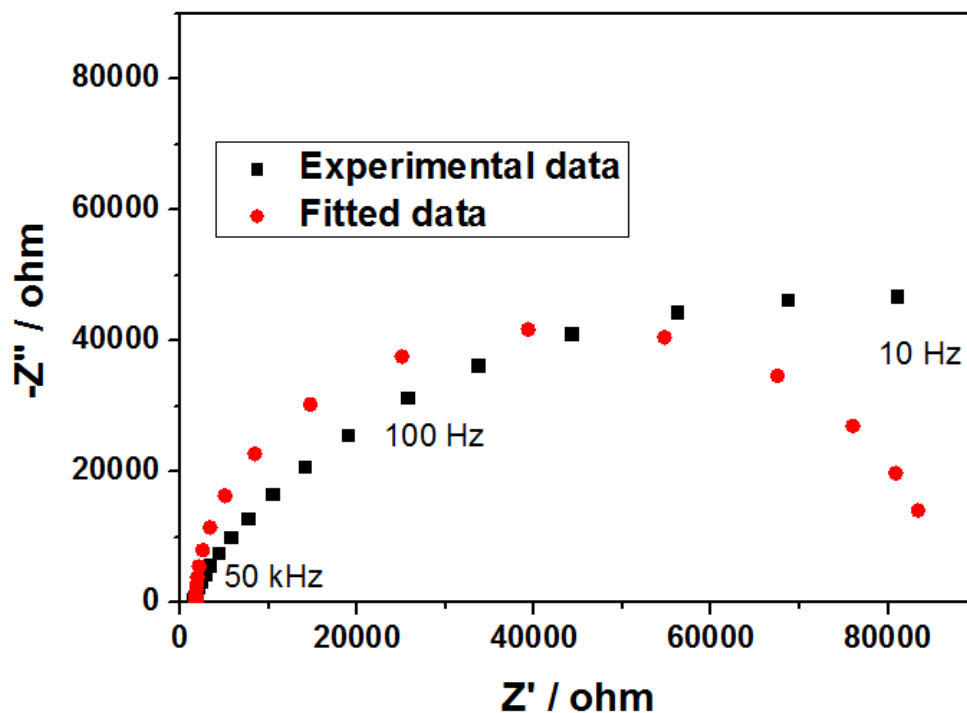


Figure 5.12 Nyquist plot (experimental data and fitted data) of BDD microelectrode.

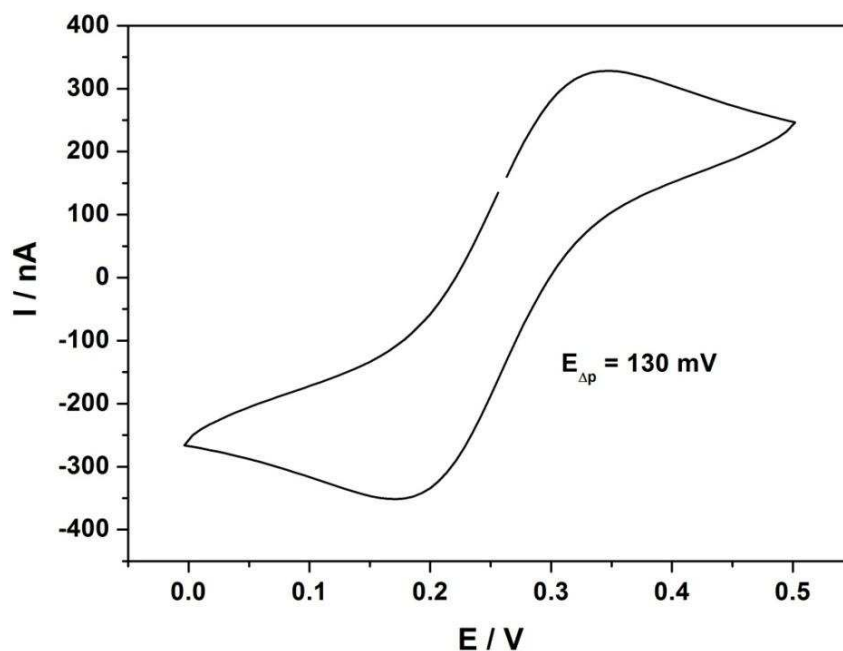


Figure 5.13 Cyclic voltammogram of BDD microelectrode at $100 \text{ mV}\cdot\text{s}^{-1}$ in 0.5 M potassium chloride aqueous solution containing $1 \text{ mM Fe(CN)}_6^{4-}$ ion.

The technological process has to be improved in order to fabricate implantable BDD microelectrode array with no leakage. Weiland et al. have evaluated the polymer layers: polyimide, parylene and silicone as the retinal prosthesis substrates.²⁶ The study indicates that parylene possess the best property among the polymers and multi-polymer approach is best suited for the implants. A long term soak-test is necessary to evaluate the insulation property of the polymer layer.

5.3 Nanograss diamond MEA

For neural stimulation, electrodes should be capable of injecting relatively large currents while minimizing electrode degradation due to faradaic effects. In order to allow long-term operation, the surface of the microelectrodes should be able to facilitate charge transport without degradation of the electrode. This led us to the fabrication of BDD nanograss microelectrode arrays with enhanced double layer capacitance ideal for neural recording and stimulation. Since the surface was not modified, rather they were nanostructured, the electrodes possessed the physical and chemical properties of diamond with superior charge injection limits.

5.3.1 Fabrication of nanograss MEA

There has been several techniques reported for nanostructuring diamonds which including oxygen plasma etching through porous anodic alumina films,²⁷ self-aligned Au nanodots as an etching mask in hydrogen/argon plasma,²⁸ nanodiamond powder hard mask in reactive ion etching (RIE) in O₂/CF₄ gas mixture²⁹ etc. We have adopted a simple method to nanostructure BDD MEAs (4 x 16 electrodes of diameter varying from 10 to 70 μm, refer chapter 3 section 3.1.2 for detailed fabrication process) by using RIE without using any mask.³⁰ Diamond was etched by the use of oxygen plasma under a pressure of 8 mbar at 30 sccm and plasma power of 200 W for 1 minute. As per Wei et al. the boron dopant atoms in the diamond act as the mask during plasma etching and the boron oxides are redeposited on top of the nanograss and continues to serve as the mask.³⁰ Even if this mechanism is not well understood, we used the technique to successfully fabricate BDD nanograss.

5.3.2 SEM characterization

Figure 5.14 shows the SEM images of a nanostructured BDD nanograss electrode (electrode diameter = 20 μm). The nanograss structures exhibit dimensions of around 100 nm in length and 10-20 nm in diameter and 20-30 nm of inter-nanograss distance.

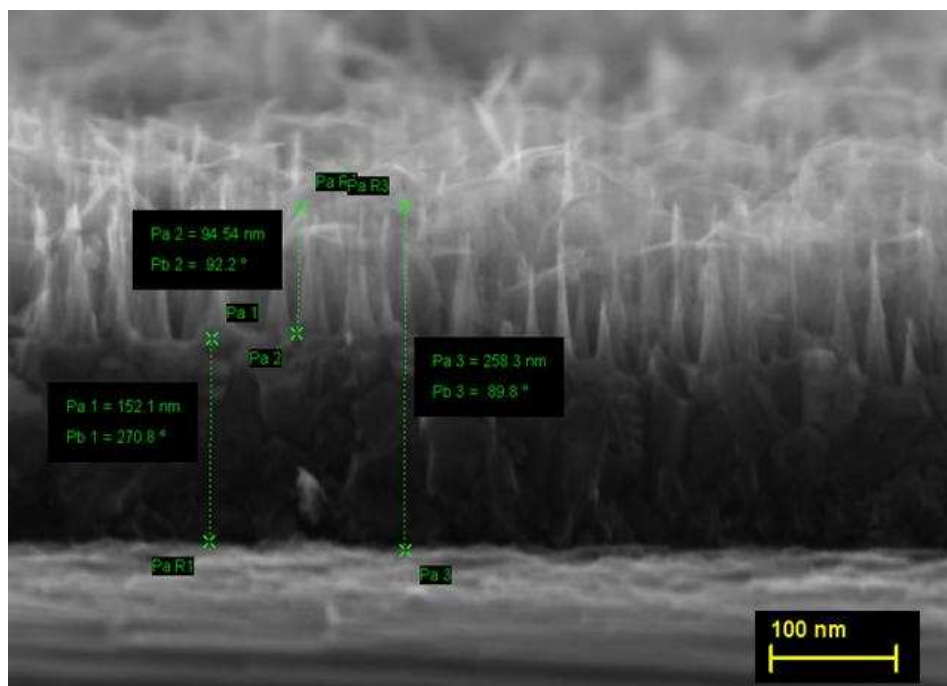


Figure 5.14 SEM image of cross-section of BDD nanoglass electrode.

5.3.3 Electrochemical characterization

The Nyquist plot obtained was a semicircular spectrum which matches a Randles circuit with no Warburg impedance component. The values of each component of the system (R_s , C_D , and R_T) were calculated from these spectra (refer chapter 1 section 1.4.2 for detailed experimental setup). Figure 5.15 shows the measured and calculated Nyquist plot of one such electrode (of diameter 20 μm). The resistance measured between the working electrode and the reference electrode, the ohmic resistance R_s , includes the resistance of the solution and the resistance of the metallic track and was 2076 Ω . The fitted C_D , and R_T values were of 288 pF and 73.73 Mohm respectively.

The double layer capacitance of the nanoglass microelectrode was about 30 times higher than the theoretical value of diamond electrode ($3 \mu\text{F}\cdot\text{cm}^{-2}$) indicating that the effective surface area of the electrode has been increased by a factor more than 30. The electrode electron transfer rate k_0 was calculated to be $1.15 \times 10^{-3} \text{ cm}\cdot\text{s}^{-1}$. Although H-terminated BDD electrodes are known to exhibit reactivity as high as $0.2 \text{ cm}\cdot\text{s}^{-1}$, the oxygen plasma treatment has reduced the reactivity considerably. Low k_0 value is an added advantage to the nanostructured MEAs as they reduce the faradaic current which involves in electrochemical changes to the solution while stimulating.

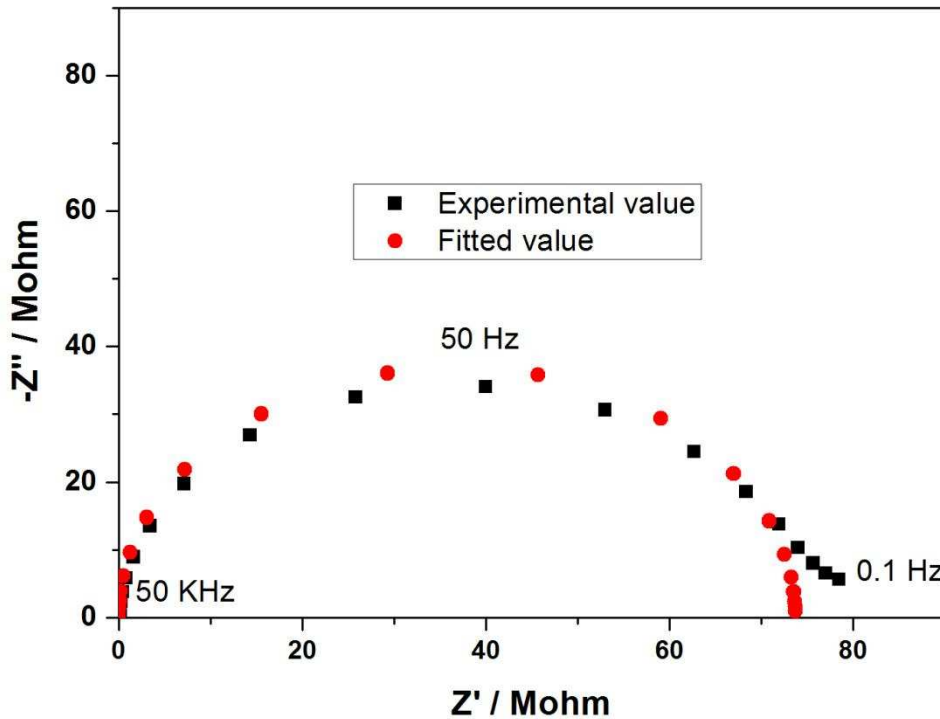


Figure 5.15 Nyquist plot (experimented and fitted curves) of a nanograss diamond microelectrode, showing the $\text{Re}(Z)$ vs $-\text{img}(Z)$ and is a semi-circular spectrum indicating that the straight line (Warburg element) is absent.

Figure 5.16 shows the EC potential window of the nanograss microelectrode which is about 3.4 V (similar to typical BDD window) with reduction and oxidation of water occurring at -1.5 V and 1.9 V respectively. The CV curves indicate that there is neither crack nor pin-holes in the passivation layer and that the only current component within the window is the transient current which charges and discharges the double layer constituting the background current within the potential window.

The enhanced background current together with the wide potential window increases the charge injection limit needed for neural stimulation. Steady state limiting current i_{lim} of ferrous oxidation was calculated from the CV (figure 5.17) in $\text{Fe}(\text{CN})_6^{3-/4-}$ solution and is 8.78 nA. The theoretical value i_{lim} for this 20 μm diameter (with the effective area enhanced by 30.5 times) is 78.53 nA.

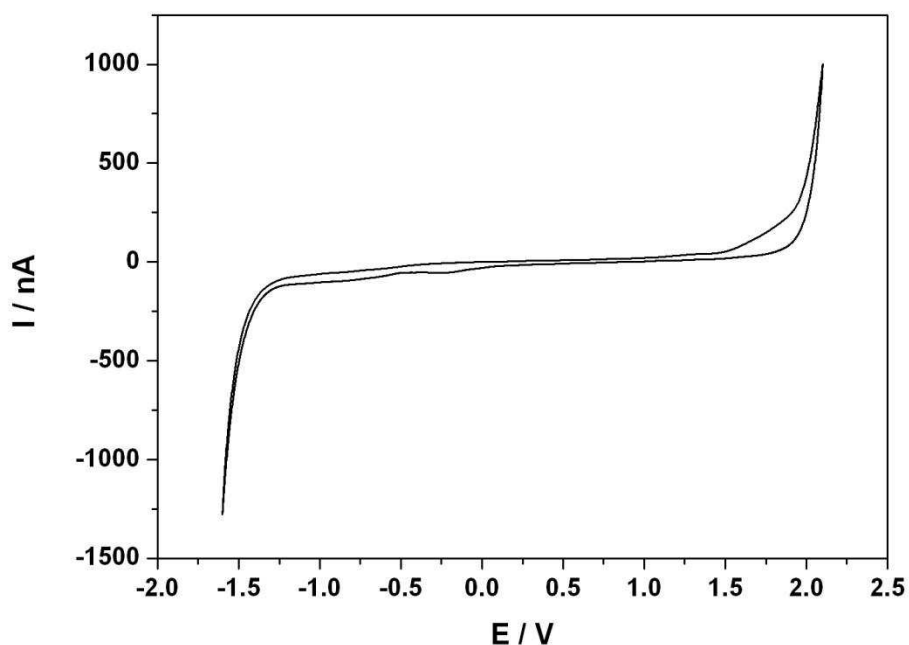


Figure 5.16 Cyclic voltammogram of nanograss diamond microelectrode scanned at $0.2 \text{ V}\cdot\text{s}^{-1}$ in 0.5 M LiClO_4 aqueous solution.

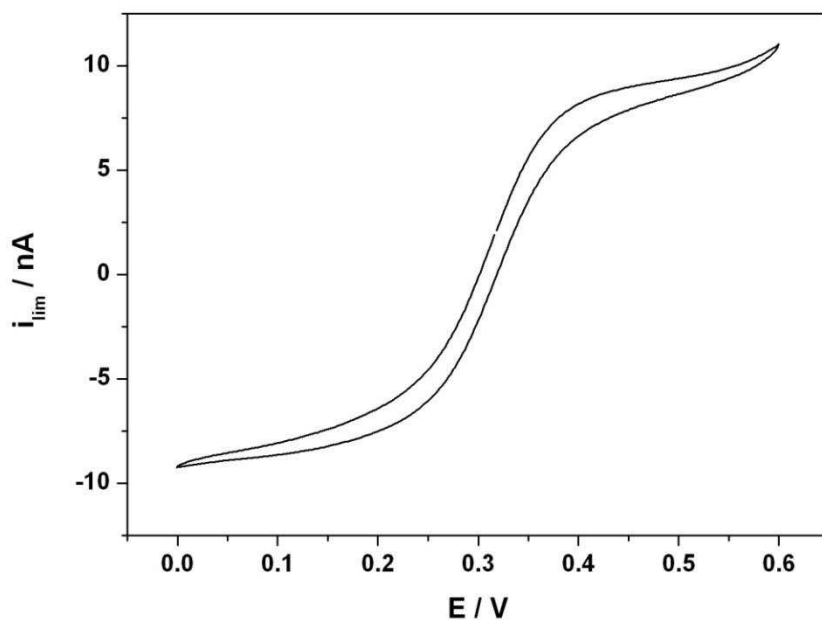


Figure 5.17 Cyclic voltammogram of nanograss diamond microelectrode scanned at $0.1 \text{ V}\cdot\text{s}^{-1}$ in 0.5 M KCl aqueous solution containing $1 \text{ mM of Fe(CN)}_6^{3-/4-}$.

The huge difference in the observed and theoretical value of the limiting current can be explained by the low reactivity of the nanograss microelectrodes, probably due to the fact that not the entire surface is active due to high series resistance of the diamond nanowires.

5.3.4 Electrophysiological characterization

Impedance measurements at 1 kHz on a 4 x 16 array of BDD nanograss of varying diameter is depicted in figure 5.18. The impedances of the electrodes of this array measured at 1 kHz, were not very homogenous around $202 \pm 139 \text{ Mohm} \cdot \mu\text{m}^2$ (mean \pm sd). The impedance measured is reactive and the phase angle is -86° . The double layer capacitance obtained from the Nyquist plot for the electrode (20 μm diameter) was 288 pF and at 1 kHz the impedance is $174 \text{ Mohm} \cdot \mu\text{m}^2$. Since the surface of the nanograss is rough, the effective surface area is not known and hence this can cause variations in the impedance values measured from electrode to electrode.

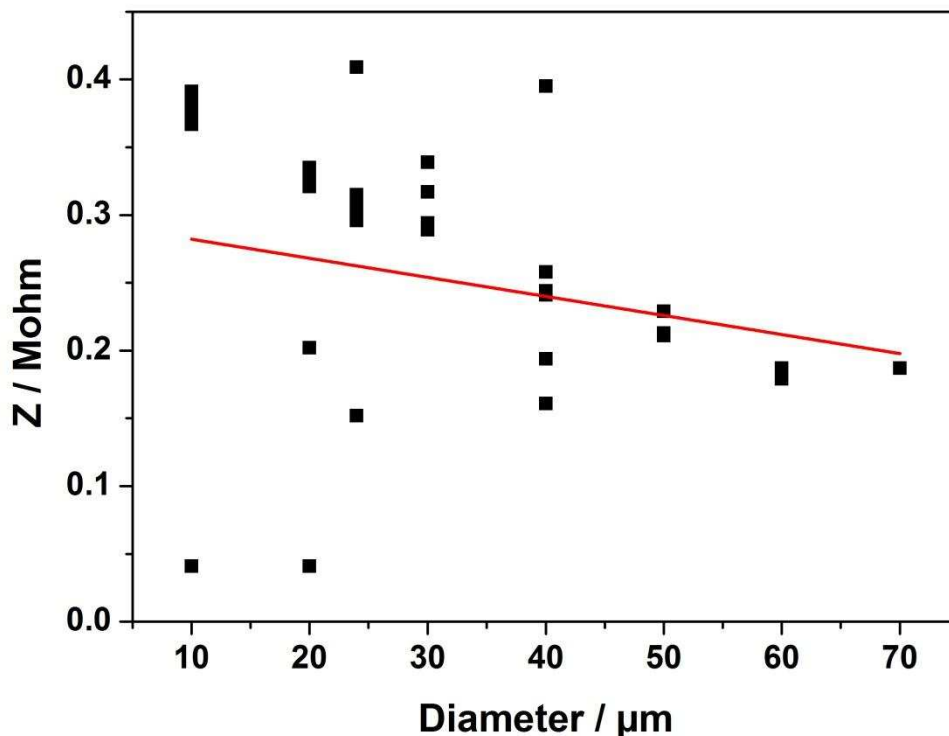


Figure 5.18 Electrode impedance measured for the 4 x 16 array.

The noise measured for this array is in good correlation with the impedance. As the diameter increases the noise level decreases. Figure 5.19 shows the noise level measured for the 4 x 16 MEA. The charge injection limit measured was above $100 \mu\text{C}\cdot\text{cm}^{-2}$.

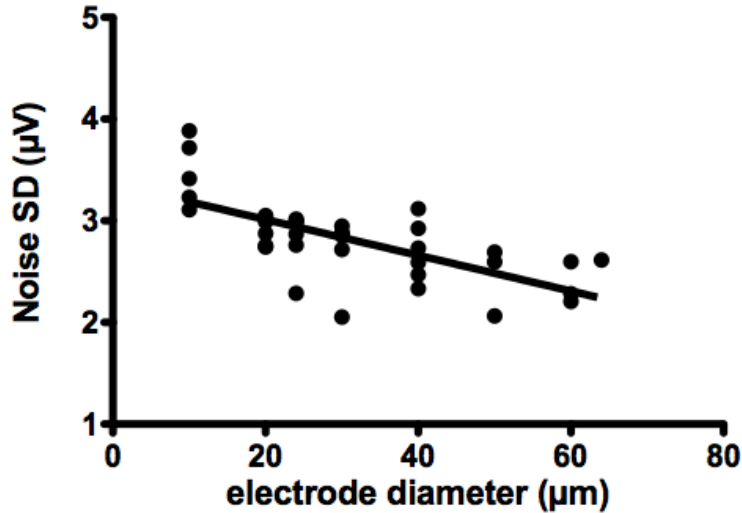


Figure 5.19 Electrode impedance measured for the 4 x 16 array.

The BDD nanograss microelectrode array with its very low impedance and noise level and high charge injection limit could be a very useful tool for electrophysiological applications. The surface being diamond, the biocompatibility and corrosion resistivity of the electrodes are expected to be excellent.

Conclusions

Diamond is an excellent neural prosthesis with its superior physical and chemical properties along with biocompatibility. In this chapter we have seen reported several approaches proposed to enhance the electrical properties of diamond to make it an ideal electrode for electrophysiological applications. Although BDD-PPy electrodes cannot be successfully used for neural prosthesis it has opened ways to other research areas such as the power storage and transmission.

BDD nanograss microelectrodes exhibit very high charge injection limits and when compared to titanium nitride and iridium oxide, diamond possess better biocompatibility and microstructural stability. Increasing the number of electrodes, designing the appropriate electrode shapes (so far the shapes were all planar) and further electrode surface modification

can make BDD nanograss MEAs superior devices than other competing techniques for neural prosthesis.

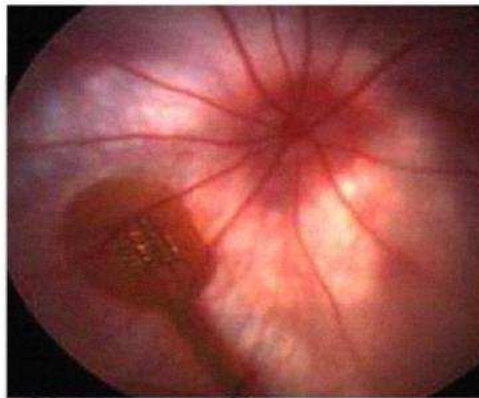
Bibliography

- (1) Blau, a; Ziegler, C.; Heyer, M.; Endres, F.; Schwitzgebel, G.; Matthies, T.; Stieglitz, T.; Meyer, J. U.; Göpel, W. *Biosensors & bioelectronics* **1997**, 12, 883–92.
- (2) Cheung, K. C.; Renaud, P.; Tanila, H.; Djupsund, K. *Biosensors & bioelectronics* **2007**, 22, 1783–90.
- (3) Kuperstein, M.; Whittington, D. a *IEEE transactions on bio-medical engineering* **1981**, 28, 288–93.
- (4) Gross, G. W.; Rieske, E.; Kreuzberg, G. W.; Meyer, A. *Neuroscience Letters* **1977**, 6, 101–105.
- (5) Berdondini, L.; van der Wal, P. D.; Guenat, O.; de Rooij, N. F.; Koudelka-Hep, M.; Seitz, P.; Kaufmann, R.; Metzler, P.; Blanc, N.; Rohr, S. *Biosensors & bioelectronics* **2005**, 21, 167–74.
- (6) Gross, G. W. **1979**, 273–279.
- (7) Grill, W. M.; Mortimer, J. T. *IEEE Engineering in Medicine and Biology Magazine* **1995**, 14, 375–385.
- (8) Normann, R. a; Maynard, E. M.; Rousche, P. J.; Warren, D. J. *Vision research* **1999**, 39, 2577–87.
- (9) Limousin, P.; Krack, P.; Pollak, P.; Benazzouz, A.; Ardouin, C.; Hoffmann, D.; Benabid, A. *The New England Journal of Medicine* **1998**, 339, 1105–1111.
- (10) Brindley, G. S.; Polkey, C. E.; Rushton, D. N. *Paraplegia* **1979**, 16, 428–37.
- (11) Chen, Q.; Granger, M. C.; Lister, T. E.; Swain, G. M. J. *Electrochem* **1997**, 144, 3806–3812.
- (12) Panizza, M.; Michaud, P. a.; Cerisola, G.; Comninellis, C. *Journal of Electroanalytical Chemistry* **2001**, 507, 206–214.
- (13) Park, J.; Quaiserova-mocko, V.; Peckova, K.; Galligan, J. J.; Fink, G. D.; Swain, G. M. *Diamond and Related Materials* **2006**, 15, 761–772.
- (14) Halpern, J. M.; Xie, S.; Sutton, G. P.; Higashikubo, B. T.; Chestek, C. a.; Lu, H.; Chiel, H. J.; Martin, H. B. *Diamond and Related Materials* **2006**, 15, 183–187.
- (15) Chan, H.; Aslam, D. M.; Member, S.; Wiler, J. A.; Casey, B. *journal of microelectromechanical systems* **2009**, 18, 511–521.
- (16) Bongrain, A.; Bendali, A.; Lissorgues, G.; Rousseau, L.; Yvert, B.; Scorsone, E.; Bergonzo, P.; Picaus, S. *DTIP proceeding* **2011**, 11–14.

- (17) Hupert, M.; Muck, A.; Wang, J.; Stotter, J.; Cvackova, Z.; Haymond, S.; Show, Y.; Swain, G. M. *Diamond and Related Materials* **2003**, 12, 1940–1949.
- (18) Prasad, A.; Sanchez, J. C. *Journal of neural engineering* **2012**, 9, 026028.
- (19) Ryyänen, T.; Kujala, V.; Ylä-Outinen, L.; Korhonen, I.; Tanskanen, J. M. a.; Kauppinen, P.; Aalto-Setälä, K.; Hyttinen, J.; Kerkelä, E.; Narkilahti, S.; Leikkala, J. *Micromachines* **2011**, 2, 394–409.
- (20) Yvert, B.; Branchereau, P.; Meyrand, P. *Journal of neurophysiology* **2004**, 91, 2101–9.
- (21) Charvet, G.; Rousseau, L.; Billoint, O.; Gharbi, S.; Rostaing, J.-P.; Joucla, S.; Trevisiol, M.; Bourgerette, A.; Chauvet, P.; Moulin, C.; Goy, F.; Mercier, B.; Colin, M.; Spirkovitch, S.; Fanet, H.; Meyrand, P.; Guillemaud, R.; Yvert, B. *Biosensors & bioelectronics* **2010**, 25, 1889–96.
- (22) Meyer, È. *Sensors and Actuators A* **2002**, 97-98, 1–9.
- (23) Braga, N. a.; Cairo, C. a. a.; Matsushima, J. T.; Baldan, M. R.; Ferreira, N. G. *Journal of Solid State Electrochemistry* **2009**, 14, 313–321.
- (24) Cheung, K. C. *Biomedical microdevices* **2007**, 9, 923–38.
- (25) Colley, A. L.; Williams, C. G.; D’Haenens Johansson, U.; Newton, M. E.; Unwin, P. R.; Wilson, N. R.; Macpherson, J. V. *Analytical chemistry* **2006**, 78, 2539–2548.
- (26) Weiland, J. D.; Humayun, M. S.; Eckhardt, H.; Ufer, S.; Laude, L.; Basinger, B.; Tai, Y.-C. *Conference proceedings : ... Annual International Conference of the IEEE Engineering in Medicine and Biology Society. IEEE Engineering in Medicine and Biology Society. Conference* **2009**, 4140–3.
- (27) Masuda, H.; Watanabe, M.; Yasui, K.; Tryk, D.; Rao, T.; Fujishima, A. *Advanced Materials* **2000**, 12, 444–447.
- (28) Zou, Y. S.; Yang, Y.; Zhang, W. J.; Chong, Y. M.; He, B.; Bello, I.; Lee, S. T. *Applied Physics Letters* **2008**, 92, 053105.
- (29) Yang, N.; Uetsuka, H.; Osawa, E.; Nebel, C. E. *Angewandte Chemie (International ed. in English)* **2008**, 47, 5183–5.
- (30) Wei, M.; Terashima, C.; Lv, M.; Fujishima, A.; Gu, Z.-Z. *Chemical communications (Cambridge, England)* **2009**, 3624–6.

CHAPTER VI

Conclusions and Future Perspectives



The global aim of the research discussed in this thesis is the design, fabrication, characterization and applications of Diamond microelectrodes. Yet the thesis also explores other topics such as in-situ activation technique, supercapacitors, etc.

4.1 Conclusions

The electrochemical activation process retrieves the lost reactivity of an electrode either aged in air or fouled by a medium. The other advantage of this technique is to enhance the reusability of the BDD electrode. Contrary to the other pre-treatments techniques commonly reported in the literature, for instance anodic, cathodic and thermal, this novel electrochemical treatment is relatively simpler, fast, and minimum resource consuming. To ensure reliable and reproducible results, especially when the electrode has not been used for a long period of time, it is recommended to perform this electrochemical activation prior to the experiments. Application of the activation technique has been seen in chapter 3 and 4 for cleaning the electrode surface from residual photoresist and to develop an automated human uric acid (UA) quantification sensor with in-situ cleaning.

A novel microfabrication technique to fabricate electrochemical and electrophysiological sensors has been developed for electro-analysis and neural recording. After experimenting several fabrication designs, a high-yield, reproducible design (design 2) was adopted, where diamond is grown before the deposition of metal tracks and the passivation layer. The electrodes exhibited very low leakage current and very high reactivity ideal for electrochemical sensors.

The strip microelectrodes fabricated as per design 2 were used to develop biosensors. Uric acid sensor based on the two proposed models indicates that the technique developed can be used as an alternative quantification process for spectrophotometric measurements. The fast scan cyclic voltammetry not only separates the uric acid and ascorbic acid peaks, but also decrease the effective quantification time. As the detection technique do not rely on any enzymatic reaction and does not need any surface modifications, a single electrode can be used for several times followed by the electrochemical activation. The in-situ activation protocol indicates the possibility to incorporate the biosensor to a bed-side monitor as the process can be fully automated.

Diamond, being biocompatible and possessing very high corrosion resistance, is a very good candidate for neural prosthesis as well as for in-vivo/in-vitro neural measurements. The

microelectrode arrays, although possess features better than conventional metal electrodes, are inferior compared to titanium nitride and iridium oxide in terms of charge injection limit and impedance. Attempts have made to address these disadvantages which include BDD surface modification and nano-structuring. BDD surface modification by BDD-PPy composite had serendipitously led to the invention of hybrid electrode with a very high specific capacitance of 130 F.g^{-1} . Nano-structured BDD microelectrodes (BDD nano-grass) with a high aspect ratio and a large surface area, is an answer to TiN and IrO_2 microelectrode arrays.

4.2 Future scope

The results of the studies presented in this thesis further suggest some area of scientific and technological interest. The in-situ activation process described in the thesis can find application in several analytical processes such as detection of neurotransmitters like dopamine, catecholamine, etc. In-vivo analysis is also possible as BDD is known to be bio-inert. Other applications include in-situ activation while quantifying the total polyphenol content during wine fermentation, waste water treatment, etc. The BDD strip electrodes and microelectrode arrays can be used for innumerable biomedical applications such as detection of heavy metals, neuro-chemical and –electrical recording especially to study the neural activity, drug delivery, neural prosthesis such as retinal, cochlear implants, etc. Functionalization of microelectrodes with enzymes can further extend the advantages of the microelectrodes as glucose, alcohol, DNA sensors etc.

Appendix A

A.1 Second order curve fitting results for UA concentration (see equation 4.1)

$$i_A = i_{A0} + aC_{UA} + bC_{AA} + cC_{UA}^2 + dC_{AA}^2 + f C_{UA}C_{AA}$$

	Value	Standard Error
i_{A0}	4.24028	1.70537
a	0.0671	0.00236
b	0.06186	0.01021
c	-2.91131E-6	8.58669E-7
d	-2.35667E-5	1.81746E-5
f	-1.22257E-5	3.07207E-6

Number of points	18
Degrees of Freedom	12
Reduced Chi-Sqr	5.16118
Residual Sum of Squares	61.93418
Adj. R-Square	0.99798
Fit Status	Succeeded(100)

A.2 Second order curve fitting results for UA concentration (see equation 4.2)

$$i_B = i_{B0} + aC_{UA} + bC_{AA} + cC_{UA}^2 + dC_{AA}^2 + f C_{UA}C_{AA}$$

	Value	Standard Error
i_{B0}	8.21117	1.21022
a	0.017	0.00168
b	-0.00874	0.00724
c	-1.94345E-6	6.09359E-7
d	-2.66667E-7	1.28977E-5
f	-8.52571E-6	2.18011E-6

Number of points	18
Degrees of Freedom	12
Reduced Chi-Sqr	2.59923
Residual Sum of Squares	31.19072
Adj. R-Square	0.97399
Fit Status	Succeeded(100)

A.3 Second order curve fitting results for UA concentration (see equation 4.3)

$$I_A = i_{A0} + aC_{UA} + bC_{AA} + cC_{UA}^2 + dC_{AA}^2 + f C_{UA}C_{AA}$$

	Value	Standard Error
I _{A0}	53.47723	15.68371
a	0.05391	0.01588
b	0.02718	0.00552
c	-2.56071E-6	5.46209E-6
d	-6.69643E-9	5.089E-7
f	-5.75357E-6	1.41031E-6

Number of points	30
Degrees of Freedom	24
Reduced Chi-Sqr	348.06835
Residual Sum of Squares	8353.64036
Adj. R-Square	0.91382
Fit Status	Succeeded(100)

A.4 Second order curve fitting results for UA concentration (see equation 4.4)

$$I_C = i_{C0} + aC_{UA} + bC_{AA} + cC_{UA}^2 + dC_{AA}^2 + f C_{UA}C_{AA}$$

	Value	Standard Error
I _{C0}	38.40045	7.59239
a	0.01469	0.00769
b	0.02105	0.00267
c	3.28929E-6	2.64417E-6
d	5.11161E-7	2.46356E-7
f	3.92786E-6	6.82721E-7

Number of points	30
Degrees of Freedom	24
Reduced Chi-Sqr	81.56888
Residual Sum of Squares	1957.65321
Adj. R-Square	0.99144
Fit Status	Succeeded(100)

